UNIVERSIDADE FEDERAL DE ALFENAS

IORRAN VIEIRA BATISTA

USING SPECIAL QUASI RANDOM STRUCTURES (SQS) AND DENSITY FUNCTIONAL THEORY (DFT) TO UNVEIL THE STRUCTURAL AND ELECTRONIC PROPERTIES OF ZNO DOPED WITH AG

ALFENAS/MG
2025

IORRAN VIEIRA BATISTA

USING SPECIAL QUASI RANDOM STRUCTURES (SQS) AND DENSITY FUNCTIONAL THEORY (DFT) TO UNVEIL THE STRUCTURAL AND ELECTRONIC PROPERTIES OF ZNO DOPED WITH AG

Thesis submitted to the Graduate Program in Physics of the Federal University of Alfenas, as part of the requirements for obtaining the degree of Master in Physics.Concentration area: Computational Simulation and Modeling of Molecules, Fluids, and Solids. Advisor: Prof. Dr. Mariama Rebello de Sousa Dias. Coadvisor: Prof. Dr. Anibal Thiago Bezerra.

ALFENAS/MG

2025

Sistema de Bibliotecas da Universidade Federal de Alfenas
Biblioteca Central

Batista, Iorran Vieira.
Using special quasirandom structures (SQS) and density functional theory (DFT) to unveil the structural and electronic properties of ZnO doped with Ag / Iorran Vieira Batista. - Alfenas, MG, 2025.
83 f. : il. -

Orientador(a): Mariama Rebello de Sousa Dias.
Dissertação (Mestrado em Física) - Universidade Federal de Alfenas, Alfenas, MG, 2025.
Bibliografia.

1. Semiconductors. 2. Doping. 3. Density Functional Theory. 4. Zinc Oxide. I. Dias, Mariama Rebello de Sousa, orient. II. Título.

Ficha gerada automaticamente com dados fornecidos pelo autor.

IORRAN VIEIRA BATISTA

USING SPECIAL QUASI RANDOM STRUCTURES (SQS) AND DENSITY FUNCTIONAL THEORY (DFT) TO UNVEIL THE STRUCTURAL AND ELECTRONIC PROPERTIES OF ZNO DOPED WITH AG

A Presidente da banca examinadora abaixo assina a aprovação da Dissertação apresentada como parte dos requisitos para a obtenção do título de Mestre em Física pela Universidade Federal de Alfenas. Área de concentração: Simulação e Modelagem Computacional de Moléculas, Fluidos e Sólidos.

Aprovada em: 19 de agosto de 2025.

Profa. Dra. Mariama Rebello de Sousa Dias

Presidente da Banca Examinadora

Instituição: University of Richmond

Prof. Dr. Marcio Peron Franco de Godoy

Instituição: Universidade Federal de São Carlos

Prof. Dr. Ihosvany Camps Rodriguez

Instituição: Universidade Federal de Alfenas

To my parents and my sister, who have always been the foundation of my journey and the reason for my greatest achievements.

ACKNOWLEDGMENTS

First and foremost, I thank God for granting me the wisdom to overcome every challenge, but above all, for blessing me with the family I have.

I express my deepest gratitude to my parents for their unwavering encouragement. You taught me that education is the ultimate tool to transform one's reality. Thank you for your tireless dedication and for being by my side, traveling countless kilometers to ensure I could reach school and pursue my dreams.

To my sister, thank you for everything you have taught me and for believing in my potential even during the moments when I doubted myself. Your support has been my strength.

I am also grateful to all the teachers and education professionals who have been part of my path. I would like to offer a special thanks to Anibal and Dr. Dias for introducing me to a brand-new world that I have truly come to love.

This study was financed in part by the Coordenação de Aperfeiçoamento de Pessoal de Nível Superior - Brasil (CAPES) - Finance Code 001.

ABSTRACT

Zinc oxide (ZnO) has emerged as an optimal candidate for optoelectronic applications due to its wide band gap (3.3 eV), high exciton binding energy, and versatile properties, including variations in conductivity, piezoelectricity, and optical transparency. However, to fully integrate ZnO into next-generation devices, we must obtain a compatible *p*-type material. One promising route is to dope ZnO with atoms such as silver (Ag), but that has been a challenge because those systems are not stable and sometimes exhibit *n*-type behavior. To understand the nature of such behavior, we perform first-principles calculations based on density functional theory (DFT), employing the Quantum Espresso (QE) package, to study the structural and optoelectronic properties of ZnO doped with Ag. We use the Norm-Conserving (NC) pseudopotential to describe the wavefunctions and charge densities. We calculate the density of states (DOS) and the band structure using the exchange-correlation functional in the generalized gradient approximation (GGA) with the Perdew-Burke-Ernzerhof (PBE) parameterization. For undoped systems, We performed calculations for pure ZnO cells containing 4, 32, 72, and 108 atoms. Based on these results, we chose to proceed with Ag doping in the 72-atom cell. With 4 atoms, we find that the band gap is 0.71, the top of the valence band is characterized by the orbital *p* of the Oxygen (O) atom, and the bottom of the conduction band is Zn-*s* in nature. For a supercell of 72 atoms, we first ensure that the system corresponds to a physical one via the special quasirandom structure (SQS) method. Next, we evaluate how Ag doping affects the electronic and optical properties of the system. We present results for eight different doping concentrations: 1.%, 3%, 4%, 5%, 7%, 8%, 10%, and 11%. Here, we generate doped structures in three different ways: by randomly replacing Zn atoms with Ag in the supercell of ZnO, the SQS-Build approach, and via the SQS method. For the first case, we observe an Ag cluster formation in the structure, and the band indicates that the system is a metal. Using the SQS method, we observed that it remains a semiconductor, after which it undergoes a significant change in the band gap and begins to transform into a metal. Finally, to validate our results, we compare them with experimental ones, and we see that SQS, it does provide a good visualization of the atomic arrangement, the band gap qualitatively is in agreement with the literature, and the behavior of the doped system is in agreement with experimental results.

Keywords: semiconductors; doping; density functional theory; zinc oxide.

RESUMO

O óxido de zinco (ZnO) tem se destacado como um candidato ideal para aplicações optoeletrônicas devido ao seu amplo gap de energia (3,3 eV), alta energia de ligação do éxciton e propriedades versáteis, incluindo variações na condutividade, piezoeletricidade e transparência óptica. No entanto, para integrar completamente o ZnO em dispositivos de próxima geração, é necessário obter um material do tipo p compatível. Uma rota promissora é a dopagem do ZnO com átomos como a prata (Ag), porém isso tem sido desafiador, uma vez que esses sistemas não são estáveis e, por vezes, apresentam comportamento do tipo n. Para compreender a natureza desse comportamento, realizamos cálculos de primeiros princípios baseados na teoria do funcional da densidade (DFT), utilizando o pacote Quantum ESPRESSO (QE), com o objetivo de estudar as propriedades estruturais e optoeletrônicas do ZnO dopado com Ag. Utilizamos pseudopotenciais do tipo norma conservada (NC) para descrever as funções de onda e densidades de carga. Calculamos a densidade de estados (DOS) e a estrutura de bandas utilizando o funcional de troca e correlação na aproximação do gradiente generalizado (GGA), com a parametrização de Perdew-Burke-Ernzerhof (PBE). Para sistemas não dopados, realizamos cálculos para células puras de ZnO contendo 4, 32, 72 e 108 átomos. Com base nesses resultados, optamos por prosseguir com a dopagem de Ag na célula de 72 átomos. Para a célula com 4 átomos, encontramos um gap de energia de 0,71 eV, onde o topo da banda de valência é caracterizado pelos orbitais p do oxigênio (O), e o fundo da banda de condução possui caráter Zn-s. Para a supercélula de 72 átomos, inicialmente garantimos que o sistema represente uma configuração física realista por meio do método de Estruturas Quase-Aleatórias Especiais (SQS). Em seguida, avaliamos como a dopagem com Ag afeta as propriedades eletrônicas e ópticas do sistema. Apresentamos resultados para oito diferentes concentrações de dopagem: 1%, 3%, 4%, 5%, 7%, 8%, 10% e 11%. As estruturas dopadas foram geradas de três maneiras distintas: substituição aleatória de átomos de Zn por Ag na supercélula, abordagem SQS-Build e método SQS. No primeiro caso, observamos a formação de aglomerados de Ag na estrutura, e a estrutura de bandas indica comportamento metálico. Utilizando o método SQS, observamos que o sistema permanece semicondutor, passando posteriormente por uma mudança significativa no gap de energia, tendendo a um comportamento metálico. Por fim, para validar nossos resultados, realizamos comparações com dados experimentais. Observamos que o método SQS fornece uma boa representação do arranjo atômico, o gap de energia apresenta concordância qualitativa com a literatura, e o comportamento do sistema dopado está de acordo com resultados experimentais.

Palavras-chave: semicondutores; dopagem; teoria do funcional da densidade; óxido de zinco.

CONTENTS

1 INTRODUCTION

In recent years, wide-bandgap semiconductors have received much attention due to their potential applications in optoelectronic devices in the short-wavelength and ultraviolet (UV) regions of the electromagnetic spectrum. Among these semiconductors [1], ZnSe, ZnS, SiC, GaN, SnO_2, and ZnO have shown similar properties in terms of crystal structures and bandgaps. Although GaN is considered the best candidate for optoelectronic devices, ZnO offers significant advantages for LEDs and Laser Diodes (LDs) due to its wide and direct bandgap and a high excitonic binding energy [2]. Additionally, the lattice constant compatibility with GaN enables the use of ZnO as a substrate in GaN-based devices [3]. ZnO exhibits excellent radiation resistance, making it suitable for space applications and high-energy radiation environments [4]. Its bandgap energy can be adjusted through alloying processes, enabling its use in heterostructured LEDs and quantum well lasers [5]. These features make ZnO a promising candidate for fabricating nanostructures with diverse applications.

For a century and a half, ZnO powder has been a principal material used in white paint pigments and industrial processing chemicals. It was not until the mid-20th century that a resurgence of interest in ZnO emerged, driven by the recognition of its unique and promising properties. These included the production of the first brass metal, the development of purified ZnO for medical purposes, and even attempts by early alchemists to transmute base metals into gold. This renewed interest was fueled by both the scientific community and industry leaders [6]. These properties hold significant potential for diverse applications beyond their traditional uses. ZnO has emerged as a front-runner for the next generation of electronic devices. Additionally, its biocompatible nature enables medical device applications. Recent advances in areas such as crystal growth, processing, and doping of ZnO have further accentuated its potential across various technological domains, including solar cells [7], gas sensors [8], and photocatalysts [9, 10].

The study of ZnO experienced notable peaks in interest during 1990 and 2010 [10], with over 5,000 publications in 2010 referencing ZnO in their title, abstract, or keywords [11]. In 2024, this number doubled, reaching 10,172 articles, as observed in [12]. This occurred because ZnO possesses ideal optoelectronic properties, depending on doping, including conductivity ranging from metallic to insulating, high transparency, piezoelectricity, wide band-gap semiconductivity, room-temperature ferromagnetism, and significant magneto-optical and chemical sensing effects [1, 2, 13–16]. Because of its promising applications in next-generation optoelectronic devices, ZnO has garnered considerable attention among metal oxide semiconductors (MOS). Pure ZnO in a wurtzite (WZ) phase is characterized by a direct bandgap (3.3 eV) [1] with a large exciton binding energy of 60 meV [17]. These properties render it particularly intriguing as a laser material, with the potential for exciton recombination at room temperature or

even higher. However, to obtain fully operable devices based on ZnO, one must find a compatible *p*-type material. Several groups have pursued this challenge [18], and substantial progress has been made.

ZnO crystallizes in the WZ structure and probably has the widest variety of different nanostructures [19, 20]. The wurtzite structure exhibits basic hexagonal symmetry. The two hexagonal close-packed (HPC) lattices have the same axis (a_3-axis), but one of them is displaced with respect to the other. The WZ structure may be considered as an HPC structure with a basis of two atoms. It also exhibits uniaxial crystal symmetry, which is compatible with most piezoelectric and pyroelectric materials [21]. The optical properties of ZnO are also influenced by its piezoelectric and pyroelectric characteristics, as these effects can modify the local electronic structure and internal electric fields within the material. Such changes can affect light absorption, emission, and refractive index, making ZnO suitable for applications in sensors, actuators, and energy-harvesting devices that integrate both electrical and optical functionalities.

Due to its use in various fields and its inorganic nature, it may be beneficial to further enhance the functionalities of ZnO rather than improve existing ones. With the final objective of designing a multi-functional system, the need for doping arises [22]. Doping represents a valuable approach to tune various ZnO properties. It consists of the insertion of a specific ion into a crystal lattice, like in our case, the Ag^{+1}. Another example is Au-doped ZnO nanoparticles, which, upon investigation, revealed that doping leads to the presence of additional weak luminescence peaks in the visible spectral range, accompanied by an increase in intensity. The authors Marco Carofiglio et al. conducted research that showed doping with Ag and Au ions was suitable for increasing the photocatalytic properties of ZnO; however, only Ag-doped ZnO exhibited enhanced antifungal activity. A X-ray analysis revealed that Ag-doped ZnO solidified in a hexagonal WZ structure [23]. The first-principles calculation returned Ag deep levels in ZnO with an n-type behavior [24]. Conversely, in ZnO structures with grain boundaries, p-type nature via shallow states is dominant. Hosseini et al. suggested that silver doping reduced the energy gap and controlled the luminescence properties, thereby producing p-type conductivity, as indicated by a red shift in the absorption edge measurements.

In this work, we present a comprehensive study of the optoelectronic properties of ZnO doped with Ag (ZnO:Ag) using Density Functional Theory (DFT). In Chapter 2, we introduce the theoretical foundations of DFT, starting with fundamental quantum mechanics concepts, including the Hohenberg-Kohn theorems and the Kohn-Sham equations. We also address optimization techniques and the Perdew-Burke-Ernzerhof (PBE) approximation. Chapter 3 focuses on the physics of the ZnO crystal structure, presenting essential concepts from solid-state physics, the hexagonal close-packed (HCP) structure, and the *k*-space Brillouin zones relevant to semiconductor behavior. Chapter 4 discusses the general properties of ZnO, with emphasis on structural, electronic, and optical characteristics, including the role of intrinsic defects. In Chapter 5, we describe the computational methodology adopted. We performed structural and electronic calculations for pure ZnO supercells containing 4, 32, 72, and 108 atoms. Based on

a balance between accuracy and computational cost, the 72-atom supercell was chosen for Ag doping studies. Doping was introduced by replacing Zn atoms with Ag using three different approaches: (i) random substitution, (ii) the SQS-Build method, and (iii) the Special Quasirandom Structures (SQS) approach. We also provide an overview of the QUANTUM ESPRESSO package employed for DFT simulations, along with the exchange-correlation approximations used. In Chapter 6, we present and analyze the results obtained from these different doping strategies, discussing their impact on the structural, electronic, and optical properties of ZnO:Ag. Finally, Chapter 7 offers concluding remarks and perspectives, summarizing the main findings and proposing future directions.

1.1 OBJECTIVES

The objective of this study is to investigate the structural and electronic properties of ZnO doped with Ag atoms at different doping concentrations. Using first-principles calculations based on DFT with the QE package, we aim to understand the impact of doping on properties such as the band structure, density of states (DOS). Additionally, the study examines the efficacy of the SQS method compared to the random substitution and SQS-build of Zn atoms with Ag on the electronic behavior, including the transition from semiconductor to metallic behavior. It compares the obtained results with experimental data available in the literature.

1.2 GENERAL PROPERTIES OF ZnO

ZnO is a II-VI compound semiconductor with properties that make it attractive for a wide range of applications. The general properties of ZnO can be divided into structural, electronic, and optical aspects.

1.2.1 Structural Properties

Most group II-VI binary compound semiconductors crystallize in cubic zinc blende (ZB), rock salt, or hexagonal WZ structures. ZnO crystallizes in the WZ structure, where each anion is surrounded by four cations at the corners of a tetrahedron, and vice versa (Figure 1.1). The ZnO crystal has a hexagonal unit cell with two lattice parameters: a and c. For ZnO, these parameters are $a = 3.25$ Å and $c = 5.21$ Å [21]. The WZ structure consists of a hexagonal close-packed (HCP) array of oxygen anions with metal cations occupying half of the tetrahedral interstices.

The table **??** summarizes the main structural and physical properties of wurtzite ZnO, the most stable crystalline phase of zinc oxide under ambient conditions. ZnO is a II-VI com-

Figure 1.1: Crystalline structure of wurtzite ZnO

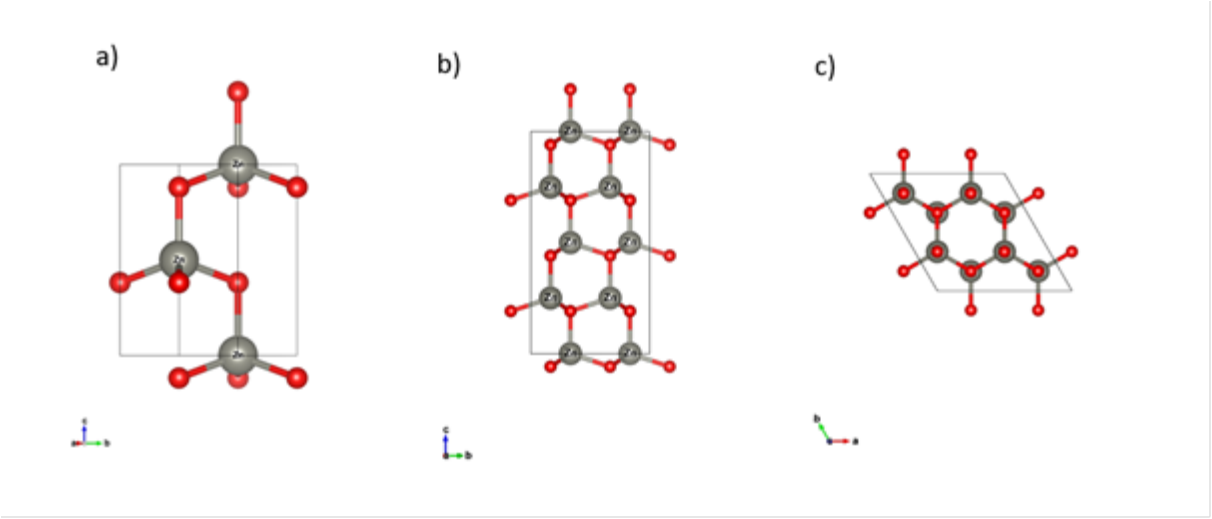

Source: Elaborated by the author (2025)
Note: Zinc (Zn) atoms occupy the lattice positions at the corners of the hexagonal unit cell. Oxygen (O) atoms are located at the center of each hexagonal face and within the unit cell. (b) View along the a-axis. (c) View along the c-axis. The gray and red spheres represent Zn and O atoms, respectively.

pound semiconductor with intrinsic *n*-type behavior, typically associated with native defects such as oxygen vacancies and zinc interstitials. Its crystal structure is hexagonal, belonging to the $P6_3mc$ space group, and is both *polar* and *non-centrosymmetric* — features that enable piezoelectric and pyroelectric behavior. The Zn–O bond lengths vary slightly along the crystallographic axes (1.90 Å along the *a*-axis and 1.98 Å along the *c*-axis), reflecting the anisotropic nature of the wurtzite lattice. The lattice constants are $a = 3.249\,\text{Å}$ and $c = 5.206\,\text{Å}$, with a unit cell volume of 47.63 Å^3 and a calculated density of 5.606 g/cm^3.

Electronically, ZnO exhibits a *direct bandgap* of 3.37 eV at 300 K, making it suitable for optoelectronic applications such as UV LEDs and photodetectors. Furthermore, it has a high exciton binding energy of 60 meV, which ensures exciton stability at room temperature, an important factor for optical efficiency. These properties, combined with its multifunctional characteristics, position ZnO as a promising material for use in electronics, photonics, and sensing technologies.

1.2.2 Electronic Properties

Following the pioneering theoretical work on the band structure calculation of ZnO by Rössler in 1969, which employed the Green's function through the Korringa-Kohn-Rostoker (KKR) method [25, 26], numerous experimental studies [13, 27–30] have investigated the WZ ZnO structure. These experiments revealed significant discrepancies between Rössler's predicted bulk electronic structure and the experimental observations. The first experimental data

Table 1.1: Structural, electronic, and physical properties of wurtzite ZnO

Material properties	**Material parameters**
Material type	II-VI compound semiconductor (n-type)
Crystal structure and type	Hexagonal, P 63 mc space group, polar and non-centrosymmetric
Zn-O distance along the a-axis	1.90 Å
Zn-O distance along the c-axis	1.98 Å
Lattice parameter	$a = 3.249$ Å and $c = 5.206$ Å
Unit cell volume	47.63 Å^3
Density	5.606 g cm^{-3}
Bandgap	$\sim$3.37 eV at 300K, direct
Exciton binding energy/diameter	$\sim$60 meV at $\sim$300K/$\sim$2 nm
Other associated properties	Piezoelectric, pyroelectric

Source: Adapted from NANDI et al. (2021)
Note: The material exhibits a hexagonal structure with polar and non-centrosymmetric characteristics, a direct wide bandgap, and piezoelectric/pyroelectric behavior, making it suitable for optoelectronic applications.

on the energy levels of core electrons in ZnO were obtained using X-ray induced photoemission spectroscopy [26, 27], which unambiguously identified the position of the Zn 3d level. This study highlighted a discrepancy between the experimentally measured and theoretically calculated energy values, which was found to be dependent on angular momentum.

Further investigations using ultraviolet (UV) photoemission spectroscopy on hexagonal ZnO, cleaved under vacuum, located the Zn 3d core level approximately 7.5 eV below the valence band maximum (VBM) [15, 26–28]. This value is 3 eV lower than the prediction made by Rössler's band calculation. Consistent results were obtained from X-ray photoemission measurements, which reported Zn 3d core levels at 8.5 eV [31] and 8.81 eV [30] below the VBM.

In subsequent years, theoretical approaches such as the local density approximation and tight-binding methods [32–35] were employed, treating the Zn 3d states as core levels to simplify calculations. While these methods achieved reasonable agreement with qualitative valence band dispersions, they failed to accurately predict the quantitative position of the Zn 3d states. With advances in computational capabilities, more sophisticated theoretical models began to incorporate the Zn 3d levels as part of the valence band states [36–39]. These advanced methods not only provided a more precise estimate of the Zn 3d state position but also accounted for their significant influence on the s- and p-derived valence bands.

The resurgence of interest in ZnO in the 1990s can be attributed to the successful commercialization of optoelectronic and electronic devices based on GaN. ZnO shares several properties analogous to those of GaN, such as its wide bandgap, high electron mobility, and abundance, making it an ideal choice for optoelectronic device technology [40].

Materials with direct or indirect band gaps exhibit different absorption and emission char-

acteristics [41]. As a direct and wide bandgap material, ZnO is attracting significant attention for various electronic and optoelectronic applications. The large bandgap offers numerous advantages, including high-temperature and high-power operation, lower noise generation, higher breakdown voltages, and the ability to sustain large electric fields. Electron transport in semiconductors is influenced by both low- and high-electric fields. At low fields, the energy gained by electrons is negligible compared to their thermal energy, so their energy distribution remains unaffected, and electron mobility remains independent of the applied electric field, following Ohm's law. However, in higher fields, the electrons gain sufficient energy to become 'hot' electrons with a temperature higher than that of the lattice, leading to significant changes in the electron distribution function. Additionally, when device dimensions shrink to the sub-micron range, transient transport phenomena, such as ballistic transport and velocity overshoot, become prominent, allowing devices to operate at higher frequencies than would be expected from simple scaling.

The electronic properties of ZnO are governed by its WZ crystal structure, where Zn and O atoms form covalent bonds through electrostatic interactions between Zn^{2+} and O^{2-} ions. The material has a direct bandgap of 3.44 eV at 30 K and 3.37 eV at room temperature, making it suitable for ultraviolet (UV) light-emitting devices.

The band structure helps classify materials as semiconductors or insulators based on the presence or absence of an energy bandgap. Semiconductors, characterized by a small bandgap, can have their electrical conductivity significantly influenced by thermal excitation or doping. On the other hand, insulators possess a large band gap, resulting in very low electrical conductivity. Additionally, it enables the determination of energy gaps between different bands, such as the bandgap between the valence band (VB) and conduction band (CB). This information is crucial for understanding optical properties and influencing thermal and electrical transport properties of materials.

The density of states quantifies the number of electronic states that exist in the tip per unit of energy. For semiconductors, the DOS near the CB and VB shows that states are available within the bandgap but are typically inaccessible at room temperature, unless thermally excited or doped. The distribution of states in the bandgap can influence the conductivity of the material, determining whether it behaves as an n-type or p-type semiconductor [40, 42–44].

In this work, we will calculate the band structure and DOS of 4, 32, 72, and 108 atom systems for pure ZnO, as well as for different compositions of doped structures using the random, SQS-build, and SQS methods. All systems will be optimized in terms of crystal structure, allowing both atomic positions and unit cell dimensions to adjust in order to minimize the total energy. Then, we will perform Self-Consistent Field (SCF) calculations to determine the electronic structure by iterating the wavefunctions and electron density until convergence. Based on the converged electron density, we will carry out Non-Self-Consistent Field (NSCF) calculations, from which we will extract electronic properties such as energy bands, density of states, and optical properties. In the case of random doping, we will expand the ZnO structure from 4

atoms and randomly replace Zn atoms with Ag

1.2.3 Optical Properties

ZnO is known for its remarkable optical properties. This allows ZnO to be utilized in various optoelectronic applications, including UV light-emitting diodes (LEDs), laser diodes, and photodetectors. The exciton binding energy of ZnO is approximately 60 meV at room temperature, which is relatively high compared to other semiconductors, making it an ideal material for applications that require stable excitonic behavior.

Inside a periodic solid, the electronic wavefunctions are described as Bloch functions, which are a product of a plane wave and a periodic function that accounts for the crystal lattice symmetry [45]. The energy of the system can be determined as a functional of the density. The total energy functional of the system can be obtained by the equation [46]:

$$E[n(\vec{r})] = T_s[n(\vec{r})] + E_{ne}[n(\vec{r})] + E_H[n(\vec{r})] + E_{xc}[n(\vec{r})]$$

where $T_s[n(\vec{r})]$ represents the kinetic energy of the non-interacting electron system, $E_{ne}[n(\vec{r})]$ is the ion-electron energy, $E_H[n(\vec{r})]$ is the electron-electron energy, and $E_{xc}[n(\vec{r})]$ is the exchange-correlation term. The exchange-correlation potential $E_{xc}[n]$ introduces the many-body interacting problem into the equation.

Interaction occurs between photons and electrons in the material, and transitions between occupied and unoccupied states are driven by the electric field of the incident photon. Resulting spectra from these transitions can be described as a joint DOS between the VB and CB. The optical response of a material to the external electromagnetic field at all energy levels can be described by the complex dielectric function $\tilde{\varepsilon}(\hbar\omega)$ as [47],

$$\varepsilon(E)_2 = \varepsilon_1(E) + i\varepsilon_2(E), \tag{1.1}$$

where $\varepsilon_1(E)$ and $\varepsilon_2(E)$ are the real and imaginary parts of the dielectric function. Real part of the dielectric function $\epsilon_1(E)$, corresponds to the dispersion of the incident photons by the material, while the imaginary part $\varepsilon_2(E)$, describes the energy absorbed by the material. There are two contributions to the complex dielectric function $\varepsilon(E)$, namely intraband and interband transitions. Thus, ε_2 can be calculated using the following expression [48]

$$\varepsilon_2(E) = \frac{4\pi^2 e^2 \hbar^2}{m^2 E^2} \sum_{i,j} \int_i \langle i|M|^2 j\rangle f_i \delta(E_f - E_i - E)\, d^3k. \tag{1.2}$$

M is the dipole matrix, i and j are initial and final states, respectively, f_i is the Fermi distribution function for the ith state, E_i is the energy of the electron in the ith state,and $\hbar\omega$ is the energy of the incident photon. The real part $\epsilon_1(\omega)$ of the dielectric function can be found from its corresponding $\epsilon_2(\omega)$ by the Kramers-Kronig transformation in the form [49–51]:

$$\varepsilon_1(\omega) = 1 + \frac{2}{\pi}\mathcal{P}\int_0^\infty \frac{\omega'\varepsilon_2(\omega')}{\omega'^2 - \omega^2}d\omega'. \tag{1.3}$$

In this equation, $\mathcal{P}$ denotes the principal value of the Cauchy integral.

These equations are known as the Kramers-Kronig relations, which connect the real part of an analytic complex function to an integral containing the imaginary part of the function and vice versa. By knowing both the imaginary and real parts of the dielectric tensor, it is possible to calculate important optical properties. For example, the absorption coefficient $(\alpha(\omega))$ describes the fraction of energy absorbed from the incident radiation as it penetrates the crystal.

$$\alpha(E) = \frac{E}{\sqrt{2\left(\sqrt{\varepsilon_1^2(E) + \varepsilon_2^2(E)} - 2\varepsilon_1(E)\right)}}. \tag{1.4}$$

Also we can obtain the refractive index, which governs how light interacts with the material at interfaces where there is a change in optical properties.

$$n(\omega) = \sqrt{\left(\frac{(\sqrt{\varepsilon_1^2(E) + \varepsilon_2^2(E)} + \varepsilon_1(E)}{2}\right)}. \tag{1.5}$$

where ε_2 is obtained directly from the electronic structure.

1.2.4 Defects of ZnO

The control of defects and associated charge carriers is of paramount importance in applications that exploit the wide range of properties of doped ZnO [5]. Solid surfaces contain segregated impurities, adsorbed gases that act as sources and sinks of electrons, and associated space charge regions. In nanostructured ZnO (as well as in other materials), the small length scales and large surface-to-volume ratio mean that surface defects play a stronger role in controlling properties. Also, critically important to understand defects in ZnO doped with aliovalent ions, either purposefully for achieving a certain functionality or through accidental doping during the growth process [52].

It is relevant to understand the relative dominance of carriers introduced by doping over

native defects. An example is the formation of p-n junctions of ZnO for ultraviolet (UV) lasers. Here, achieving p-type ZnO with sufficient carrier concentration in a reproducible way relies on striking a careful balance between control of extrinsic doping and intrinsic defect concentration [53]. Before considering the defect structure of ZnO in more detail, it is substantial to realize that ZnO has a relatively open structure, with a hexagonal close-packed lattice where Zn atoms occupy half of the tetrahedral sites. All the octahedral sites are empty. Hence, there are plenty of sites for ZnO to accommodate intrinsic (namely, Zn interstitials) defects and extrinsic dopants. There are several intrinsic defects with different ionization energies. The Kröger Vink notation uses i= interstitial site, Zn = zinc, O = oxygen, and V = vacancy. **Oxygen vacancy ($\mathbf{V_O}$)** is the most common intrinsic defect in ZnO. It occurs when an oxygen atom is missing from the crystal lattice, resulting in a donor defect (electron donor). **Zinc Interstitial ($\mathbf{Zn_i}$)** it is a zinc atom that occupies a position in the lattice where it normally should not be. The presence of Zn_i acts as an acceptor defect (electron acceptor).

The terms indicate the atomic sites, and superscripted terms indicate charges, where a dot indicates a positive charge, a prime indicates a negative charge, and a cross indicates zero charges, with the charges in proportion to the number of symbols. Understanding and controlling these defects in ZnO is crucial for tailoring its properties to various applications, such as transparent conductive films, optoelectronics, sensors, and photocatalysis. Researchers and engineers often manipulate the defect structure through growth techniques, doping, and annealing processes to achieve desired material characteristics. Due to the different ionization energies, the relative concentrations of the various defects depend strongly on temperature [52]. In order to attain the potential offered by ZnO, both high-quality n-type ZnO and p-type ZnO are essential, but it is difficult to obtain the bipolar carrier doping, both n- and p-types, in wide-bandgap semiconductors. N-type behavior in ZnO is associated with a zinc-rich composition within the wurtzite (WZ) crystal structure. Due to this excess, ZnO is a non-stoichiometric compound and n-type semiconductor. Group III elements Al, Ga, and In as substitutional elements for Zn and group VII elements can be used as n-type dopants [54, 55]. P-type doping is very difficult to obtain in wide band gap semiconductors because the acceptors in ZnO can take place from both lattice defects and impurity atoms. The oxygen interstitial O_i and zinc vacancy V_zn are both known to be acceptors in ZnO. Deep impurity level can also be source of doping problem, causing large resistance to the formation of shallow acceptors.

2 METHODS

This section outlines the methods used in Density Functional Theory (DFT) simulations, including the treatment of crystalline and semiconductor materials, periodic boundary conditions, and the reciprocal space approach. It also covers key concepts like k-space and Brillouin zones, as well as the role of pseudopotentials and GGA approximations. The implementation details using Quantum ESPRESSO are presented, focusing on the hexagonal closed-packed (HCP) structure and the use of Special Quasirandom Structures for supercells.

2.1 INTRODUCTIONS

We used DFT to calculate their structural and electronic properties. The plane-wave self-consistent field (PWSCF) code is employed as our first principle energy code. PWSCF is a first principle energy code that uses norm-conserved pseudopotential (PP) within DFT. At first, an initial guess for the electron density is assumed, which is required for the calculation of $V_{eff}(r)$, the diagonalization of the Kohn-Sham equations, and the subsequent evaluation of $(\rho(r))$ along with total minimum energy. As long as the convergence criterion is not fulfilled, the numerical procedure is continued with the last $(\rho(r))$ instead of the initial guess. When criterion is satisfied, various output quantities are computed like energy of system stress.

We used Density Functional Theory (DFT) to calculate their structural and electronic properties. The plane-wave self-consistent field (PWSCF) code, part of the **Quantum ESPRESSO** package, is employed as our first-principles energy code. PWSCF is a first-principles energy code that uses norm-conserving pseudopotentials (PP) within DFT.

At first, an initial guess for the electron density is assumed, which is required for the calculation of $V_{eff}(r)$, the diagonalization of the Kohn-Sham equations, and the subsequent evaluation of $\rho(r)$ along with the total minimum energy. As long as the convergence criterion is not fulfilled, the numerical procedure is continued with the last $\rho(r)$ instead of the initial guess. When the criterion is satisfied, various output quantities are computed, such as the system's energy and stress. In what follows, details of the calculations are presented.

2.2 CRYSTALLINE MATERIALS

We are going to introduce concepts, our general objectives in this chapter is to understand the macroscopic properties of solids on a microscopic level focusing on a semiconductor as ZnO. A crystal is described in real space in terms of the primitive lattice vectors $\mathbf{a}_1$, $\mathbf{a}_2$, and $\mathbf{a}_3$

and the positions of atoms inside a primitive unit cell (PUC). The lattice vectors $\mathbf{R}$ are formed by all possible combinations of the primitive lattice vectors, multiplied by integers [56]:

$$\mathbf{R} = n_1\mathbf{a}_1 + n_2\mathbf{a}_2 + n_3\mathbf{a}_3, \quad n_1, n_2, n_3 : \text{integers} \tag{2.1}$$

The lattice vectors connect all equivalent points in space; this set of points is referred to as the “ravis lattice". The PUC is defined as the volume enclosed by the three primitive lattice vector [56]:

$$\Omega_{PUC} = |\mathbf{a}_1.(\mathbf{a}_2 \times \mathbf{a}_3)| \tag{2.2}$$

This is a useful definition: we only need to know all relevant real-space functions for $\mathbf{r}$ within the PUC since, due to the periodicity of the crystal, these functions have the same value at an equivalent point of any other unit cell related to the PUC by a translation $\mathbf{R}$. There can be one or many atoms inside the primitive unit cell, and the origin of the coordinate system can be located at any position in space; for convenience, it is often chosen to be the position of one of the atoms in the PUC [56].

2.2.1 Periodic Boundary Conditions

Due to the periodicity of the lattice, any such function need only be studied for r within the PUC. This statement applied to the single-particle wavefunctions is known as “Bloch’s theorem”. The Bloch’s theorem say when the potential in the single-particle hamiltonian has the translational periodicity of the Bravais lattice only crystals with one or two atoms per unit cell are considered; the position of one atom in the PUC is always assumed to be at the origin; when there are two atoms in the PUC, the position of the second atom t_2 is given with respect to the origin. All vectors are given in cartesian coordinates and in terms of the standard lattice parameter a, the side of the conventional cube or parallelpiped. For the Hexagonal Closed-packed Structure (HCP) lattice, a second parameter is required, namely the c/a ratio. d_{NN} is the distance between nearest neighbors in terms of the lattice constant a.

2.2.2 Reciprocal Space

In the study of crystalline materials, reciprocal space plays a fundamental role in describing periodic structures. The reciprocal lattice vectors $\mathbf{b}_1$, $\mathbf{b}_2$, and $\mathbf{b}_3$ are defined in terms of the primitive lattice vectors in real space:

$$\mathbf{b}_1 = 2\pi \frac{\mathbf{a}_2 \times \mathbf{a}_3}{\mathbf{a}_1 \cdot (\mathbf{a}_2 \times \mathbf{a}_3)}, \quad \mathbf{b}_2 = 2\pi \frac{\mathbf{a}_3 \times \mathbf{a}_1}{\mathbf{a}_1 \cdot (\mathbf{a}_2 \times \mathbf{a}_3)}, \quad \mathbf{b}_3 = 2\pi \frac{\mathbf{a}_1 \times \mathbf{a}_2}{\mathbf{a}_1 \cdot (\mathbf{a}_2 \times \mathbf{a}_3)} \tag{2.3}$$

The reciprocal lattice is useful for describing wave vectors associated with the periodic potential of the crystal. Each point in the reciprocal space corresponds to a plane wave with a wavelength inversely proportional to the distance in real space. This framework is essential in the application of Bloch's theorem and the interpretation of diffraction patterns.

Below is a table showing the types of lattice and the crystal lattice properties such as lattice parameters like the ones mentioned above: $a, t_2, c/a$ and D_{NN}.

Below is a table showing the types of lattice and the crystal lattice properties as lattice parameters like the one mentioned above: $a, t_2, c/a$ and D_{NN}

Table 2.1: Properties of Different Crystal Lattices

Lattice	$\mathbf{a}_1$	$\mathbf{a}_2$	$\mathbf{a}_3$	t_2	c/a	d_{NN}
Cubic	$(a, 0, 0)$	$(0, a, 0)$	$(0, 0, a)$	-	-	a
BCC	$\left(\frac{a}{2}, -\frac{a}{2}, -\frac{a}{2}\right)$	$\left(\frac{a}{2}, \frac{a}{2}, -\frac{a}{2}\right)$	$\left(\frac{a}{2}, -\frac{a}{2}, \frac{a}{2}\right)$	-	-	$\frac{a\sqrt{3}}{2}$
FCC	$\left(\frac{a}{2}, \frac{a}{2}, 0\right)$	$\left(\frac{a}{2}, 0, \frac{a}{2}\right)$	$\left(0, \frac{a}{2}, \frac{a}{2}\right)$	-	-	$\frac{a}{\sqrt{2}}$
HCP	$\left(\frac{a}{2}, \frac{\sqrt{3}a}{2}, 0\right)$	$\left(\frac{a}{2}, \frac{\sqrt{3}a}{2}, 0\right)$	$(0, 0, c)$	$\left(\frac{a}{2}, \frac{a}{2\sqrt{3}}, \frac{c}{2}\right)$	$\sqrt{\frac{8}{3}}$	$\frac{a}{\sqrt{3}}$

Source: Elaborated by the author (2025).

These crystals are illustrated in Figure 2.1.

Figure 2.1: Crystal structures for ZnO properties study

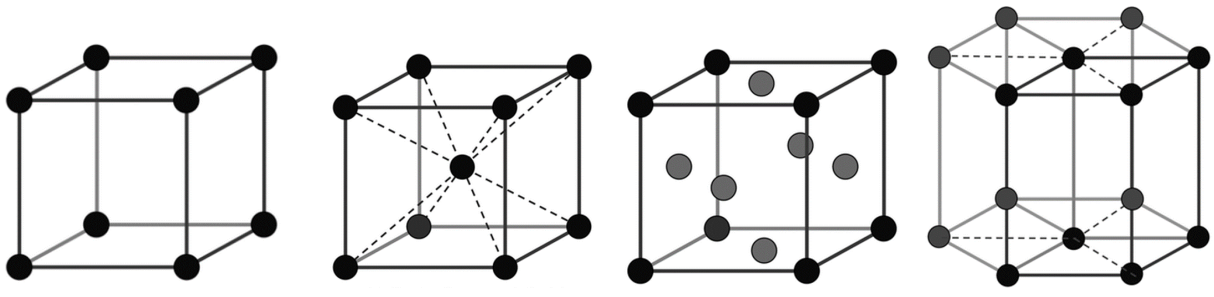

(a) SC (b) BCC (c) FCC (d) HCP

Source: Elaborated by the author (2025).
Note: Comparison of structures shown in Table 2.1: simple cubic (SC), body-centered cubic (BCC), face-centered cubic (FCC), and hexagonal close-packed (HCP). Lattice vectors are indicated by arrows. For the HCP structure, two different symbols (gray and black circles) represent the two atoms in the unit cell.

2.2.2.1 k-space - Brillouin zones

The notions of direct and reciprocal lattices and Brillouin zone are introduced as a mathematical tool for describing the properties of materials which can be considered (to a certain approximation) as perfect crystals, where the atoms are arranged in patterns which repeat themselves periodically. The smallest portion of a crystal from which we can generate the entire solid using rigid translations is called the primitive unit cell, and corresponds to a parallelepiped whose edges are denoted by a_1, a_2 and a_3. These vectors are called the primitive lattice vectors. [57]

Brillouin zones gave the statement of the diffraction condition that is most widely used in solid state physics, which means in the description of electron energy band theory and the elementary excitation of other kinds [58]. The first Brillouin zone is the smallest volume entirely enclosed by planes that are the perpendicular bisectors of the reciprocal lattice vector drawn from the origin. The Brillouin zones are not part of the language of X-ray diffraction analysis of the electronic energy-band structure of crystals.

2.2.3 Semiconductor Materials

Conductors are materials that allow electricity to flow easily through them because they have many free electrons that can move freely within the material. Common examples of conductors are metals such as copper, aluminum, and gold. Insulators, on the other hand, are materials that do not conduct electricity or do so very poorly. They have few or no free electrons, which prevents the movement of electric charge. Examples of insulators include wood, rubber, glass, and plastic. Semiconductors, in contrast, have electrical conductivity that lies between that of conductors and insulators. They do not conduct electricity as well as conductors, but can be made to conduct under certain conditions, such as when doped with impurities or when exposed to external energy like heat or light. They are crucial for electronic device manufacturing, including diodes, transistors, and integrated circuits, due to their compactness, reliability, efficiency, and cost-effectiveness. Semiconductors play a vital role in electronic systems for communication, signal processing, computing, and control in both consumer and industrial markets [59]. In short, the electrical properties of a material are directly linked to the size of the energy bandgap (forbidden region) and its configuration. These characteristics determine whether materials can be classified as conductors, semiconductors, or insulators [45].

The bandgap is the difference in energy between the lowest point of the conduction band and the highest point of the valence band. The lowest point in the conduction ban is called the conduction ban edge; the highest point in the valence band is called valence band edge [45].

The study of semiconductor materials began in the early 19th century. The general idea

behind a semiconductor is that the bandgap between the highest occupied states and the lowest unoccupied states is sufficiently small to get thermally excited electrons at reasonable temperatures [60]. In other words, there is a certain energy band that is completely filled, and the next band at higher energy is completely empty. The highest occupied band and the lowest unoccupied band are called the valence band (VB) and the conduction band (CB), respectively. At finite temperature, the electrons have to be distributed according to the Fermi–Dirac distribution. The most common elemental semiconductors are the group IV elements Si and Ge with their characteristic tetrahedral sp3 bonding. The latter two groups of materials are commonly referred to as III–V and II–VI semiconductors [61].

A very small amount of impurities strongly influences the conductivity of semiconductors, and a precise control of the impurity concentration turns out to be essential for the construction of semiconductor devices. One way to control impurity concentration is by doping the element, which involves adding a very small amount of electrically active impurities [62, 63].

Doping of materials primarily aims to modify or introduce new properties into the matrix [64]. Studies conducted on semiconductors doped with transition metals have shown that it is possible to improve material properties by inserting a dopant ion. Mockenhaupt et al. have described the solubility limit of transition metals in the crystalline lattice of ZnO [65]. This limit can vary significantly depending on the synthesis methodologies employed. The synthesis methodologies used to obtain the materials directly influence the concentration of incorporated dopant, as well as the size and shape of the particles. Therefore, there is an increasing search for synthesis processes that allow obtaining materials under more advantageous synthesis conditions. Works involving the study of materials at the theoretical level are important because they allow assessing how the dopant acts in the structure, as well as providing the basis for improving physical and chemical properties through doping. [66]

The dopant atoms change the conductivity by either donating (giving) electrons to the CB or accepting (taking) electrons from the VB, that is, by generating holes. Therefore, they are called donors and acceptors, respectively. The two types of doping in a semiconductor are called n and p doping, for dopant atoms that give rise to free electrons in the CB and free holes in the VB, respectively. [59]

Acceptor impurities have fewer electrons in the valence band, creating holes as charge carriers. This results in p-type extrinsic semiconductors, where impurity levels are close to the valence band, facilitating electron transfer to the conduction band [64]. Zinc oxide is naturally an intrinsic type-n semiconductor [1], but impurities or defects can alter its conductivity, potentially resulting in p-type extrinsic semiconductor behavior depending on the dopant.

The lattice parameters of a semiconductor usually depend on the following factors: (i) free-electron concentration acting via deformation potential of a conduction-band minimum occupied by these electrons, (ii) concentration of foreign atoms and defects and their difference of ionic radii concerning the substituted matrix ion, (iii) external strains, and (iv) temperature. The lattice parameters of any crystalline material are commonly and most accurately measured by

high-resolution X-ray diffraction. It is need to consider that the periodicity of the lattice is disturbed by many imperfections or defects, ans those imperfection or defects can have influence on mechanical thermal electrical an optical properties of a semiconductor [67]. Usually the lattice parameter of any crystal are measured by high-resolution x-ray ion (HRXRD).

Semiconductor are generally classified by their electrical resistivity at room temperature, with values in the range of 10^{-2} to 10^{9} Ωcm, and strongly dependent on temperature. At absolute zero, a pure, perfect crystal of most semiconductors will be an insulator, if one arbitrarily defines an insulator as having a resistivity above $10^{14}\Omega cm$. Transistor, switchers, diodes, photovoltaic cells, detectors and thermistors are some devices based on semiconductors. A highly purified semiconductor exhibits intrinsic conductivity, as distinguished from the impurity conductivity of less pure specimens. In the intrisic temperature range the electrical properties of a semiconductor are not essentially modified by impurities in the crystal. The conduction band is vacant at absolute zero and is separated by an energy gap E_g from the filled valence band [45, 68].

The intrinsic conductivity and intrinsic carrier concentrations are largely controlled by E_g/K_bT, the ratio of the band gap to the temperature. When this ratio is large, the concentration of intrinsic carriers will be low and the conductivity will be low. The best values of the bandgaps are obtained by optical abortions. In the direct absorption process the threshold of continuous optical absorption at frequency ω_g measures the bandgap $E_g = \hbar\omega_g$. A photon is absorbed by the crystal with the creation of an electron and a hole. In the indirect absorption process, the minimum energygap of the band structure involves electrons and holes separated by substantial wavevector $\mathbf{k}_c$. The bandgap may also be deduced from the conductivity's temperature dependence or carrier concentration in the intrinsic range. The carrier concentration is obtained from measurements of the Hall voltage, sometimes supplemented by conductivity measurements.

When we look at the energy-wavevector relation $\epsilon = (\hbar^2/2m)k^2$ for free electrons, we see that the coefficient of k^2 determines the curvature of ϵ versus k. So, we can say that $1/m$, the reciprocal mass determines the curvature. For electrons in a band there can be regions of unusually high curvature near the band gap at the zone boundary. If the energy gap is smaller than the free electron energy λ at the boundary, the curvature is enhanced by the factor λ/E_g. In semiconductors, the band width, which is like the free electron energy, is of the order of 2 eV, while the bandgap is of the order of 0.2 to 2 eV. In semiconductors it has been possible to determine by cyclotron resonance the effective masses of carrier in the conduction and valence band near the band edges.The perturbation theory of band edges suggest that the electron effective mass should be proportional to the band gap, approximately, for a direct gap crystal.

2.3 PSEUDOPOTENCIAL

Pseudopotentials are used in conjunction with plane wave basis sets because a large number of plane waves is required to expand the wave functions of core electrons, as they exhibit highly oscillatory behavior near the nuclei. Pseudopotentials effectively replace the core electrons and the true potential (Z/r) with a smoother, effective potential, which results in atomic, valence electron wave functions with reduced oscillations while preserving key features of the all-electron, atomic, valence electron wave functions, such as their eigenvalues and values outside the cutoff radius (which separates the core and valence regions) [57].

The pseudopotential (PP) approach originated with the orthogonalized plane wave (OPW) method [69,70], in which the wavefunctions of the valence band are expanded using a basis consisting of plane waves that are orthogonalized to the lower lying core states, φ_c, as represented below.

$$\phi_{\text{OPW}}(\mathbf{K}+\mathbf{G}) - \sum_{\alpha,c} \langle \varphi_c | \phi_{\text{PW}}(\mathbf{K}+\mathbf{G}) \rangle \varphi_{\alpha,c} \tag{2.4}$$

Here, ϕ_{PW} is a plane wave and ϕ_{OPW} is the corresponding OPW, and the sum if over core states and atoms. They effectively eliminate, from the very start, the true electron-nuclear potential and the inner core electrons, that is, those electronic states that are tightly bonded to the nucleus, do not participate in the formation of chemical bonds, and remain approximately unchanged in atoms, molecules and solids [69–71]. Also, this conceptual simplification amounts to a very practical efficient computational scheme, especially when a plane-wave basis set is adopted to expand the electronic wavefunction. In the 80's, this method, in connection with a density-functional description of the electron-electron interaction, evolved into a reliable prescription for the first principle computation of electronic, structural, and dynamical properties of molecules and solids. The fundamental idea of pseudopotential is the replacement of one problem with another. The primary applications in electronic structure is to replace a strong Coulomb potential of the nucleus and the effects of the tightly bound core levels by an effective ionic potential acting on the valence electrons. The core states remain almost unchanged (frozen approximation). Plane wave pseudopotentials are usually employed because simplify the interaction between nuclei and electrons by reducing the number of electron states considered.

The pseudo-wavefunctions (and potential) are constructed to be equal to the actual valence wavefunction (and potential) outside the core wavefunction radius r_c. Inside r_c, the pseudo-wavefunction differ from the true wavefuncion, but the norm is constructed to be the same,

$$\int_0^{e_c} r^2\, \psi^{[*ps]}(\vec{r})dr = \int_0^{e_c} dr\, r^2\ \psi^*(\vec{r})\psi(\vec{r}). \tag{2.5}$$

The integrated charge density inside r_c for each wave function agrees for r_c for each wave-function. The wave function and eigenvalue depend on the angular momentum l and the pseudo-wave function called semi-local should be l. Other conditions can be imposed to enchance the smoothness of the potential, i.e. to reduce the number of high energy Fourier components required for plane wave calculations. This is crucial for PWs because this is the single factor that determines the energy cutoff, and thus the cost of the calculation. Typical cutoff radii are between two and three times the core radius, and are located in the region around the maximum of the valence wave function.

Having a brief view of a the quantum mechanics parts on the DFT, which has been extremely successful during the past decade, leading with the calculation to simulate the behavior and properties of the materials, the next chapter we will address the solid state physics to help us understand how to interpreted thus results and are what are the properties of the object of study in this work.

We choose to use norm-conserving pseudopotential (NCPP), this is because the main strengths of norm-conserving (NC)is their superior transferability. They preserve scattering properties across various chemical environments, allowing for reliable application to different crystal structures without reparameterization. This characteristic is particularly useful when studying materials under diverse conditions.

These pseudopotentials also enable accurate calculations of optical properties, such as the dielectric function and absorption spectra. The preservation of the wavefunction norm ensures the correct description of wavefunction shapes, which is vital for predicting optical responses and excitonic effects.

Although norm-conserving pseudopotentials may require higher energy cutoffs than ultra-soft pseudopotentials, they provide a balance between accuracy and computational efficiency. This allows for systematic convergence of results, which is especially important in plane-wave basis calculations.

Bisedes that their ability to accurately describe physical wavefunctions makes norm-conserving pseudopotentials suitable for computing forces, stress tensors, and phonon spectra. This is crucial for studying lattice dynamics and other structural properties in materials science.

2.3.1 DFT: GGA Approximations

We use the QE code package with a GGA pseudopotential and a plane-wave basis set to perform the first-principles calculations of the structural, dielectric, and vibrational properties of

ZnO. DFT generally uses a wavefunction to compute some parts of the formation energy, total energy and fermi energy. The total electronic density and the normalized wavefunction are interrelated because the former is the absolute value of the square of the normalized wavefunction times the number of electrons [72].

For the Generalized Gradient Approximation (GGA), the exchange-correlation energy depends on a local gradient of the charge density. It emerged as an attempt to describe better some systems where the LDA approximation is not sufficient [7, 47, 70].

$$E_{xc}^{GGA} = \int f(\rho(\mathbf{r}, \nabla\rho(\mathbf{r}))d\mathbf{r} \tag{2.6}$$

This is desirable because the electron density of a real system is not homogeneous and varies spatially, unlike what is done in LDA. In this way, a more realistic description of the systems is obtained.

Compared to LDA, GGAs tend to improve total energies [47, 70]. However, unlike LDA in which the exchange and correlation energy ε_{xc}^{hom} is uniquely defined, there is no function $E_{xc}^{GGA}[\rho]$ that defines GGA. What exists, however, are numerous proposals for parameterizations, of which one of the most popular, which is used in the present thesis, is the functional parameterized by Perdew, Burke and Ernzerhof (PBE). So, despite its strengths, DFT has limitations stemming from its approximations, particularly in the exchange-correlation functional. Calculations using DFT potentials are the most successful and widespread in the last three decades, in several areas of materials studies, most of these calculations have resulted in significant underestimations of the band gaps of semiconductors and of insulators. The determination of the total energy of the system depends on the exchange-correlation energy term (Equation (2.6)).

We seek convergence by applying different cutoff values for the wave function, k-points, and charge density energy cutoff, until the results no longer oscillate between large values. After obtaining the energy cutoff for wavefunctions, k-point grid, and Gaussian broadening, the parameters need to be converged. Then, a relaxation calculation is required to obtain the lattice parameters and cell positions. Converging the parameters guarantees the reliability of electronic structure calculations, while relaxation calculations provide valuable information about the structural stability and geometry of the material. After to convergence parameters, there are other essential calculation operations in material simulations. One of them is the Self-Consistent Field (SCF)calculation, which aims to find a self-consistent solution to the Kohn-Sham equations in DFT [73]. This is crucial for obtaining an accurate description of the electronic structure of the system. The Non-Self-Consistent Field (NSCF) is another important calculation, used to compute electronic properties without self-consistently iterating the wavefunction.

We obtain the band structure by solving the Kohn-Sham equations. In the density of states (DOS) calculations, the energy levels of electrons in the material are typically represented by a

density function, which describes the number of electronic states per unit energy interval.

2.4 IMPLEMENTATION

This section covers the implementation of Density Functional Theory (DFT) using Quantum ESPRESSO, with a focus on the Hexagonal Close-Packed (HCP) structure and the use of Special Quasirandom Structures for supercells, providing practical insights into the application of DFT for simulating complex materials.

2.4.1 Quantum Espresso

Quantum ESPRESSO is a comprehensive set of software tools designed for electronic-structure calculations and materials modeling, based on density functional theory, plane waves, and pseudopotentials (including norm-conserving, ultrasoft, and projector-augmented wave types). The name "Quantum ESPRESSO" stands for "opEn Source Package for Research in Electronic Structure, Simulation, and Optimization." It is freely available to researchers globally under the GNU General Public License. Quantum ESPRESSO is built on advanced electronic-structure codes developed and tested by some of the pioneers in the field, and has been used for over two decades by leading materials modeling groups. The software prioritizes innovation, efficiency, and user-friendliness, with particular emphasis on support for massively parallel architectures. It is continually evolving as an open-source project, inviting contributions from researchers who wish to share their own code or integrate new ideas into the existing framework. [74]

2.4.2 Hexagonal Closed-packed Structure (HCP)

There are an infinite number of ways of arranging identical spheres in a regular array that maximizes the packing fraction. One is the FCC structure, and the other is the HCP structure, as shown in Figures 2.1c and 2.1d. The number of nearest-neighbor atoms is 12 for both HPC and FCC structures. If the binding energy depended only on the number of nearest-neighbor bonds per atom, there would be no difference in energy between them. The atom positions in the HCP structure do not constitute a space lattice. The space lattice is a simple hexagonal lattice with a basis of two identical atoms associated with each lattice point, where a is in a basal plane and c is the magnitude of the axis $\mathbf{a_3}$.

2.4.3 Special Quasirandom Structures for Supercells

Special Quasirandom Structures (SQS) are a computational technique used to efficiently and realistically model disordered materials, such as metallic alloys. Instead of simulating fully random systems, which would require very large supercells and computationally expensive calculations, SQS are periodic structures designed to reproduce the statistical properties of a disordered material, such as short-range atomic correlations. This approach is widely used in methods like Density Functional Theory (DFT) to study electronic, thermodynamic, and mechanical properties of alloys and other complex materials.

Here, we employ the Special Quasirandom Structures (SQS) method to study the structural properties of doped ZnO. The supercell method is the ubiquitous approach for studying solid-state systems with periodic boundary conditions [75]. With only a system of four atoms, using DFT calculation, it is possible to obtain important information about the lattice parameter, atomic distance between those atoms, stress, and boundary conditions, making it possible to calculate their band structure, density of states (DOS), and optical response, such as the complex dielectric function $(\tilde{\varepsilon}(\lambda))$. However, in the macroscopic world, matter consists of more than just a few atoms—often, even billions. Therefore, creating a supercell is one of the tools used in simulations to provide a more accurate description of physical systems, allowing for the evaluation of phenomena like doping, for example. When expanding the primitive cell to 72 atoms, the doping of one foreign atom corresponds to approximately 1.39%, mimicking real configurations. But how can one be sure if the replacement of one atom with another will generate the most favorable atomic configuration? To the best of our knowledge, previous works have either handpicked the position of the new atom [76,77] in a supercell or randomly replaced them [78]. In this way, they may not have reproduced the most energy-favorable crystal structure. To overcome this challenge, we employ the SQS to provide real physical doped systems.

SQS are specially designed small-unit-cell periodic structures that closely mimic the most relevant nearest neighbor pair and multi-site correlation functions of random substitutional alloys. For example, in a random diamond $A_{1-x}B_x$ alloy, an A or B atom can be surrounded by various A_mB_{4m} coordination shells with m ranging from 0 to 4. Such distribution of local environments will mimic the influence of a random distribution, including dopant-defect interactions [79].

This approach predicts self-averaging quantities of alloys using finite-size supercells, meaning the relative variance of the physical quantity Q vanishes [80, 81] by enhancing the number of possible configurations [81, 82],

$$\frac{\langle Q^2\rangle - \langle Q\rangle^2}{\langle Q\rangle^2} \longrightarrow 0, \tag{2.7}$$

Using the nominator from equation (2.7) for a binary $A_{1-x}B_x$ alloy, one can formulate the

SQS algorithm to minimise the energy of the system. This implies that the material properties converge to the expected mean values of a sufficiently large sample, representing randomness well without the need for an infinite sample. In practice, Q is minimized with respect to the system's atomic configuration. The SQS approach has become a key technique for modeling tensorial properties and determining local properties of alloys, such as vacancy formation energy, due to its relatively low computational cost compared to calculating self-averaging thermodynamic quantities. This is because it does not focus on generating structures with accurate point symmetry.

In this work, we built a seventy-two-atom ZnO supercell using the positions and lattice parameters of the four initial atom cells, which means the supercell was made by replicating the conventional unit cell, and the structure after it was built was relaxed on QE. We chose to expand it to a 2x2x2, 3x3x2, and 3x3x3 supercell, and also used the SQS method for doping with Ag. We doped by replacing one Zn atom and continued replacing one atom at a time until we had 8 doped atoms in different random configurations for a 72-atom system. The following doping concentrations were obtained: 1.39%, 2.78%, 4.17%, 5.56%, 6.94, 8.33%, 9.97%, and 11.11%. All SQs' expansion method used the same concentrations.

2.4.3.1 Super Cell Generation

The process begins by defining the primitive unit cell of ZnO in the wurtzite structure. The bulk function from the ASE (Atomic Simulation Environment) library is used to generate the structure with a lattice parameter 'a' equal to 3.25 Å.

The next step involves defining the cluster space, which is essential for capturing atomic interactions in the structure. The cutoffs for pairs, triplets, and quadruplets were set to 7.0 Å, 5.0 Å, and 4.0 Å, respectively. Additionally, it was specified that Zn sites can be occupied by either Zn or Ag, while O sites remain unchanged.

For the desired doping of approximately 4.17% Ag, it was planned to replace 3 Zn atoms with Ag in a supercell containing 72 atoms (36 ZnO pairs). Thus, the target concentrations were defined as follows: The `generate_sqs` function was used to generate the SQS structure that meets the target concentrations and specified symmetry conditions. The parameters included the maximum supercell size (`max_size=18`), initial and final temperatures for the simulated Monte Carlo algorithm (`T_start=10.0` and `T_stop=0.001`), number of steps, and optimality weight.

2.5 QUANTUM MECHANICS

In recent years, density functional theory (DFT) has been the dominant method for quantum mechanical simulations of periodic systems. In recent years, it has also been adopted by quantum physicists and is now widely used for simulating energy surfaces in molecules. In this chapter, the main concepts of Density Functional Theory (DFT) will be discussed, including its theoretical foundation, the Hartree-Fock approximation, the Hohenberg-Kohn theorems, the Kohn-Sham equation, optimization methods, and the Perdew-Burke-Erzenhof (PBE) functional, providing an essential understanding of how DFT is applied in the simulation of periodic and molecular systems.

2.5.1 Introduction

The physicists Schrödinger and Heisenberg put forward the Schrödinger equation and the uncertainty principle respectively, which marked the birth of quantum mechanics in 1926 and 1927. After that, the physics of the world could have access to a completely different knowledge from classical mechanics. The H_2 molecule was the first atomic structure studied using the applied approach of quantum mechanics by the physicists Heithler and London in 1927, and it successfully explained the bonding mechanism in a homo nuclear molecule [83, 84]. Their success marked the interdisciplinary science of quantum mechanics and chemistry: the birth of quantum chemistry.

The Hartree equation [85] was proposed in 1928, which assumed that the charge distributions of each electron were the solution of the Schrödinger equation for an electron in a potential $V(r)$, derived from the field created by other electrons. Hartree's students, Fock and Slater, proposed a self-consistent field iterative equation considering the Pauli principle, called the Hartree-Fock equation, which further improved the Hartree equation in 1930 [83, 86–88]. To solve the Hartree-Fock equation, in 1951, Roothaan further proposed that molecular orbitals could be expressed as the linear combination of atomic orbitals that comprise the molecule and developed the famous Roothaan-Hartree-Fock (RHF) equation [83, 89]. This equation, along with the method based on the further development of this equation, is the fundamental method of modern quantum chemistry.

Although quantum theory had been established as early as the 1930s, the Schrödinger equation is very complex when involving atoms with more than one electron due the repulsion potential between electrons, and it is still difficult to obtain the exact solution in a many-electron system. Even for the approximate solution by molecular orbital, that means describing the electron distribution in crystalline materials by combining atomic orbitals, considering interactions between atoms, the required computations are enormous. For example, for a small molecule

with 100 electrons, there are over 100 million double-electron integrals in the process of solving the RHF equation. This calculation is impossible for humans to complete. In the study of condensed matter physics, it is almost impossible to calculate the crystal and the surface from the classical molecular orbital due to the periodic structure of the crystal and the 10^{23} order magnitude of the nuclei and electrons per cubic centimeter [83]. Thus, the theoretical calculation of solid physics has been developing slowly. It was not until the 1990s that the maturity of density functional theory (DFT) and the development of computer hardware provided an effective theoretical tool for calculating the electronic properties of solids and their surfaces. DFT is a quantum-mechanical method used in physics to calculate the electronic structure of atoms, crystalline materialsand solids [90]. It has been widely used in computational solid-state physics since the 1970s. However, only in the 1990s did improvements in its accuracy make it suitable for quantum-physics applications, leading to a significant increase in its use. Distinguished from many methods based on molecular orbital theory, which construct wave functions of multi-electron systems (e.g., Hartree Fock methods), this method is based on the electron density function and solves the single-electron many-body Schrödinger equation by Kohn-Sham self-consistent field (KS-SCF) iteration to obtain the electron density distribution. This operation reduces the number of free variables and the degree of systematic oscillation, improving the rate of convergence.

2.5.2 The theory behind the DFT

Wave function, in quantum mechanics, is a quantity that mathematically describes the wave characteristics of a particle, that's means it is a mathematical tool that encodes the quantum state of a system, describing its wave-like properties and enabling predictions about the probabilities of measurement outcomes. It is central to the formalism of quantum mechanics. The value of the wave function of a particle at a given point of space and time is related to the probability of the particlebeing there at the time. By analogy with waves, such as those of sound, a wave function designated by the Greek letter psi, Ψ, may be thought of as an expression for the amplitude of the particle-wave (or de Broglie wave), although for such waves amplitude has no physical significance. However, the square of the wave function, Ψ^2 does have physical significance: the probability of finding the particle described by a specific wave function Ψ at a given point and time is proportional to the value of Ψ^2 [91]. Mathematically, the wavefunction must satisfy the normalization conditions

$$\int_{-\infty}^{\infty} |\Psi(\mathbf{r})|^2 \, d\mathbf{r} = 1. \tag{2.8}$$

The Hamiltonian is a fundamental concept in quantum mechanics and plays a vital role in

computational simulation. It is an operator that represents the total energy of a quantum system, including both kinetic and potential energy. The Hamiltonian provides a mathematical framework for describing the dynamics and evolution of quantum states. In particular, the dynamics and time evolution of quantum states are described by the time-dependent Schrödinger equation:

$$i\hbar\frac{\partial}{\partial t}\Psi(\mathbf{r},t) = \hat{H}\Psi(\mathbf{r},t),$$

where $\hat{H}$ is the Hamiltonian operator. This equation governs how the wave function $\Psi(\mathbf{r},t)$ evolves with time. For systems where the Hamiltonian does not explicitly depend on time, the evolution of the quantum state can be expressed as:

$$\Psi(\mathbf{r},t) = e^{-iEt/\hbar}\Psi(\mathbf{r}),$$

where E is the energy eigenvalue corresponding to a stationary state. Mathematically, the Hamiltonian $\hat{H}$ is a Hermitian operator that acts on the state space of a quantum system.

The eigenvalues of the Hamiltonian correspond to the possible energy levels of the system, and its eigenvectors represent the corresponding stationary states. For a single particle, the time-independent Hamiltonian operator is given by [92]

$$\hat{H} = -\frac{\hbar^2}{2m}\nabla^2 + V(\mathbf{r}), \tag{2.9}$$

where $\hat{H}$ is the Hamiltonian operator, $\hbar$ is the reduced Planck constant, m is the mass of the particle, ∇^2 is the Laplacian operator, and $V(\mathbf{r})$ is the potential energy depending on the position $\mathbf{r}$. For a system of multiple particles, the Hamiltonian operator is the sum of the individual Hamiltonians for each particle.

In 1913, Bohr suggested that instead of buzzing randomly around the nucleus, electrons inhabit orbits situated at a fixed distance away from the nucleus. In this picture, each orbit is associated with a particular energy, and the electron can change orbit by emitting or absorbing energy in discrete chunks (called quanta). In this way, Bohr was able to explain the spectrum of light emitted (or absorbed) by hydrogen, the simplest of all atoms. However, it showed many deficiencies for other atoms, i.e., almost all atoms of interest other than hydrogen. The Schrödinger equation overcame the limitations of the Bohr approach: the quantum numbers naturally emerge from it due to the confinement, as in the case of a particle in a potential well, where there is no need to consider spin. The spin quantum number m_s requires a relativistic form of the Schrödinger equation, the Dirac equation, and electron 'spin' is not actually due to the particle spinning like a top. It is important to highlight that the Schrödinger equation

can be solved in an exact analytical way only for one-electron systems like the hydrogen atom, the helium mono-cation, and the hydrogen molecule ion. Still, the mathematical approach is complicated in the study of complex crystalline materials [93].

To solve the Schrödinger equation for hydrogen-like atoms, we need to transform it from Cartesian (x, y, z) to polar coordinates (r, θ, ϕ), since these are more naturally in accordance with the spherical symmetry of the system, since the Coulomb potential between the nucleus and the electrons depends only on the distance between them, not on the directions. With this basis, it is possible to separate the equation into three independent equations, one for each coordinate: a radial equation $F(r)$, an angular equation $\Theta(\theta)$, and an azimuthal equation $\Phi(\phi)$. The solutions to these equations lead to the quantum numbers: The solution of the radial equation $F(r)$ determines the principal quantum number n, the solution of the angular equation $\Theta(\theta)$ determines the azimuthal (or orbital) quantum number l and the solution of the azimuthal equation $\Phi(\phi)$ determines the magnetic quantum number m.

For each specific set of quantum numbers (n', l', m'), the total wavefunction is obtained by combining these solutions:

$$\Psi(r, \theta, \phi; n', l', m') = F(r)\Theta(\theta)\Phi(\phi). \tag{2.10}$$

The wavefunction $\Psi(r, \theta, \phi)$ depends explicitly on the spatial coordinates r, θ, and ϕ, while it is parametrized by the quantum numbers n, l, and m. For each particular set $(n = n', l = l', m = m')$, a specific function describes the quantum state in terms of the spatial coordinates r, θ, and ϕ (or equivalently x, y, z). This Ψ function is an orbital or, in terms used by Milliken, "quasi-orbit", and shows how its representation changes with respect to spatial coordinates. Plots of the variation of Ψ^2 with spatial coordinates indicate variations of the electron density in space due to an electron with quantum numbers n', l', and m', recall the Born interpretation of the wavefunction. An orbital can be viewed as a spatial region where an electron exists, characterized by a specific set of quantum numbers, or as a mathematical function that describes the energy and shape of the electron's spatial domain. For an atom or molecule with more than one electron, the assignment of electrons to orbitals is an approximation since orbitals follow from the solution of the Schrödinger equation for a hydrogen atom [92, 93].

The Schrödinger equation is typically solved for stationary states, where the time dependence is separated from the spatial dependence of the wave functions. This leads to time-independent solutions, which are eigenfunctions of the Hamiltonian operator. The Schrödinger equation we've been discussing is actually the time-independent (and nonrelativistic) Schrödinger equation. In this equation, the variables are spatial coordinates, or spatial and spin coordinates when electron and spin are considered. This time-independent equation is the most commonly used in numerical calculations. However, the more general time-dependent Schrödinger equation, which we will not delve into, is crucial for certain applications. For instance, it is essen-

tial in some methods of studying the interaction between crystalline materials and light, since light (radiation) consists of time-varying electric and magnetic fields. The time-independent Schrödinger equation, for a non-relativistic particle, is given by

$$\hat{H}\Psi = E\Psi, \tag{2.11}$$

where H is the the Hamiltonian operator, $\hat{\Psi}$ is the wave function, and E represents the energy of the system. This equation is a partial differential equation that determines the allowed wave functions and corresponding energy eigenvalues of a quantum system. By solving the Schrödinger equation, valuable information about the energy levels, wave functions, and properties of the systems such as energy levels, transitions probabilities and expectation values of observable are obtained.

A many-electron system refers to a quantum mechanical system that involve more than one electron. while the behavior of a single electron can be accurately describe by a single wavefunction, the inclusion of multiple interacting electrons introduces significant complexity. The Hamiltonian operator

$$\begin{aligned}\hat{H} = &-\sum_{i=1}^{N}\frac{\hbar^2}{2m_e}\nabla_i^2 - \sum_{I=1}^{M}\frac{\hbar^2}{2M_I}\nabla_I^2 - \sum_{i=1}^{N}\sum_{I=1}^{M}\frac{Z_I e^2}{|\mathbf{r}_i - \mathbf{R}_I|} \\ &+ \sum_{i<j}\frac{e^2}{|\mathbf{r}_i - \mathbf{r}_j|} + \sum_{I<J}\frac{Z_I Z_J e^2}{|\mathbf{R}_I - \mathbf{R}_J|},\end{aligned} \tag{2.12}$$

here $\hbar$ is the reduced Planck's constant, m_e is the mass of the electron, M_I is the mass of the nucleus I, Z_I is the charge of the nucleus I, e is the charge of the electron, ∇_i^2 is the Laplacian operator acting on the position of the electron i, and ∇_I^2 is the Laplacian operator acting on the position of the nucleus I. The many-electron Schrödinger equation cannot be solved exactly (or at least has not been solved yet) even for a simple two-electron system such as the helium atom or hydrogen molecule. Approximations need to be introduced to provide practical solutions [94, 95].

One way to simplify the Schrödinger equation for larger systems is to assume that the nuclei are considered as motionless since their movement is much slower than the electrons' ones. This is called the Born-Oppenheimer approximation, and leads to an "electronic" Schrödinger equation [68, 95]

$$\Psi(\mathbf{R}, \mathbf{r}) = \psi_e(\mathbf{r}; \mathbf{R})\chi(\mathbf{R}). \tag{2.13}$$

The $\psi_e(\mathbf{r}; \mathbf{R})$ is the electronic wavefunction that depends on the positions of the nuclei

where $\chi(\mathbf{R})$ is the nuclear wavefunction.

$$\hat{H}_e = -\sum_{i=1}^{N} \frac{\hbar^2}{2m_e} \nabla_i^2 - \sum_{i=1}^{N} \sum_{I=1}^{M} \frac{Z_I e^2}{|\mathbf{r}_i - \mathbf{R}_I|} + \sum_{i<j} \frac{e^2}{|\mathbf{r}_i - \mathbf{r}_j|} \tag{2.14}$$

The term in equation (5) describing the nuclear kinetic energy is missing in equation (7) (it is zero), and the nuclear-nuclear Coulomb term in equation (5) is a constant. The latter needs to be added to the electronic energy, E^{el}, to yield the total energy, E, of the system. Note that nuclear mass does not appear in the electronic Schrödinger equation.

2.5.3 The Hartree-Fock Approximation

The electronic Schrödinger equation is inherently complex for many-body systems and cannot be solved exactly, necessitating further approximations. A common simplification is to assume that electrons move independently of one another. In practical terms, each electron is described by a molecular orbital, which is calculated assuming that the electron experiences an average field created by all other electrons. A single determinant, known as a Slater determinant, is employed to represent the total wavefunction. This formulation ensures that the wavefunction is antisymmetric with respect to the exchange of electron coordinates [56,68,96],

$$\psi(\mathbf{r}_1, \mathbf{r}_2, \ldots, \mathbf{r}_N) = \frac{1}{\sqrt{N!}} \begin{vmatrix} \phi_1(\mathbf{r}_1) & \phi_1(\mathbf{r}_2) & \cdots & \phi_1(\mathbf{r}_N) \\ \phi_2(\mathbf{r}_1) & \phi_2(\mathbf{r}_2) & \cdots & \phi_2(\mathbf{r}_N) \\ \vdots & \vdots & \ddots & \vdots \\ \phi_N(\mathbf{r}_1) & \phi_N(\mathbf{r}_2) & \cdots & \phi_N(\mathbf{r}_N). \end{vmatrix} \tag{2.15}$$

$\phi_i(\mathbf{r}_j)$ represents the single-particle wavefunction (molecular orbital) associated with of the i-th electron evaluated at the position of the j-th electron. Solving the Hartree–Fock from the perspective of computational software means finding a proper coefficient matrix (C) that minimize the total energy with respect to all degrees of freedom in the wavefunction with the restriction that it has the form equation (8) [97].

The lowest-energy molecular orbitals are obtained using the self-consistent field (SCF) approach. The Hartree-Fock (HF) method is a classic example of an SCF technique, as is Density Functional Theory (DFT). These methods iteratively refine the molecular orbitals by solving the equations self-consistently until convergence is achieved, effectively minimizing the total energy of the system.

$$f(i)\phi(x_i) = \epsilon\phi(x_i) \tag{2.16}$$

Here, the Fock operator $f(i)$ can be written as

$$f(i) = -\frac{1}{2}\nabla_i^2 + \upsilon_{\text{eff}}(i) \tag{2.17}$$

The coordinates $\mathbf{x}_i$ represent both the spin and spatial coordinates of the i electron, ϕ denotes the spin orbitals, and υ_{eff} is the effective potential experienced by the i electron, which depends on the spin orbitals of the other electrons. The nature of the effective potential υ^{eff} depends on the Self-Consistent Field (SCF) methodology used.

Hartree-Fock models assume that the motions of individual electrons are independent of each other. To achieve this, they substitute the "instantaneous interactions" between individual electrons with interactions between a particular electron and the average field created by all the other electrons. This approximation causes electrons to interfere with each other more than they actually do, leading to an overestimation of the electron-electron repulsion energy and, consequently, a higher total energy. Electron correlation, which refers to the coupling or correlation of electron motions, reduces the overestimation of electron-electron repulsion and lowers the total energy. The correlation energy is defined as the difference between the Hartree-Fock energy and the experimentally determined energy [68].

The electron density concept provides a convenient way to describe and analyze the distribution of electrons within a many-electron system. The number operator $\hat{n}(\mathbf{r})$ describes the presence of particles (or electrons) at a specific position in space. For a system of localized particles, the number operator is given by:

$$\hat{n}(\mathbf{r}) = \sum_i \delta(\mathbf{r} - \mathbf{r}_i), \tag{2.18}$$

where $\delta(\mathbf{r}-\mathbf{r}_i)$ is the Dirac delta function, which is zero everywhere except at $\mathbf{r} = \mathbf{r}_i$, where it has an infinite peak.

The electron density $\rho(\mathbf{r})$ describes the probability of finding an electron at a position $\mathbf{r}$ in space. Mathematically, it is given by the expectation value of the number operator $\hat{n}(\mathbf{r})$:

$$\rho(\mathbf{r}) = \langle\Psi|\hat{n}(\mathbf{r})|\Psi\rangle. \tag{2.19}$$

Substituting the expression for $\hat{n}(\mathbf{r})$, we obtain:

$$\rho(\mathbf{r}) = \langle\Psi| \sum_i \delta(\mathbf{r} - \mathbf{r}_i)|\Psi\rangle. \tag{2.20}$$

In systems with continuous wavefunctions, the electron density $\rho(\mathbf{r})$ can be written as the sum of contributions from the wavefunctions of all electrons:

$$\rho(\mathbf{r}) = \sum_i |\Psi_i(\mathbf{r})|^2. \tag{2.21}$$

DFT is based not on the wavefunction, but rather on the electron probability density function or the electron density function, commonly called simply the electron density or charge density designated by $\rho(x, y, z)$. This is a probability per unit volume: the probability of finding an electron in a volume element $dx\ dy\ dz$ centered on a point with coordinates x, y, and z is $\rho(x, y, z)\ dx\ dy\ dz$. The units of ρ are logically $volume^{-1}$, and since the units of $dx\ dy\ dz$ is volume, it is a pure number, a probability. However, if we regard the charge on the electron as our unit of charge, then ρ has units of electronic charge $volume^{-1}$ and $\rho(x, y, z)dx\ dy\ dz$ units of electronic charge.

The electron density function serves as the foundation for not only DFT but also a range of methods for examining atoms and molecules and crystalline materials [93, 98]. Unlike the wavefunction, the electron density can be directly measured, for example, by X-ray diffraction or electron diffraction [93, 99]. In addition of being an experimentally observable quantity and intuitively understandable, the electron density has another significant advantage. It is a function solely of position, involving just three variables (x, y, z), whereas the wavefunction of an n-electron molecule depends on $4n$ variables—three spatial coordinates and one spin coordinate for each electron. This means that regardless of the size of the molecule, the electron density remains a function of three variables, where the complexity of the wavefunction increases with the number of electrons [93, 98–100].

By studying the electron density, it is possible to uncover important information about the bonding and electronic interactions in materials. For example, the presence of an electron density between two atoms indicates the existence of a chemical bond, whereas regions of high electron density may signify the presence of lone pairs or charge localization; such insights are crucial for understanding the stability, reactivity and functionality of materials [96].

2.5.4 The Hohenberg-Kohn theorems

The first theorem of Hohenber-Kohn state that the external potential $V_{\text{ext}}(r)$ experienced by the electrons is a unique functional, except for a constant, of the ground-state electronic

density $\rho_0(r)$, and the second one is a universal functional of the energy $E(\rho)$ defined in terms of the density $\rho(r)$, valid for any $V_{\text{ext}}(r)$. For a particular $V_{\text{ext}}(r)$, the ground-state energy E_0 is minimized for the exact density $\rho(r)$.

According to these theorems, the expectation value of the Hamiltonian $\hat{H}$ can be expressed as

$$\langle \Psi | \hat{H} | \Psi \rangle = E(\rho(r)). \tag{2.22}$$

Since energy is a function of the density, which is also a function, it is called a functional (a function of functions). If the form of the energy functional is known, one can change the electron density until the energy function is minimized using the variational principle

$$\frac{\delta E(\rho(r))}{\delta \rho} = 0. \tag{2.23}$$

From equation (14), the electron density corresponding to the minimum energy E_0 is the ground state density $\rho_0(r)$. Thus, the ground-state energy is written as

$$E_0 = \langle \Psi | \hat{H} | \Psi \rangle = E(\rho_0(r)) \tag{2.24}$$

2.5.5 The Kohn-Sham Equation

In general, a functional is a kind of mapping on a vector space, usually of functions. The electron probability density ρ is a function $\rho(\mathbf{r})$ of a point in space located by the radius vector $\mathbf{r}$ measured from an origin (possibly an atomic nucleus), and the energy E of an electron distribution is a function of its probability density $E = f(\rho)$. Therefore, E is a functional of $\rho(\mathbf{r})$ denoted $E(\rho(\mathbf{r}))$. The first Hohenberg–Kohn theorem states that, for a nondegenerate ground state, there is a one-to-one mapping between ρ, $\mathbf{V}$, and ψ_0 [68, 101].

$$\rho(r) \longleftrightarrow V(r) \longleftrightarrow \psi_0, \tag{2.25}$$

where V is the potential energy, and ϕ_0 is the wave function at a given potential, that is, ψ_0 is a functional of V and of ρ

$$\psi_0 = \psi_0(V) = \psi_0(\rho). \tag{2.26}$$

In 1965, W. Kohn and L. J. Sham introduced the Kohn-Sham equation as a practical way to solve the many-body Shrodinger equation within DFT. Their equations transform the many-electron system into a set of non-interacting electrons moving in an effective potential. The Kohn-Sham equation can be derived by introducing an auxiliary system of noninteracting electrons with the same electron density as the ground-state density of the real system. The non-interacting Kohn-Sham system consists of a set of single-particle wavefunctions, known as Kohn-Sham orbitals, which obey the Kohn–Sham equations given by

$$\left[-\frac{\hbar^2}{2m_e}\nabla^2 + V_{\text{eff}}(\mathbf{r})\right]\psi_i(\mathbf{r}) = \epsilon_i\psi_i(\mathbf{r}), \tag{2.27}$$

where $\psi_i(\mathbf{r})$ are the Kohn–Sham orbitals for the i-th electron, ϵ_i are the Kohn–Sham eigenvalues, and $V_{\text{eff}}(\mathbf{r})$ is the effective potential. The effective potential is defined as the sum of the external potential V_{ext}, which accounts for the interaction with external fields or nuclei, and the exchange-correlation potential $V_{\text{xc}}(\mathbf{r})$, which captures the electron-electron interactions given by

$$V_{\text{eff}}(\mathbf{r}) = V_{\text{ext}}(\mathbf{r}) + V_{\text{xc}}(\mathbf{r}), \tag{2.28}$$

where $V_{\text{ext}}(\mathbf{r})$ is the external potential, $V_{\text{Hartree}}(\mathbf{r})$ is the Hartree potential, and $V_{\text{xc}}(\mathbf{r})$ is the exchange-correlation potential.

The exchange-correlation potential incorporates the effects of electron-electron interaction, for which an exact expression is unknown and requires approximations. Some of the common approximation schemes are the local density approximation (LDA) and the gradient approximation (GGA)

2.5.6 Optimization

The positions of the atoms in their unit cell influence the microscopic properties of the crystalline material. Therefore, it is fundamental to calculate the atomic positions and the lattice parameters corresponding to the minimum energy. This requires optimizing the atomic positions within the unit cell.

The total electronic energy of the system is obtained iteratively through the calculation of the Kohn-Sham potential V. The calculation of the electronic density is an implicit function of the nuclear positions $\vec{R}_I$

$$E_{\text{total}}(\mathbf{R}_1, \mathbf{R}_2, \ldots, \mathbf{R}_M). \tag{2.29}$$

Convergence is achieved when the electron density that minimizes the total energy of the system is found. This process is repeated until the positions of the ions reach convergence, that is, until the forces on the ions become sufficiently small, indicating that the system has reached a state of equilibrium. The Hellmann-Feynman method is based on calculating forces rather than the total energy. The essence of this method is based on evaluating the forces on the nuclei within a quantum-mechanical description of the system, which is done using the Hellmann-Feynman theorem [102]. Thus, starting from the Hamiltonian Equation (5) corresponding to the nucleus

$$\hat{H} = \sum_{i=1}^{N}\sum_{I=1}^{M}\frac{Z_I e^2}{|\mathbf{r}_i - \mathbf{R}_I|} + \frac{1}{2}\sum_{I,J=1,I\neq J}^{M}\frac{Z_I Z_J e^2}{|\mathbf{R}_I - \mathbf{R}_J|},$$

the nuclear force I in R_{I} can be calculated as

$$F_1 = \frac{\delta E_{\text{total}}}{\delta \mathbf{R}_1} = -\langle\psi\left|\frac{\delta \hat{H}}{\delta \mathbf{R}_I}\right|\psi\rangle. \tag{2.30}$$

This theorem proves to be very useful, as it provides an expression for the force on the nucleus based on the electron density ρ.

2.5.7 Perdew-Burke-Erzenhof (PBE)

The authors Perdew, Burke, and Ernzerhof [1996] presented a simplified construction for the exchange-correlation functional in the GGA approximation, known as GGA-PBE. The exchange term is represented by [70]

$$E_x[\rho(r)] = \int \rho(r)\varepsilon_x^{LDA}\rho(r)F_x^{PBE}(s)dr, \tag{2.31}$$

where the term $\varepsilon_x^{LDA}\rho(r)$ is the exchange energy per particle. The enhancement factor, $F_x(s)$, is given by

$$F_x^{PBE}(s) = 1 + k - \frac{k}{1 + \frac{\mu^2}{k}} \tag{2.32}$$

which, when multiplied by the exchange energy term, $\varepsilon_x^{LDA}\rho(r)$, describes the contribution of the exchange energy in a non-uniform system with respect to position. The term $F_x(s)$ depends

on the gradient density s, given by

$$s(r) = \frac{\nabla\rho(r)}{2K_F\rho(r)} \tag{2.33}$$

In equation (21), the parametrization is given by: μ=0.21951 and k= 0.804. Meanwhile, in equation (22), $K_F(r) = [3\pi^2\rho(r)]^{\frac{1}{3}}$ is the Fermi wavevector. The exchange-correlation potential is also an important quantity in judging the quality of a functional [44, 103], by the equation of exchange-correlation

$$\varepsilon_{xc}(\rho(r)) = \varepsilon_x(\rho(r)) + \varepsilon_c(\rho(r)) \tag{2.34}$$

where ε_x is the exchange terms and ε_c is the correlation one. Remember that the exchange term can be calculated analytically, while the correlation term cannot be determined exactly. However, using quantum Monte Carlo methods [104], one can calculate with great numerical precision for a homogeneous interacting electron gas. So, using equation (23), the functional is written in the PBE proposal as [70]

$$E_{\text{xc}}^{\text{PBE}}[\rho(r)] = \int \left[\varepsilon_c^{\text{hom}}(R_s,\zeta) + H_c^{\text{PBE}}(r_s,\zeta,t)\right]\, dr. \tag{2.35}$$

Here, r_s is defined as the Seitz radius, given by $r_s = (\frac{3}{4\pi\rho})^{\frac{1}{3}}$, the relative spin polarization is $\zeta = \frac{\rho\uparrow(r)-\rho\downarrow(r)}{\rho(r)}$, and the density gradient is $t = \frac{\nabla\rho}{2gk_s\rho}$ with $g = [(1+\zeta)^{\frac{2}{3}} + (1-\zeta)^{\frac{2}{3}}]/2$ representing the spin scaling factor.

3 RESULTS AND DISCUSSION

3.1 PURE ZnO

In the context of DFT, the optimization of atomic structure involves finding the arrangement of atoms that minimizes the total energy of the system. We optimize them to identify the most favorable configuration of atom positions and lattices. The lattice parameter, which defines the unit cell dimension of a crystal, is optimized using QE. By varying the lattice parameter, one can observe the effects of lattice distortion and investigate the stability of different crystal structures. Additionally, QE enables the calculation of atomic forces and stresses. While atomic forces provide information about the interaction between atoms and reveal the balance of forces within the system, stresses provide information about the mechanical properties of materials, such as their response to external forces or deformations. This knowledge is used to design new materials with specific properties, investigate phase transitions, and predict material behavior under different conditions [74].

We start our analysis with a four-atom ZnO structure (see Figure 3.1) in a hexagonal WZ configuration $P6_3/m$. The unit cell of ZnO in the WZ structure contains two Zn cations and two O anions, as shown in Figure 3.1 (a). Figure (3.1) (b) shows the convergence for the K-points grid, resulting in a 6x6x3 configuration. We choose a norm-conserving PP and search for the convergence parameters. Figure 3.1 (c) and (d) show the wavefunction cutoff energy (ecutwfc) in Rydberg and the charge density cutoff (euctrho) versus the total energy of the system calculated by SCF. The convergence of the wave function and charge density is 70 Ry and 300 Ry, respectively. The ZnO lattice parameters and positions of the atoms after relaxation calculation are presented in Table (3.1). They are in excellent agreement with other works and experimental values [40, 42, 105].

The values of a (3.23-3.25 Å) and c (1.60-1.97 Å) from this work align closely with the experimental values (3.25 Åand 1.97 Å, respectively) [42, 106, 107], indicating good agreement. The c/a ratio, ranging from 1.60 to 1.97 in the reference data and this work, also matches the experimental value of 1.97. However, the band gap energy from this work (0.71 eV) significantly deviates from the experimental value (3.4 eV), suggesting a potential underestimation, which is already expected in the DFT method [108].

Table 3.1: Comparison of ZnO structural parameters

	a (Å)	c/a	Zn-O (Å)	Band gap
Reference [105, 109, 110](Å)	3.31	1.61	2.02	0.75 (eV)
This work	3.23	1.60	1.97	0.71 (eV)
Experimental values [42, 106, 107]	3.25	1.60	1.97	3.4 (eV)

Figure 3.1: Structural and parameter optimization for pure ZnO

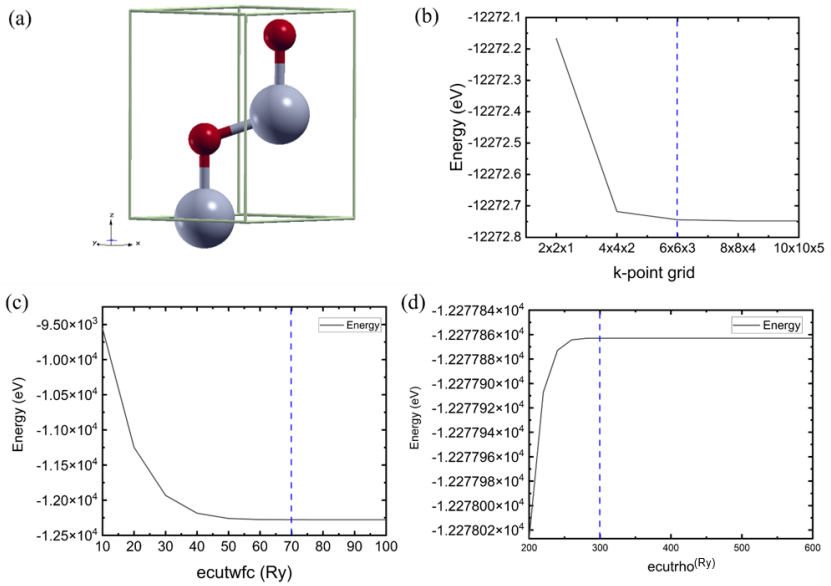

Source: Elaborated by the author (2025).
Note: (a) Schematic representation of the ZnO wurtzite structure after optimization; zinc (Zn) atoms in gray and oxygen (O) in red. (b) Convergence of total energy relative to the k-points grid. (c) Optimization of the wavefunction energy cutoff (E_{cut}). (d) Optimization of the charge density energy cutoff (E_{rho}).

Next, we perform band structure and DOS calculations using PBE-GGA potentials. The reciprocal space is sampled based on the convergence results grid in the ZnO unit cell calculations with four atoms (Figure 3.2 (a)). We expand the cell twice in every direction, starting with a 2×2×2 supercell (32 atoms, Figure 3.2 (b)), followed by a 3×3×2 supercell (72 atoms, Figure 3.2 (c)), and finally a 3×3×3 supercell with 108 atoms (Figure 3.2 (d)). We calculate the band structure and DOS for each system, analyzing the contributions of Zn and O orbitals to the structure, E_F, and E_g (see Figure 3.2 and Table 3.2).

Figure 3.2 (e) shows the electronic properties of the four-atom cell along the high-symmetry points Γ-M-K-Γ-A-L-H-L-M-K-H in the Brillouin zone, which corresponds to the hexagonal path for ZnO. Here, we confirm that ZnO has a direct bandgap, with the valence band maximum and conduction band minimum located at the same high-symmetry point, the Γ point ($k = 0$). The calculated bandgap E_g using PBE-GGA is 0.71 eV, consistent with previous works [110–112]. After verifying the results for the primitive cell and validating them with experimental data, we generated supercells to study finite-size effects.

Figures 3.2 (f)–(h) present the band structures for the 32-, 72-, and 108-atom supercells. While a direct bandgap at the Γ point is preserved, we observe a shift in the Fermi energy (E_F) towards the valence band for the larger supercells, suggesting an apparent p-type semiconductor behavior. This behavior, although unexpected for undoped ZnO, can be explained by known artifacts in supercell calculations. Specifically, as the number of atoms increases, E_F shifts can occur due to band-filling effects, artificial periodic image interactions, Brillouin zone folding,

and subtle inconsistencies in the convergence of computational parameters. These effects do not indicate physical doping, but rather reflect numerical and finite-size influences on E_F and the DOS [113].

The results of the TDOS and PDOS calculations for 4 atoms of ZnO bulk as a function of energy, in electron volts (eV), using the PBE functional, are shown in Figure 3.2 (i). The zero energy level represents E_F (black vertical line). The occupied states are found in the negative energy range (VB), while the unoccupied states (CB) are in the positive energy range. By analyzing the PDOS, it is possible to identify the main contributions of the valence band and conduction band. The O_p is what predominates in the VB, while Zn_s is in the CB. The DOS changes with the increase in atoms (Figure 3.2 (j)-(l)), as the band structure becomes denser and the distribution of states in the valence and conduction bands also alters.

Figure 3.2: Structural and electronic properties of ZnO supercells of varying sizes

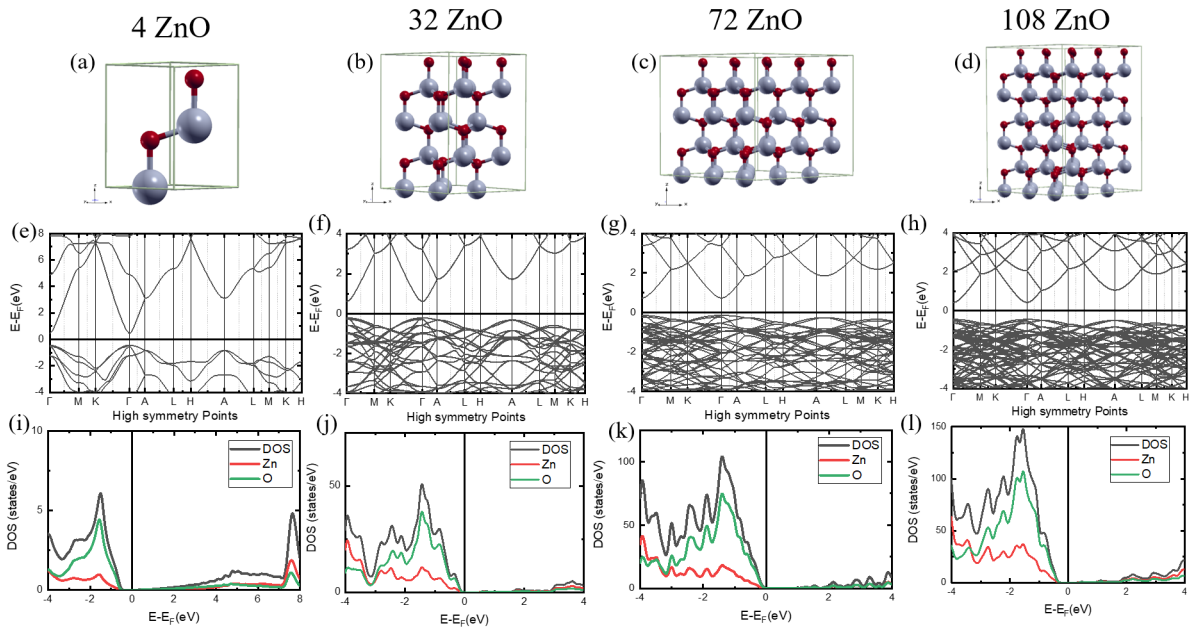

Source: Elaborated by the author (2025).
Note: Panels (a)-(d) display the atomic arrangements for 4, 32, 72, and 108 atoms, illustrating the WZ lattice evolution. (e)-(h) Corresponding band structures along high-symmetry paths, highlighting the direct bandgap at the Γ point. (i)-(l) Density of states (DOS) with energy levels relative to the Fermi energy ($E - E_F$).

Figure 3.3 presents the results of the evolution of the Fermi energy (E_F) and total energies as a function of the number of atoms in the ZnO supercells. Figure 3.3 (a) shows the variation of the Fermi energy in Ry about the number of atoms (4, 32, 72, and 108), revealing an initial decreasing trend followed by a progressive increase, suggesting changes in the electronic structure with increasing cell size. Figure 3.3 (b) displays the energies in Ry, including the final enthalpy (black line) and the total energy (red line), both of which decrease linearly with increasing number of atoms, indicating energetic stabilization. These data, combined TDOS and PDOS calculations for the 4-atom supercell (Figure 3.2 (i)), show that O_p orbitals dominate the valence band (VB), while the conduction band (CB) is predominantly composed of Zn_s

Table 3.2: Results for Pure ZnO

Parameter	4 atoms	32 atoms	72 atoms	108 atoms
$a()$	3.27	3.33	3.28	3.23
$c()$	5.27	5.13	5.24	5.22
c/a	1.61	1.54	1.59	1.61
E_F (eV)	9.48	9.15	9.60	10.21
Band Gap (eV)	0.81	0.84	0.82	0.86
New unit-cell Volume (Å^3)	331.32	395.99	884.57	1279.66
Final Enthalpy (Ry)	-902.41	-7218.92	-1624.33	-24364.79
Total Energy (Ry)	-902.41	-7219.34	-24365.01	-24365.01
Density (g/cm^3)	5.50	5.46	5.71	5.71
Lattice Parameter (Å)	3.27	3.33	3.23	3.23
Zn-O (Å)	1.97	1.97	1.97	1.97

orbitals, with E_F defined as the zero energy level. In the larger supercells (Figure 3.2 (j)-(l)), a densification of the band structure and a redistribution of states in the VB and CB are observed, reflecting the influence of the cell size on the electronics of the material. The character of the conduction band (CB) is predominantly derived from Zn $4s$ orbitals, while the valence band (VB) mainly consists of O $2p$ orbitals, and this electronic structure remains consistent across all supercell sizes.

Figure 3.3: Energy analysis as a function of the number of atoms for pure ZnO

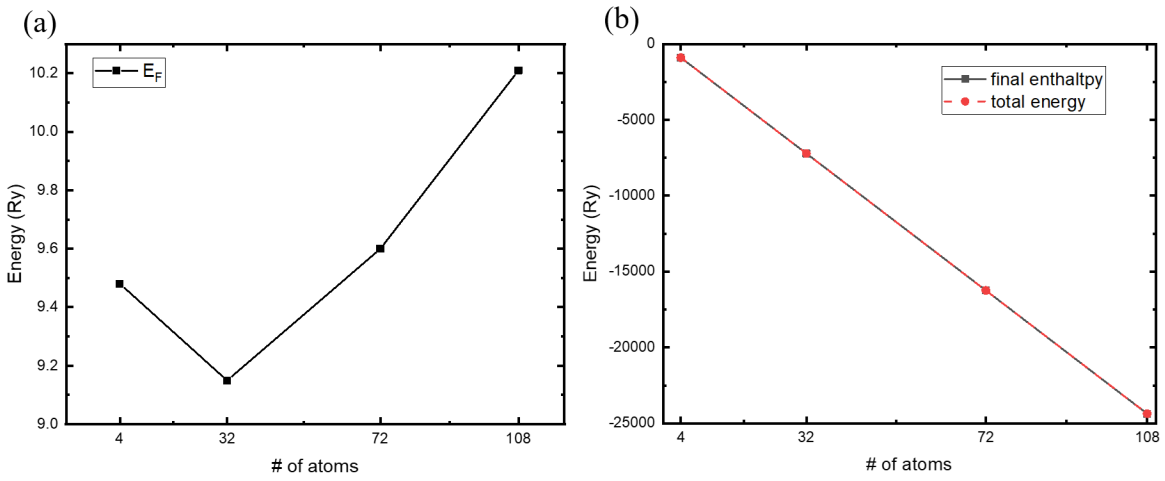

Source: Elaborated by the author (2025).
Note: (a) Fermi energy variation relative to the supercell size. (b) Final enthalpy and total energy behavior. All energy values are reported in Rydbergs (Ry).

Our main goal is to study the ZnO:Ag systems. For that, we must select a supercell size that balances accuracy and computational feasibility but allows a realistic doping framework. Our choice is the 72-atom supercell as a reference for the forthcoming calculations. This cell provides a sufficiently close representation of the bulk behavior of ZnO, minimizing finite-size effects observed in the 4-atom supercell, while still allowing efficient k-point sampling and convergence of parameters such as the energy cutoff (ecutwfc). Furthermore, the total energy and enthalpy results (Figure 3.3 (b)) indicate a significant stabilization of convergence of total energy and enthalpy starting at 72 atoms, suggesting that this size is adequate to capture the intrinsic properties of the material without the excessive numerical artifacts that can arise in even larger supercells, such as the 108-atom one, which would demand disproportionately large computational resources.

3.2 ZnO DOPED WITH Ag

With the supercell of 72 atoms well-characterized, we investigate the role of Ag doping in this system, replacing a Zn atom with an Ag atom. Ideally, one would like to dope ZnO crystals with ions such as Ag^{1+} to obtain p-doped semiconductor structures. Thus, we replace Zn^{2+} with Ag^{1+} atoms. Our goal is to validate the SQS method; therefore, we compare the results with those obtained from a structure with randomly replaced Ag atoms, chosen by us, and also the SQS-Build method. We evaluate doped systems, replacing 1, 2, 3, 4, 5, 6, 7, and 8 Zn atoms, resulting in 1.39%, 2.78%, 4.17%, 5.56%, 6.94%, 8.33%, 9.72%, and 11.11% doping concentration, respectively.

3.2.1 ZnO with Random Ag Doping

The random method consists of placing Ag dopant atoms at Zn lattice sites completely at random, without any energetic optimization or consideration of statistical correlations. Each Ag atom is positioned at a randomly chosen site, with no subsequent adjustments to stabilize or homogenize the distribution.

The random method for placing Ag dopant atoms in ZnO was chosen to simulate the disordered state, which is common in real materials, and to serve as a baseline for comparison with SQS, ensuring a comprehensive understanding of the doped system's properties. This approach is justified by its ability to model average properties over many configurations, its computational simplicity, and its alignment with theoretical frameworks like those discussed by Zunger et al. [81]. In what follows, we will investigate the electronic properties of 29 structures ranging from 1 Ag doping atom to 8 atoms.

3.2.1.1 Band Structure and DOS Analysis

We first investigate the effect of Ag doping on a 72-atom ZnO supercell in the band structure and DOS. For the resulting composition $Zn_{36}O_{35}Ag_1$, where one zinc (Zn) atom is arbitrarily replaced by an Ag atom, two different configurations are considered, see Fig. 3.4 (a) and (b). We observe that the ZnO matrix retains the WZ structure, with O and Zn atoms arranged as expected. The Ag atom is represented in green and substitutes for one of the Zn atoms in distinct positions in the two structures, simulating the random nature of doping.

Analysis of the electronic band structure (Fig. 3.4 (c) and (d)) reveals that E_F is located near the top of the valence band in both configurations. This indicates that Ag doping introduces acceptor states, a characteristic of p-type doping. The differences between the bands near E_F inthe two configurations suggest the position of the Ag dopant does not affect the electronic structure of the material. The electronic DOS, presented in Fig. 3.4 (e) and (f), reinforces this observation. A significant contribution from O orbitals is noted in the valence band region, while Ag contributes modestly, yet visibly, near E_F. The DOS at E_F is low but nonzero, indicating the presence of localized states induced by doping.

Figure 3.5 (a)-(d) shows four distinct configurations of the $Zn_{34}O_{36}Ag_2$ supercell, where two Zn atoms are substituted by two Ag atoms at different lattice positions. Each case presents a unique arrangement of Ag atoms: closely spaced in (a), far apart in (d), and in distinct local environments in (b) and (c), allowing investigation into how dopant distance and local environment affect the material's electronic properties. Figures 3.5 (e)-(h) display the corresponding electronic band structures, with energy relative to the Fermi level ($E - E_F$), revealing p-type doping as the Fermi level lies near or slightly overlaps the top of the valence band (VB). Configurations (a) and (c) exhibit an impurity level within the bandgap, indicating localized states introduced by Ag. In (a), the closely spaced Ag atoms create a pronounced impurity peak near the top of the VB, suggesting strong interaction and a deeper acceptor level, while in (c), the impurity level is less intense and shifted slightly higher, reflecting a weaker interaction due to the distinct local environment. Figures 3.5 (i)-(l) show the total and partial DOS, with O dominating the VB, Ag contributing modestly near E_F (especially between -1 and 0 eV), and non-zero DOS at E_F across all configurations, confirming acceptor levels. The difference between (a) and (c) highlights how Ag spacing and local coordination influence impurity level depth and intensity, impacting electronic behavior.

Figure 3.6 presents six different structural configurations of a ZnO supercell with three Zn atoms replaced by Ag, forming the compound $Zn_{33}O_{36}Ag_3$. We observe that the ZnO WZ structure is preserved, with local distortions occurring around the Ag atoms (green spheres). The different placement of dopants represents different substitutional scenarios, such as the DOS, the number of bands in the bandgap, and the size of the bandgap. In Figure 3.6 (d)–(f) and (m)–(o), the Fermi level (horizontal line at 0 eV) lies near or slightly above the top of the

Figure 3.4: Structural and electronic properties of the $Zn_{35}O_{36}Ag_1$ supercell

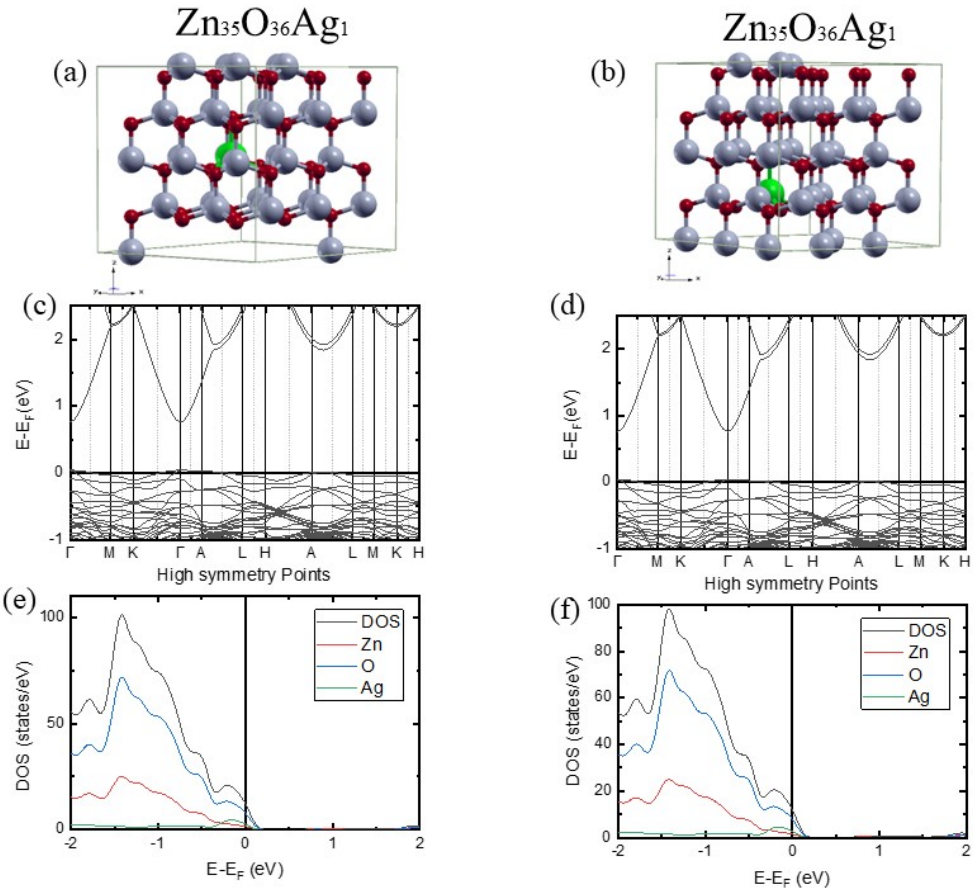

Source: Elaborated by the author (2025).
Note: (a)-(b) Visualization of 72-atom ZnO:Ag supercells with one Ag atom in different substitution sites. (c)-(d) Corresponding band structures for each configuration. (e)-(f) Density of states (DOS) analysis. The results illustrate how the Ag position influences the electronic states within the 72-atom structure.

VB, indicating a *p*-type behavior. The presence of flat bands near the Fermi level suggests localized states induced by the Ag atoms. In Figure 3.6(g)–(i) and (p)–(r), the oxygen orbitals dominate the VB, with moderate contributions from Zn and minor yet visible contributions from Ag. The Ag-induced states appear near the Fermi level, supporting the role of Ag as an acceptor dopant. The low but non-zero DOS at E_F suggests the presence of localized states rather than delocalized conduction.

Figure 3.7 (e-h) shows structure diagrams plotted along high-symmetry points in the Brillouin zone. The plots show the dispersion of electronic states, with variations indicating how Ag doping affects the electronic band structure. Notable features include the valence and conduction bands, with some configurations exhibiting shifts or new states near the E_F. Figure 3.7 (e) shows a clear energy gap between the VB (below E_F) and CB (above E_F), indicating that this configuration is a semiconductor. There are relatively flat bands near the Fermi level. In Figure 3.7 (f), the energy gap appears smaller compared to Figure 3.7 (e), and there are more states near the E_F, which indicates a metallic behavior or a transition to a semiconductor with

Figure 3.5: Structural and electronic properties of the $Zn_{34}O_{36}Ag_2$ supercell

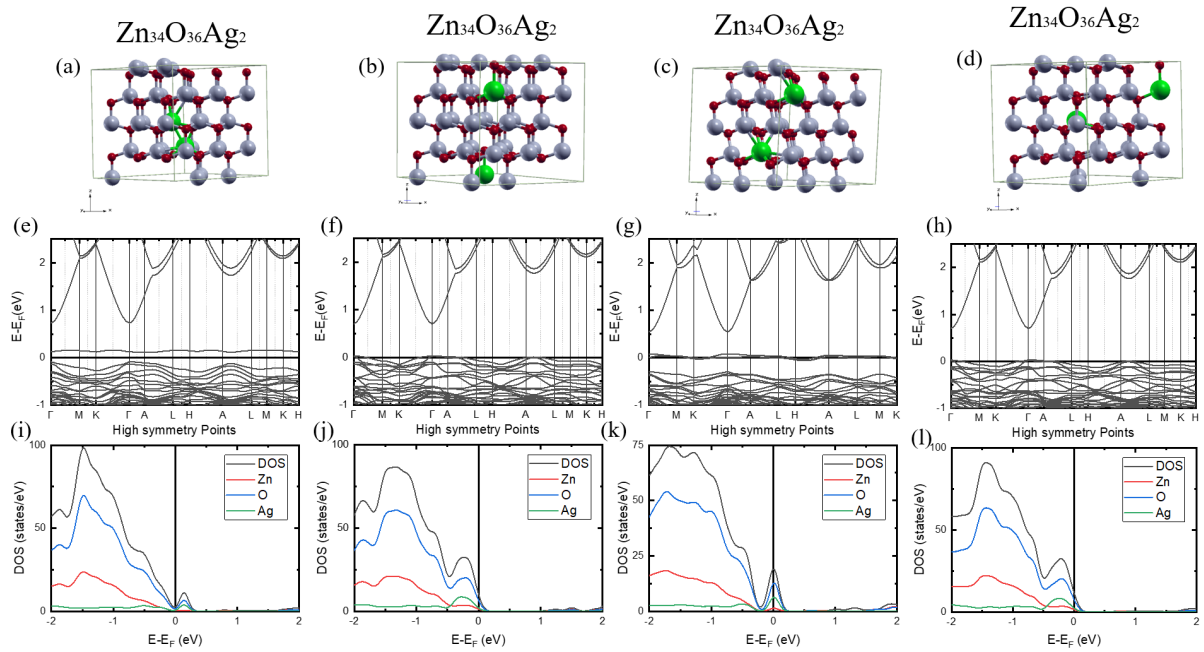

Source: Elaborated by the author (2025).
Note: (a)-(d) Visualizations of the 72-atom ZnO:Ag supercell with two Ag atoms in different configurations. (e)-(h) Corresponding electronic band structures for each arrangement. (i)-(l) Density of states (DOS) profiles showing the influence of double Ag doping on the electronic structure.

a reduced gap. The introduction of Ag may create defects or dopant states within the gap. Figure 3.7 (g) is similar to (f), but with a higher DOS near E_F, suggesting that this configuration has more electronic states available for conduction, possibly due to the position of the Ag atoms within the structure. For the fourth considered configuration, Fig. 3.7 (h), the gap is further reduced, and there is a greater mixing of states around E_F. This indicates that this configuration has either a metallic character or a degenerate semiconductor behavior, with Ag contributing significantly to states near the Fermi level.

For the first structure of this group, Zn and O dominate the states in the VB (below E_F), while Ag contributes little, with small peaks near E_F, see Fig. 3.7 (i). This suggests that in this configuration, Ag has a limited impact, and the structure retains characteristics of a gapped semiconductor. For the structure corresponding to Fig. 3.7 (j), we see an increase in the Ag contribution near the Fermi level, with more pronounced peaks. Zn and O still dominate the VB, but the Ag states in the gap region indicate the introduction of additional energy levels, possibly acting as a dopant, reducing the energy gap. For the last configuration, Fig. 3.7 (k), the Ag contribution is even more significant, with larger peaks near E_F. This reinforces the idea that Ag introduces states within the gap, potentially making the structure more conductive or altering its optical properties. Figure 3.7 (l) the DOS shows a high density of Ag states around E_F, showing that this configuration has a strong influence from Ag, possibly leading to a stronger metallic behavior or a heavily doped semiconductor.

Figure 3.6: Structural and electronic properties of the $Zn_{33}O_{36}Ag_3$ supercell

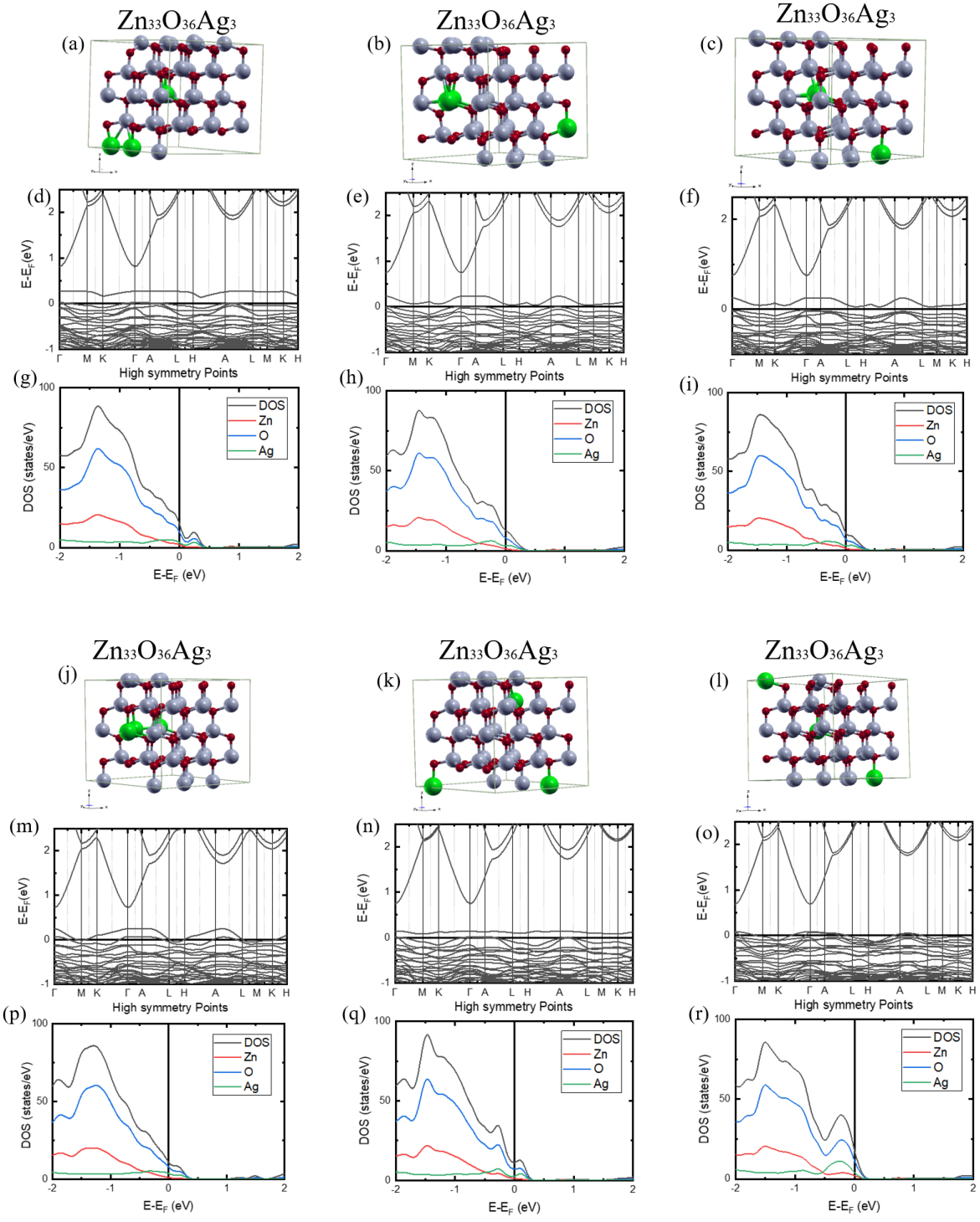

Source: Elaborated by the author (2025).
Note: (a)-(c) and (j)-(l) Atomic arrangements for six different configurations of the 72-atom ZnO supercell doped with three Ag atoms. (d)-(f) and (m)-(o) Respective electronic band structures. (g)-(i) and (p)-(r) Corresponding density of states (DOS) calculations.

We consider three different configurations for the structure containing 5 Ag atoms, see Fig. 3.8 (a)-(c). For the first structure of this group, where all Ag atoms are clustered together,

Figure 3.7: Structural and electronic properties of the $Zn_{32}O_{36}Ag_4$ supercell

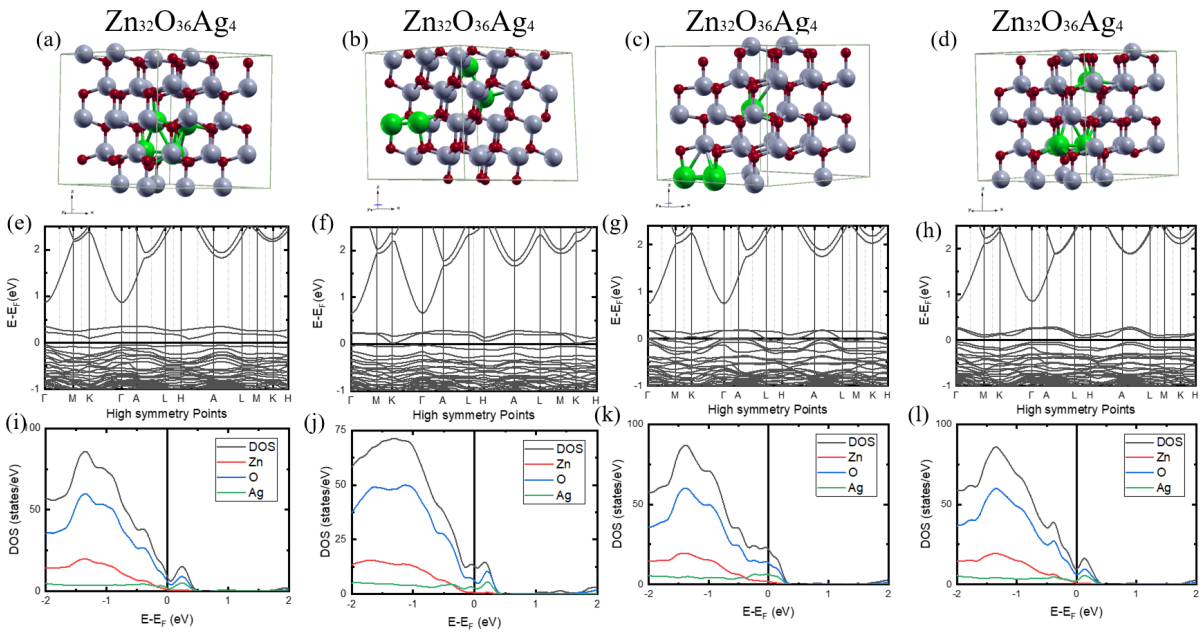

Source: Elaborated by the author (2025).
Note: (a)-(d) Atomic arrangements of the 72-atom ZnO supercell doped with four Ag atoms in different configurations. (e)-(h) Corresponding electronic band structures for each configuration. (i)-(l) Density of states (DOS) analysis showing the cumulative effect of four dopants.

we observe a visible energy gap, indicating a semiconductor behavior, with flat states near E_F, see Fig. 3.8 (d). For the second structure, the gap decreases slightly, and there are more states near E_F (Fig. 3.8 (e)). Finally, for the third structure, Fig. 3.8 (f), the gap is further reduced, with a high DOS near E_F, suggesting a metallic behavior. When looking at the character of the DOS, we notice that Zn and O dominate the VB of the first structure, with Ag introducing small states near E_F, Fig. 3.8 (g). For the second structure, Fig. 3.8 (h), we see an increased in the Ag contribution near the E_F, further reducing the gap, and for the third struture, Fig. 3.8 (i) it is quite similar to the previous one.

Comparing the structures with 4 and 5 Ag atoms, we observe a more pronounced reduction in the energy gap and a higher DOS near the Fermi level. This suggests that higher Ag doping enhances conductivity and may shift the material toward metallic behavior. These properties make $Zn_{31}O_{36}Ag_5$, 6.94%, potentially more suitable for applications requiring higher conductivity, such as optoelectronic devices or catalysts.

Next, we evaluate four different configurations for the composition $Zn_{30}O_{36}Ag_6$, shown in Fig. 3.9 (a)–(d). In Fig. 3.9 (a), two groups of three Ag atoms form clusters. The band structure in Fig. 3.9 (e) shows that an energy gap is still visible between the VB (below E_F) and CB (above E_F), but smaller than in configurations with fewer Ag, indicating a transition toward mettalic behavior. The corresponding DOS in Fig. 3.9 (i) reveals a moderate increase of states near E_F, especially influenced by Ag.

In Fig. 3.9 (b), the Ag atoms are positioned as nearest neighbors. The band structure in

Figure 3.8: Structural and electronic properties of the $Zn_{31}O_{36}Ag_5$ supercell

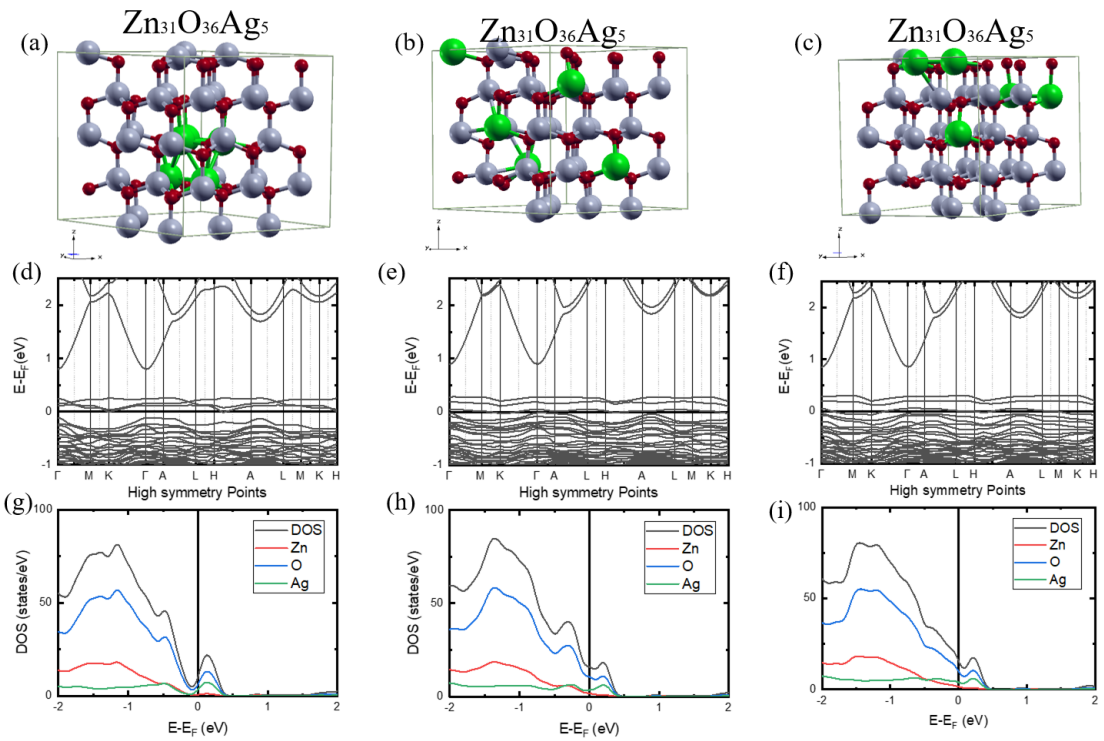

Source: Elaborated by the author (2025).
Note: (a)-(c) Visualizations of the 72-atom ZnO supercell doped with five Ag atoms in different configurations. (d)-(f) Corresponding electronic band structures. (g)-(i) Density of states (DOS) for each respective arrangement.

Fig. 3.9 (f) exhibits a narrower gap and higher density of states near the Fermi level, suggesting stronger hybridization and possibly metallic behavior. This is supported by the DOS in Fig. 3.9 (j), where states contributed by Ag dominate around E_F.

For the third configuration, Fig. 3.9 (c), the band structure in Fig. 3.9 (g) shows almost no visible gap and a flat band near the Fermi level, indicating enhanced conductivity. However, upon visual inspection, this structure appears to contain only four Ag atoms, despite the label. This discrepancy needs verification. Still, the DOS in Fig. 3.9 (k) confirms a high density of states near E_F, reinforcing the metallic character.

Finally, in Fig. 3.9 (d), the Ag atoms form a compact arrangement. The band structure in Fig. 3.9 (h) shows no band gap and a high density of overlapping bands at E_F, indicating metallic behavior. The DOS in Fig. 3.9 (l) also displays a significant contribution from Ag around E_F, confirming the dominant role of Ag in tuning the electronic properties.

In Fig. 3.9 (i) Zn and O still dominate the states in the valence bands, but Ag shows more pronounced peaks near E_f compared to previous configurations. This indicates that Ag is introducing more states into the gap, further reducing the semiconductor properties. In Fig. 3.9 (j) the contribution of Ag near the Fermi level is even more significant, with high peaks. This reinforces the reduction of the gap and the increase in conductivity. In Fig. 3.9 (k), the density of states of Ag around E_f is very high, suggesting that Ag is dominating the electronic states

near the Fermi level, which is consistent with the metallic behavior observed in In Fig. 3.9 (g). In Fig. 3.9 (l) the contribution of Ag is extremely high near E_f, with peaks indicating a strong doping influence. This confirms that this configuration exhibits metallic characteristics, with Ag completely filling the gap.

$Zn_{30}O_{36}Ag_6$ (6 Ag atoms) shows an even greater reduction in the energy gap compared to $Zn_{32}O_{36}Ag_4$ (4 Ag) and$Zn_{31}O_{36}Ag_5$ (5 Ag). While $Zn_{32}O_{36}Ag_4$ still exhibited semiconductor characteristics in some configurations, and $Zn_{31}O_{36}Ag_5$ showed a transition to a metallic, $Zn_{30}O_{36}Ag_6$ displays predominantly metallic behavior, especially in the configurations shown in Fig. 3.9 (g) and (h). The contribution of Ag in the DOS progressively increases with the number of Ag atoms. In $Zn_{30}O_{36}Ag_6$, the Ag peaks near E_F are higher and broader, indicating a greater density of states and a stronger doping effect. The addition of more Ag (from 4 to 6 atoms) leads to a clear transition from semiconductor to metallic behavior, with the energy gap almost completely disappearing in some configurations of $Zn_{30}O_{36}Ag_6$.

Figure 3.9: Structural and electronic properties of the $Zn_{30}O_{36}Ag_6$ supercell

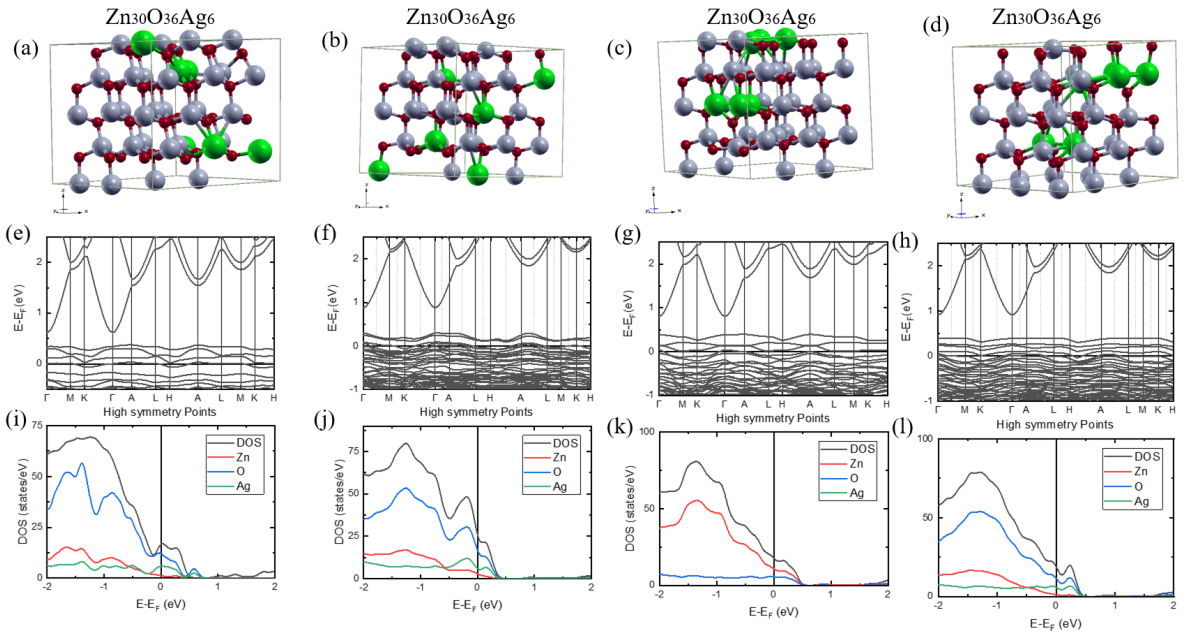

Source: Elaborated by the author (2025).
Note: (a)-(d) Atomic arrangements of the 72-atom ZnO supercell doped with six Ag atoms in different configurations. (e)-(h) Corresponding electronic band structures for each arrangement. (i)-(l) Density of states (DOS) profiles showing the high-concentration doping effects.

The graphs presented in Figure 3.10 provide a detailed analysis of the electronic properties of three distinct configurations of the compound $Zn_{29}O_{36}Ag_7$. Panels (a), (b), and (c) illustrate the structural configurations, highlighting the different positions of the silver atoms (in green) within the ZnO crystal lattice. This variation in the location of the silver impurity is critical, as small changes in the atomic structure can significantly impact the electronic properties of the material, directly influencing how electrons behave and distribute across energy states. The analysis of the electronic band structure diagrams (d), (e), and (f), along with the DOS plots

(g), (h), and (i), reveals that silver doping and the structural configuration notably alter the electronic landscape of ZnO. The presence of states at the Fermi level in all three configurations, as indicated by the DOS graphs, suggests that these materials may exhibit metallic behaviour or behave as degenerate semiconductors. The contributions from Zn, O, and, crucially, Ag near the Fermi level demonstrate the active role of silver in modulating the electronic properties.

Figure 3.10: Structural and electronic properties of the $Zn_{29}O_{36}Ag_7$ supercell

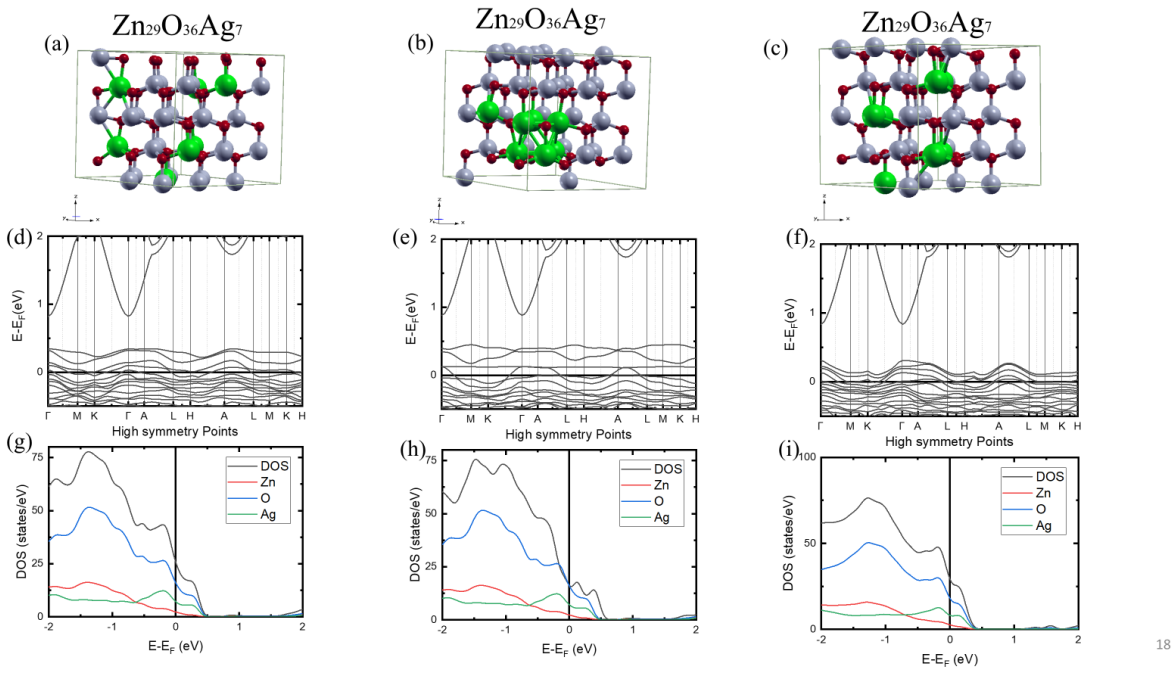

Source: Elaborated by the author (2025).
Note: (a)-(c) Visualizations of the 72-atom ZnO supercell doped with seven Ag atoms in different configurations. (d)-(f) Corresponding electronic band structures for each arrangement. (g)-(i) Density of states (DOS) profiles.

For our last doping concentration, $Zn_{28}O_{36}Ag_8$, we analyze three different structures, Fig. 3.11 (a)-(c). For the first configuration, we see that the states cross the E_F, see Fig. 3.11 (e), indicating a clear metallic behavior. The high DOS around E_F shows that Ag has a significant impact. In Fig. 3.11 (f), a similar behavior is observed; there is no gap, and the states around E_F are even denser. This reinforces the metallic behavior, with Ag fully filling any previously existing gap. In Fig. 3.11 (g), the behavior is consistently metallic, with a high density of states crossing the Fermi level. The band structure shows that the material has completely lost its semiconductor characteristics. In Fig. 3.11 (i), the contribution of Ag near E_F is very high, with significant peaks. Zn and O still contribute to the VB states, but Ag dominates the states near the Fermi level, consistent with metallic behavior. In Fig. 3.11 (j), the DOS of Ag around E_F is even more pronounced, with higher and broader peaks. This indicates that Ag introduces a substantial number of states, eliminating any remaining gap. In Fig. 3.11 (k) Ag shows an extremely high DOS near E_F, with dominant peaks. This confirms that the material exhibits metallic characteristics, with Ag playing a crucial role in conduction, in all possible configura-

tions considered.

Figure 3.11: Structural and electronic properties of the $Zn_{28}O_{36}Ag_8$ supercell

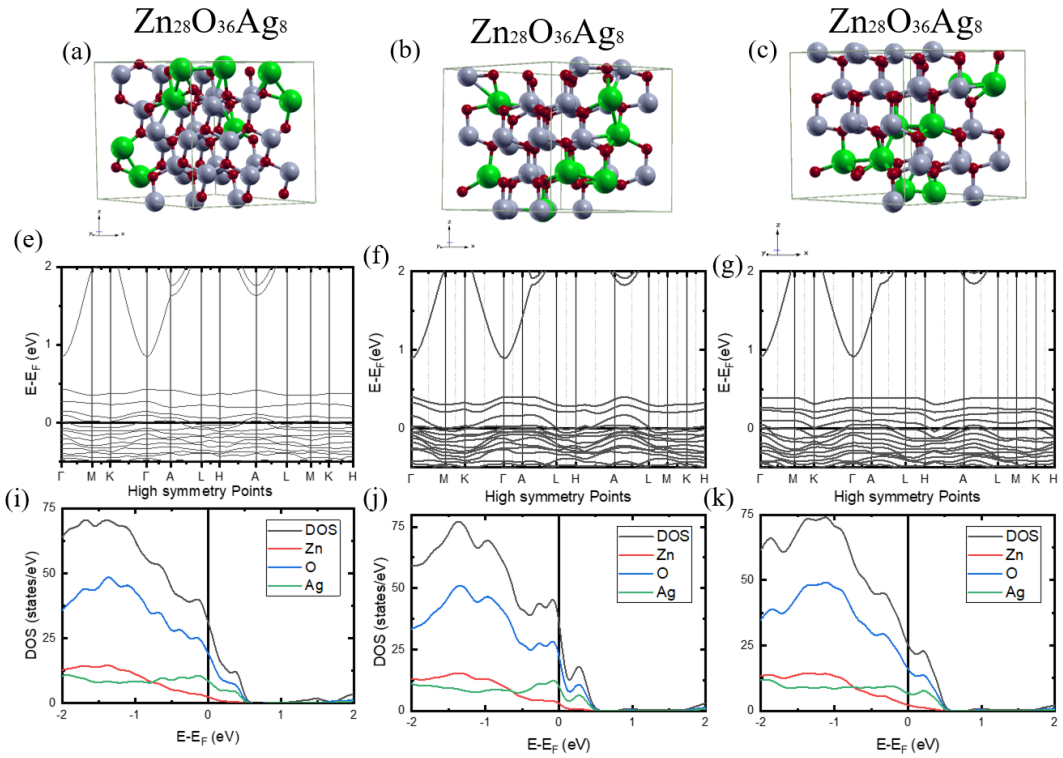

Source: Elaborated by the author (2025).
Note: (a)-(c) Visualizations of the 72-atom ZnO supercell doped with eight Ag atoms in different configurations. (d)-(f) Corresponding electronic band structures. (g)-(i) Density of states (DOS) analysis for each configuration.

We ask ourselves if a system with 72 atoms would be enough to infer conclusions of a real system, and to clarify this, we have analyzed systems with 108 atoms. We conclude that all the electronic characteristics were similar, if not identical, to the systems with 72 atoms (see appendix for details). For computational efficiency, we could safely proceed with our analyses with a system with 72 atoms. As one can notice, we have obtained different electronic properties for configurations with the same doping concentrations, which one is the most favorable one is a difficult question to answer because the permutation of atom positions increases with the number of atoms. To optimize and accelerate the search for the ideal structure, we use two different versions of the SQS method.

Let's analyze the band structures Fig. 3.12 (d-f) and the density of states (DOS) diagrams 3.12 (g-i) for the $Zn_{53}O_{54}Ag_1$ and $Zn_{52}O_{54}Ag_2$ configurations. These configurations have a higher proportion of Zn and O compared to the previous ones, with a smaller amount of Ag (1 or 2 atoms), which can significantly alter the electronic properties.

In the Fig. 3.12 (d) - $Zn_{53}O_{54}Ag_1$, a clear energy gap exists between the valence bands (below E_f) and conduction bands (above E_f), indicating that this configuration is a semiconductor. The gap is relatively wide, suggesting that the introduction of only one Ag atom has

a limited impact on gap reduction. In the Fig. 3.12 (e) $Zn_{52}O_{54}Ag_2$, the energy gap is still present but visibly smaller than in Fig. 3.12 (d). This indicates that the addition of a second Ag atom reduces the gap, making the structure resemble a more finely tuned semiconductor. In Fig. 3.12 (f) - $Zn_{52}O_{54}Ag_2$ (different configuration), the gap is even smaller than in Fig. 3.12 (e), but still present. The presence of states closer to the Fermi level suggests that the position of Ag atoms in the structure affects the gap width, although the configuration still retains semiconductor characteristics. In the Fig. 3.12 (g) - $Zn_{53}O_{54}Ag_1$ Zn and O dominate the states in both the valence and conduction bands, with a very small contribution from Ag near E_F. This is consistent with semiconductor behavior, as the single Ag atom introduces few states in the gap due to its low concentration. In Fig. 3.12 (h) - $Zn_{52}O_{54}Ag_2$ the contribution of Ag near the Fermi level slightly increases, with small but more visible peaks than in Fig. 3.12 (g). This indicates that two Ag atoms introduce more states into the gap, reducing it and increasing the likelihood of conduction. In the Fig. 3.12 (i) - $Zn_{52}O_{54}Ag_2$ (different configuration), the density of states from Ag near E_F is slightly higher than in panel (h), with more pronounced peaks. This suggests that the configuration of Ag atoms affects the number of states introduced into the gap, but the material still retains semiconductor characteristics.

Figure 3.12: Structural and electronic properties of 108-atom ZnO supercells with Ag doping

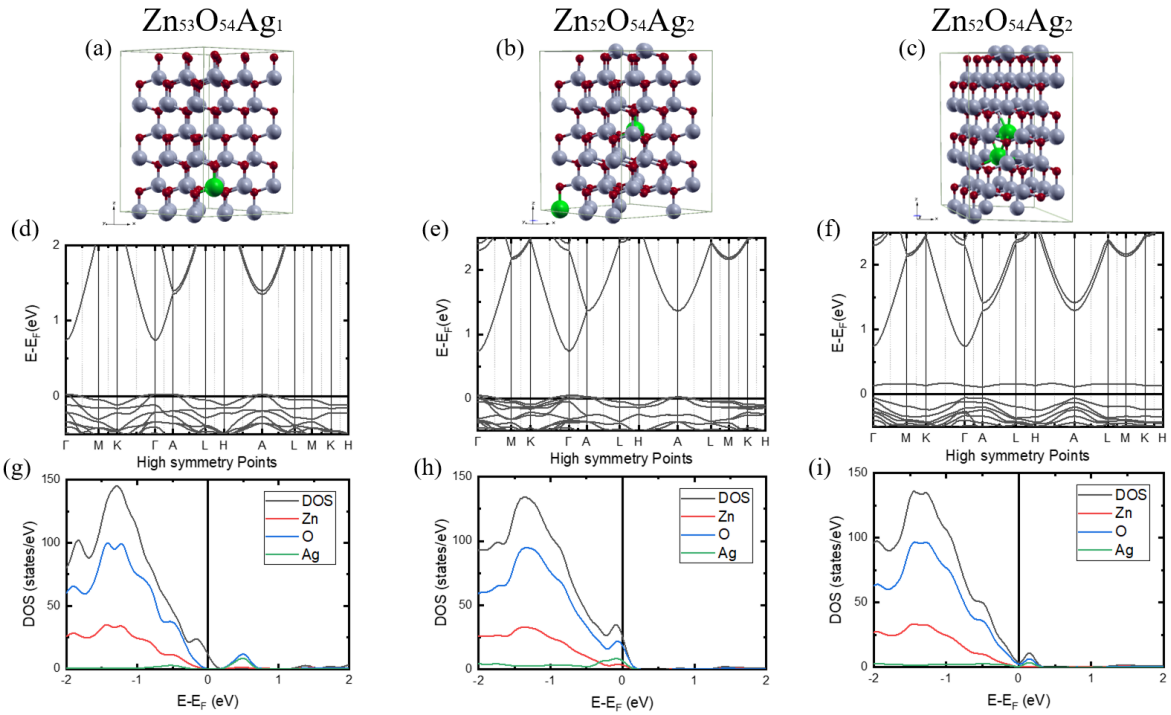

Source: Elaborated by the author (2025).
Note: (a)-(c) Visualization of the 108-atom ZnO supercell doped with one, two, and two Ag atoms in different configurations. (d)-(f) Corresponding electronic band structures for each case. (g)-(i) Density of states (DOS) profiles.

3.2.2 SQS-build

The SQS-build method refers to an approach in which initially random structures are generated and subsequently optimized to find the lowest-energy configuration, usually through geometric relaxation. Unlike the traditional SQS method, which emphasizes the statistical correlations of disorder, SQS-build prioritizes the energetic stability of the system. Thus, the initial randomness is adjusted until the structure reaches an energetically favorable state, although this may result in less uniform or more clustered distributions of Ag atoms. This approach can be inferred in specific cases, such as the $Zn30O36Ag_6$ structure, where variations in configurations indicate a process of energy optimization.

3.2.2.1 Band Structure and DOS Analysis

For the SQS-build method we compare pure $Zn_{36}O_{36}$ with $Zn_{35}O_{36}Ag_1$ in Fig. 3.13. We observe that the undoped system, Fig. 3.13 (a), exhibits a symmetric WZ structure, typical of pure ZnO, without distortions, reflecting its classical semiconductor properties, confirmed by it band structure displayed in Fig. 3.13 (c). In contrast, the $Zn_{35}O_{36}Ag_1$ system introduces a small local distortion due to the presence of one Ag atom, with the overall symmetry of the cell being preserved. This results in a slight reduction of the energy gap, while still maintaining semiconductor characteristics. Also, we see that in Fig. 3.13 (c) there is a well-defined energy gap between the VB (below E_F) and the CV (above E_F), indicating that $Zn_{36}O_{36}$ is an intrinsic semiconductor. Figure 3.13 (d) shows that the energy gap of $Zn_{35}O_{36}Ag_1$ is still present but visibly smaller than in $Zn_{36}O_{36}$. The introduction of one Ag atom creates additional states near the Fermi level, reducing the gap. The structure retains semiconductor characteristics, but with a reduced gap, indicating that Ag acts as a light dopant. Figure 3.13 (e) and (f) present the DOS of both systems. For $Zn_{36}O_{36}$, Zn and O fully dominate the electronic states, with Zn contributing more to the CB and O to the VB. As expected, in pure ZnO, the energy gap is evident, with no states near E_F. This is typical of a pure semiconductor like ZnO. The introduction of one Ag atom adds a small contribution to the DOS near the Fermi level, visible as discrete green peaks. Zn and O still dominate the VB and CB, respectively, but the Ag states within the gap indicate that the dopant is beginning to influence the electronic properties, reducing the gap and potentially increasing conductivity.

Figure 3.14 shows the configurations obtained for $Zn_{34}O_{36}Ag_2$ and $Zn_{33}O_{36}Ag_3$. For the system with two Ag we still observe an energy gap (Fig. 3.14 (c)). However, it is smaller than in the $Zn_{35}O_{36}Ag_1$ system (previously analyzed). The presence of two Ag atoms introduces additional states near the Fermi level (E_F), reducing the gap and indicating that the structure retains semiconductor characteristics, though modified by doping. For the configuration with

Figure 3.13: Pure and Ag-doped ZnO structures generated via SQS-build

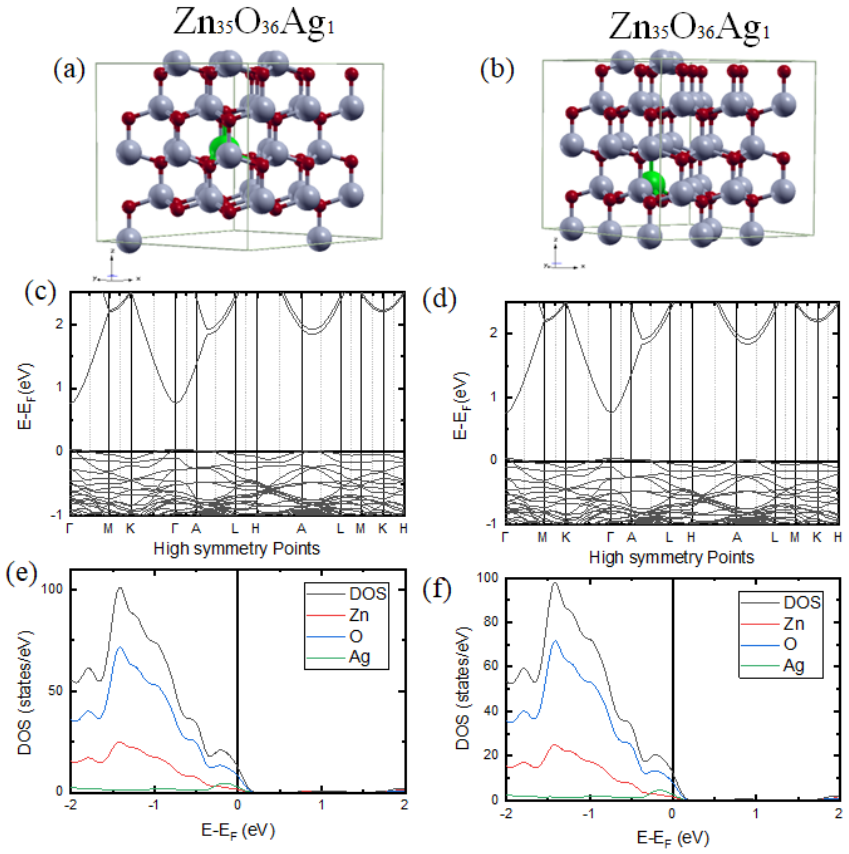

Source: Elaborated by the author (2025).
Note: (a)-(b) Visualization of 72-atom supercells for pure ZnO and ZnO:Ag (1 Ag atom) obtained through the Special Quasirandom Structure (SQS) method. (c)-(d) Corresponding electronic band structures. (e)-(f) Density of states (DOS) analysis.

three Ag atoms, Fig. 3.14 (d), the energy gap is further reduced compared to $Zn_{34}O_{36}Ag_2$, with more states appearing near E_F. This suggests that the addition of a third Ag atom narrows the gap even more, pushing the structure toward degenerate semiconductor behavior, though it remains non-metallic. The character of the electronic bands for the $Zn_{34}O_{36}Ag_2$ system has Zn and O dominating the VB and CB, respectively, but the contribution of the Ag atom is visible as small peaks near E_F which are more pronounced than the $Zn_{35}O_{36}Ag_1$. This indicates that the two Ag atoms introduce more states into the gap, narrowing it and increasing the possibility of electronic conduction. Likewise, in the Fig. 3.14 (f) - $Zn_{33}O_{36}Ag_3$, the contribution from Ag near E_F is even more significant, with higher and broader peaks than in the $Zn_{34}O_{36}Ag_2$ system. This reflects the increasing influence of Ag doping, further filling the gap and moving the material toward a more conductive behavior.

We present in Fig. 3.15 the results for structures with 4 and 5 Ag atoms. The Ag atoms substitute Zn in the WZ ZnO lattice, causing more significant local distortions compared to configurations with fewer Ag atoms. The four Ag atoms are distributed throughout the cell.

Figure 3.14: Electronic properties of SQS-generated ZnO:Ag with 2 and 3 Ag atoms

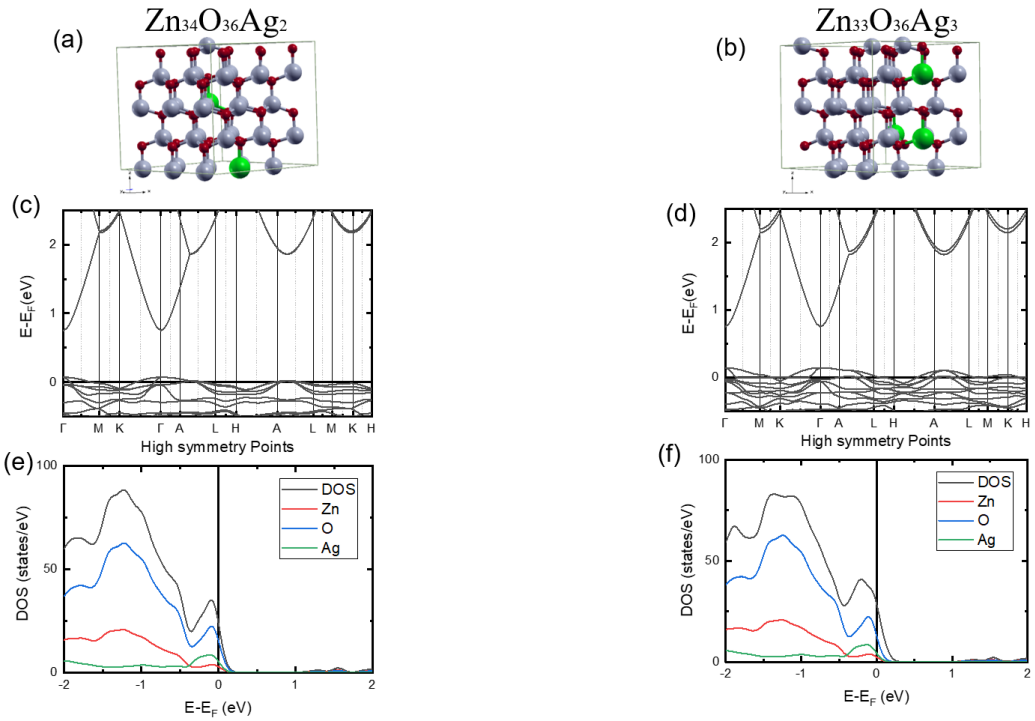

Source: Elaborated by the author (2025)..
Note: (a)-(b) Visualizations of 72-atom ZnO:Ag supercells containing two and three Ag atoms, respectively, modeled using the SQS method. (c)-(d) Corresponding electronic band structures. (e)-(f) Density of states (DOS) for both configurations.

Their presence may lead to Ag–Ag interactions depending on proximity, affecting the symmetry of the lattice. For Fig. 3.15 (b) - $Zn_{31}O_{36}Ag_5$ with five Ag atoms, the structure presents a higher dopant concentration. This results in even more pronounced distortions in the WZ lattice, with increased likelihood of Ag–Ag interactions, as shown. The cell symmetry is more affected, and the structure may exhibit local defects or regions of greater deformation, this will be discussed in the upcoming sections.

When analyzing the band structure of 3.15 (c) - $Zn_{32}O_{36}Ag_4$, we still see an energy gap, but it is significantly smaller than in $Zn_{34}O_{36}Ag_2$ and $Zn_{33}O_{36}Ag_3$. The presence of four Ag atoms introduces more states near E_F, reducing the gap and indicating that the structure is transitioning from a semiconductor to a metallic. In the band structure of $Zn_{31}O_{36}Ag_5$, Fig. 3.15 (d), the energy gap is even smaller than in $Zn_{32}O_{36}Ag_4$, with a higher density of states near the Fermi level. This suggests that the addition of a fifth Ag atom brings the structure even closer to metallic behavior, although a small gap may still be present, characterizing a metal. The graph in Fig. 3.15 (e) - $Zn_{32}O_{36}Ag_4$ Zn and O still dominate the VB and CB, but Ag shows more pronounced peaks near E_F, higher than in $Zn_{33}O_{36}Ag_3$. This indicates that the four Ag atoms introduce a significant number of states within the gap, narrowing it and increasing the likelihood of conduction and Fig. 3.15 (f) - $Zn_{31}O_{36}Ag_5$ the contribution from Ag near E_F is even more substantial, with higher and broader peaks than in $Zn_{32}O_{36}Ag_4$. This reflects the growing

impact of Ag, nearly filling the gap and leading to more conductive properties, consistent with a transition toward metallic behavior.

Figure 3.15: Electronic properties of SQS-generated ZnO:Ag with 4 and 5 Ag atoms

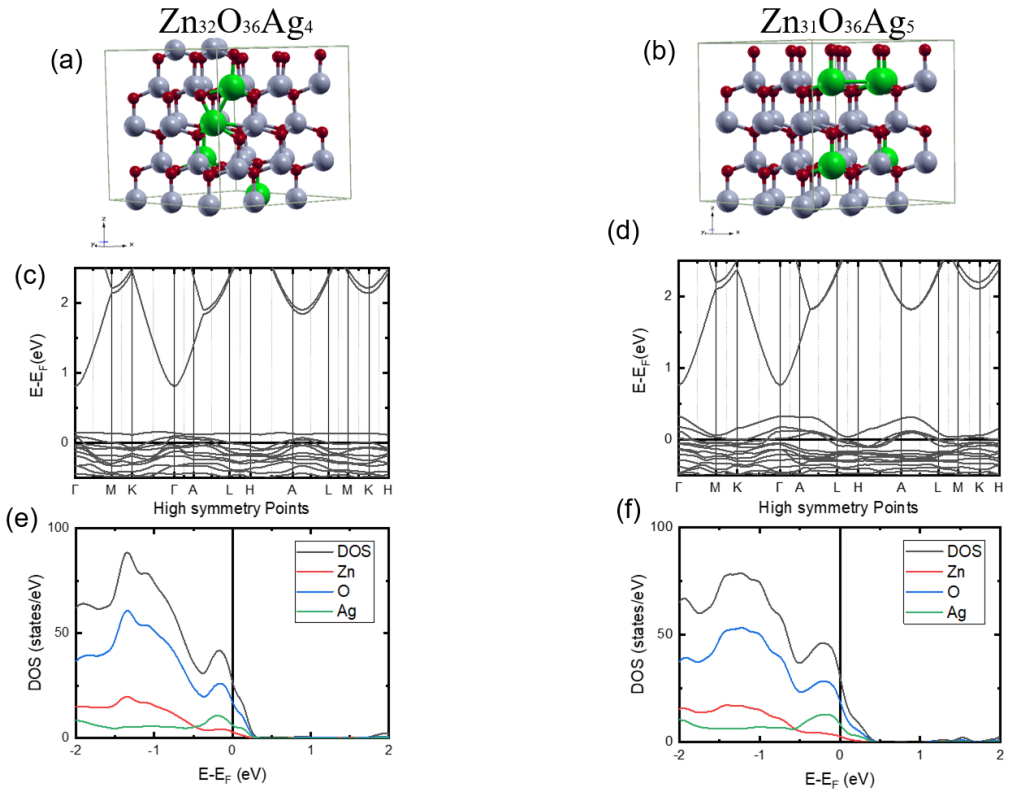

Source: Elaborated by the author (2025).
Note: (a)-(b) Visualizations of 72-atom ZnO:Ag supercells containing four and five Ag atoms, respectively, modeled using the SQS method. (c)-(d) Corresponding electronic band structures. (e)-(f) Density of states (DOS) for each respective concentration.

Interesting, for the concentration with six Ag atoms, there are 2 energy equivalent structures, Fig. 3.16 (a) and (b). The first one has three Ag atoms grouped in 2 clusters, while the second one had them separated. For the first one, Fig. 3.16 (c) - Zn_{30} $O_{36}Ag_6$, the energy gap is highly reduced, with states crossing the Fermi level. This indicates that the structure exhibits metallic behavior characteristics due to the high concentration of Ag (six atoms). By comparison, the second one, displayed in Fig. 3.16 (d) - $Zn_{30}O_{36}Ag_6$, is similar to Fig. 3.16 (c), the gap is minimal, with a high density of states near E_F. The variation in the positions of Ag atoms does not significantly change the metallic behavior but may slightly modify the distribution of the states, similar to the 3.9 (f) configuration. In Fig. 3.16 (e) - $Zn_{30}O_{36}Ag_6$ Zn and O still dominate the valence and conduction bands, but Ag shows significant peaks near E_F, higher than those in $Zn_{31}O_{36}Ag_5$. This indicates that six Ag atoms introduce a substantial number of states within the gap, filling it and resulting in metallic behavior. Figure 3.16 (f) - $Zn_{30}O_{36}Ag_6$ the contribution from Ag near E_F is even more pronounced, with tall and broad peaks, similar to graph 3.16 (e). The variation in the arrangement of Ag atoms further reinforces the dopant's

impact, confirming the metallic nature of the structure.

Figure 3.16: Electronic properties of the SQS-generated ZnO:Ag supercell with 6 Ag atoms

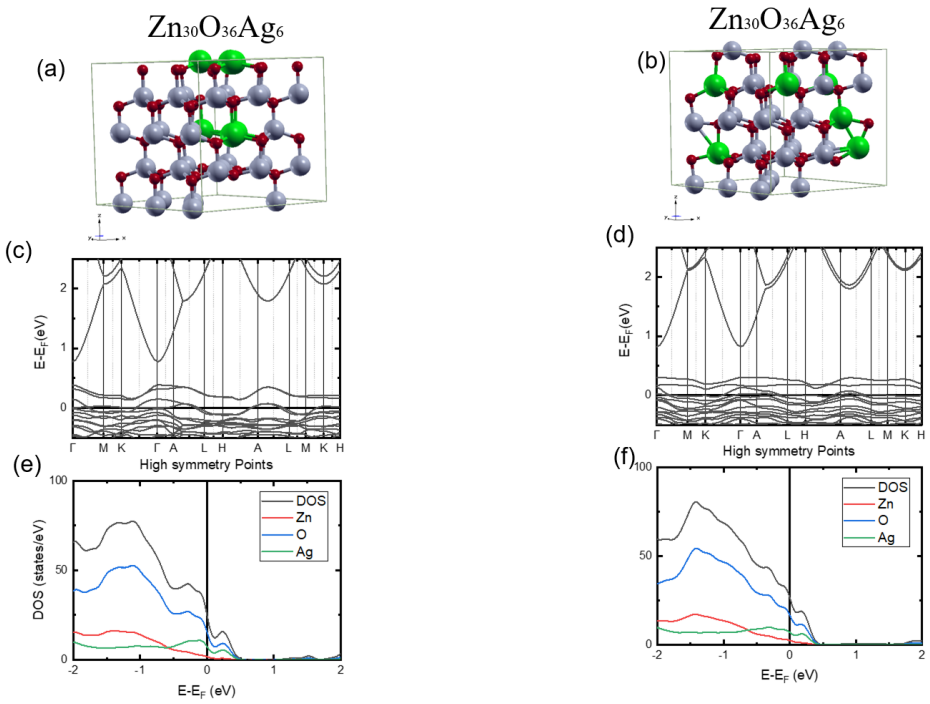

Source: Elaborated by the author (2025). **Note:** (a)-(b) Visualizations of the 72-atom ZnO:Ag supercell containing six Ag atoms modeled using the SQS method. (c)-(d) Corresponding electronic band structures. (e)-(f) Density of states (DOS) analysis showing the effects of high-concentration random doping.

Lastly, we present the results for the configurations with seven and eight Ag atoms in Fig. 3.17. The analysis of the band structure of Fig.3.17 (c) - $Zn_{29}O_{36}Ag_7$ shows that the energy gap is virtually nonexistent at zero, with states crossing the Fermi level. This indicates clear metallic behavior, resulting from the high Ag concentration (7 atoms), which fills the gap and 3.16 (d) - $Zn_{28}O_{36}Ag_8$ happens the same as 3.16 (c), no visible gap is observed around 0 energy, with a high density of states crossing E_F. The addition of an eighth Ag atom reinforces the metallic character, with the structure fully dominated by doping effects. Fig. 3.16 (e) - $Zn_{29}O_{36}Ag_7$ Zn and O still contribute to the valence and conduction bands, but Ag shows very high and broad peaks near E_F, larger than in $Zn_{30}O_{36}Ag_6$. This confirms that the 7 Ag atoms dominate the electronic states, leading to metallic behavior, and 3.16 (f) - $Zn_{28}O_{36}Ag_8$, the Ag contribution near E_F is even more pronounced, with even higher and wider peaks. The 8 Ag atoms maximize the doping impact, completely filling the gap and consolidating metallic properties. It is worth noting that the distribution of Ag atoms in the SQS-method structures (Fig. 3.17) differs significantly from random configurations (Fig. 3.10 and Fig. 3.11). These differences are visible in both the atomic arrangements and the resulting electronic properties, highlighting the importance of using SQS to realistically represent dopant distribution in disordered systems.

For the structures obtained via SQS-build, the WZ lattice of ZnO is preserved at low doping

Figure 3.17: Electronic properties of SQS-generated ZnO:Ag with 7 and 8 Ag atoms

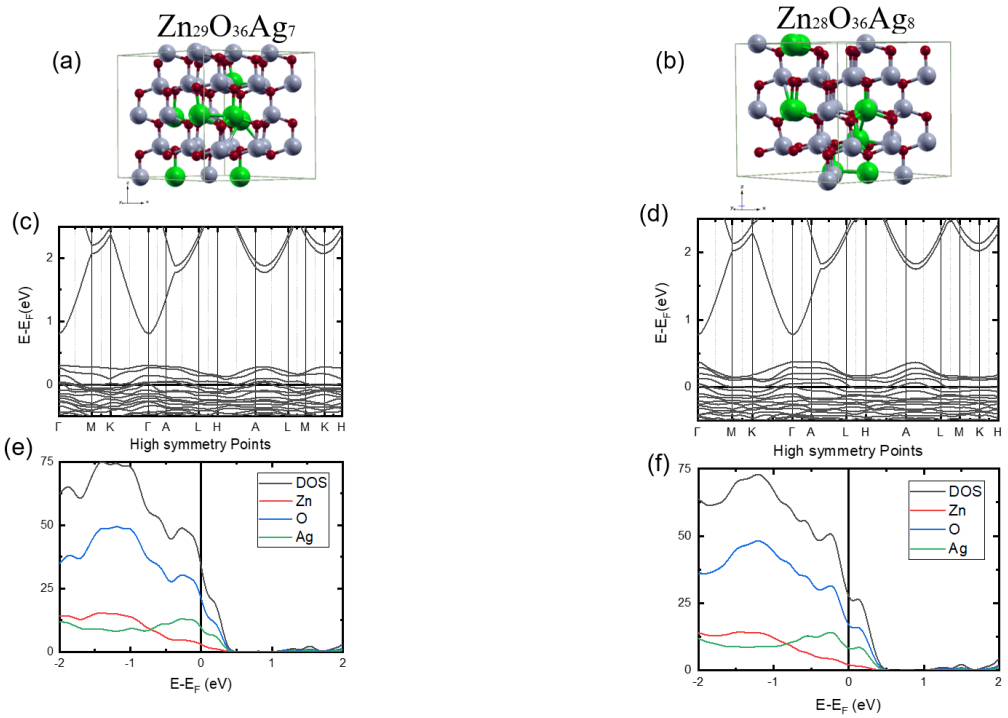

Source: Elaborated by the author (2025).
Note: (a)-(b) Visualizations of the 72-atom ZnO:Ag supercells containing seven and eight Ag atoms, respectively, modeled using the SQS method. (c)-(d) Corresponding electronic band structures. (e)-(f) Density of states (DOS) profiles showing the high-concentration effects on the valence and conduction bands.

levels (0-3 Ag), but increasingly distorted with 4–8 Ag atoms, leading to structural disorder in $Zn_{28}O_{36}Ag_8$. From pure semiconductor behavior ($Zn_{36}O_{36}$) to metallic ($Zn_{28}O_{36}Ag_7$), Ag doping progressively reduces the band gap and enhances conductivity, with $Zn_{30}O_{36}Ag_6$ marking a turning point. Configurations with 0–3 Ag atoms are suitable for semiconductor applications (e.g., optoelectronic devices), while 6–8 Ag atoms are more appropriate for high-conductivity uses (e.g., electrodes).

3.2.3 Special Quasirandom Structures for ZnO doped with Ag

The SQS method consists of generating optimized structures that simulate the randomness found in solid solutions by distributing dopant atoms (Ag) so as to replicate the statistical correlations characteristic of a disordered lattice, but within a small periodic cell. This optimization considers correlations involving pairs, triplets, and sometimes quadruplets of atoms, aiming to maximize the similarity of the generated structure to ideal randomness.

It is important to note that the SQS method does not seek to minimize the total energy of the structure, but rather to provide a realistic statistical representation of disorder in the crystal lattice. To this end, it employs algorithms based on interaction energies that adjust the distribution

of Ag atoms. In the present study, the SQS method was applied in all analyzed configurations, ensuring a quasirandom distribution of silver atoms in the WZ lattice of ZnO. The (SQS) were generated using the ICET Python package, which employs Monte Carlo simulated annealing to optimize the correlation functions.

3.2.3.1 Band Structure and DOS Analysis

Figure 3.18: Electronic properties of SQS-generated ZnO:Ag with 1 and 2 Ag atoms

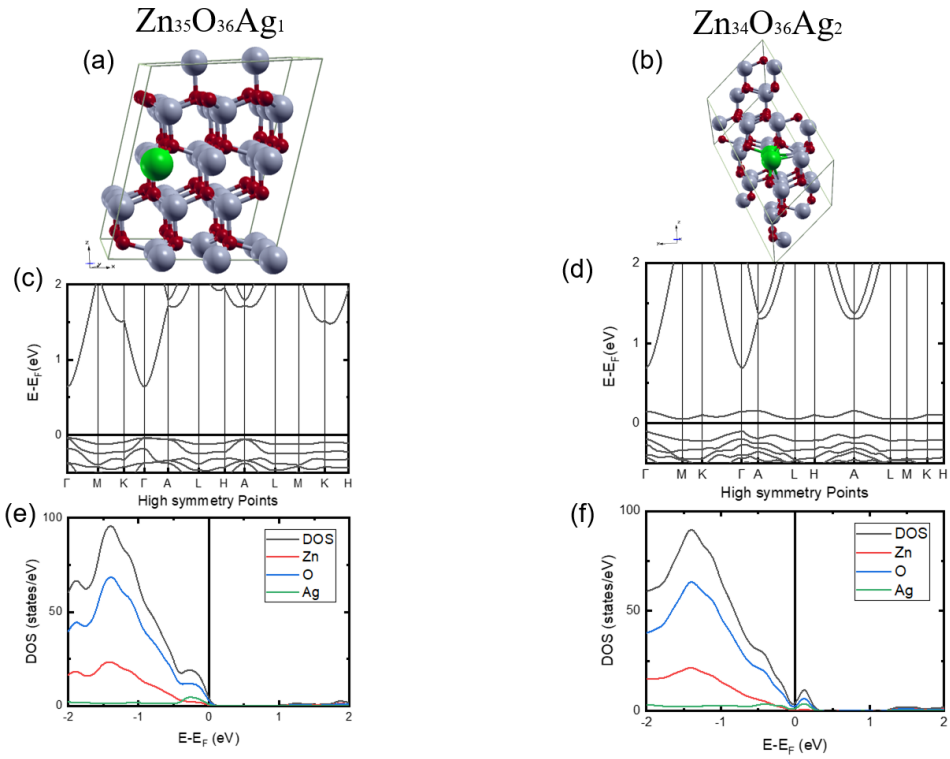

Source: Elaborated by the author (2025).
Note: (a)-(b) Visualizations of 72-atom ZnO:Ag supercells with one and two Ag atoms, respectively, modeled using the SQS method. (c)-(d) Corresponding electronic band structures. (e)-(f) Density of states (DOS) analysis for each configuration.

Figure 3.18 shows the atomic structures, electronic band structures, and DOS for $Zn_{35}O_{36}Ag_1$ and $Zn_{34}O_{36}Ag_2$, generated using the SQS method. Also, it illustrates the minimal structural distortions due to Ag doping, the preserved band gaps indicative of semiconducting behavior, and the DOS contributions from Zn, O, and Ag. These results highlight the impact of low Ag concentrations on the electronic properties of ZnO. Different from the previous cases, the band gap in the structure containing two Ag atoms, Fig. 3.18 (d), is smaller than the one with one Ag atom, Fig. 3.18 (e), with a higher DOS near the Fermi level. This is mainly due to the clustering of the Ag atoms in the $Zn_{23}O_{36}Ag_2$, forming a metallic Ag particle. Consequently, the two Ag atoms further reduce the gap, maintaining the structure as a semiconductor, but with a clear

impurity level within the gap.

The structures of $Zn_{33}O_{36}Ag_3$ and $Zn_{32}O_{36}Ag_4$ are presented in Fig. 3.19. Here, we see a clear preference for clustering Ag atoms in pairs. The addition of three and four Ag atoms introduces local distortions and alters the electronic states, reducing the band gap and increasing the DOS near the Fermi level. In both cases, a clear impurity level is observed, leading to a phase toward degenerate semiconductor behavior, highlighting the influence of impurity concentration on the transition from semiconducting to conducting properties.

Figure 3.19: Electronic properties of SQS-generated ZnO:Ag with 3 and 4 Ag atoms

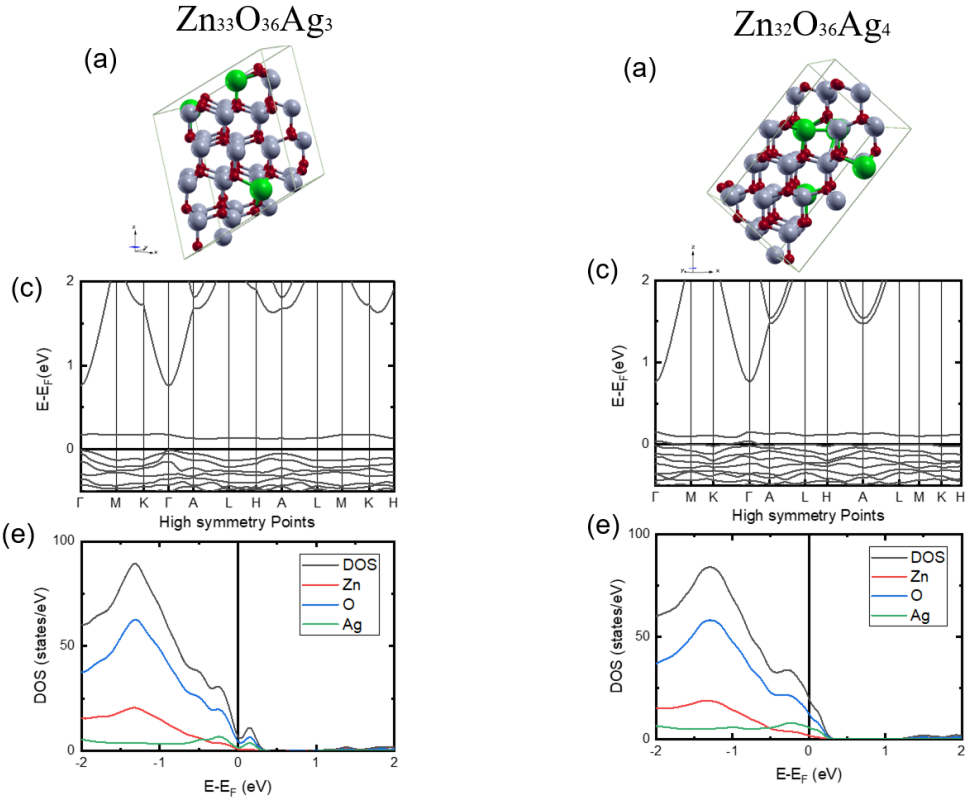

Source: Elaborated by the author (2025).
Note: (a)-(b) Visualizations of 72-atom ZnO:Ag supercells containing three and four Ag atoms, respectively, modeled using the SQS method. (c)-(d) Corresponding electronic band structures. (e)-(f) Density of states (DOS) profiles showing the evolution of electronic levels.

Figure 3.20 illustrates the structural, band structure, and DOS properties for $Zn_{31}O_{36}Ag_5$ and $Zn_{30}O_{36}Ag_6$. Both configurations preserve the WZ lattice, but local distortions due to Ag atoms are more pronounced in $Zn_{30}O_{36}Ag_6$, affecting the local symmetry. In both cases, the energy bands cross the Fermi level ($E - E_F = 0$ eV), indicating metallicr. The band gap is closing, especially in $Zn_{30}O_{36}Ag_6$, due to the higher doping level. The total DOS shows a high density near the Fermi level for both structures. In $Zn_{31}O_{36}Ag_5$, Ag contributes modestly, while in $Zn_{30}O_{36}Ag_6$ the Ag contribution near E_F is more significant. Zn and O continue to dominate the valence and conduction bands, but Ag doping increasingly fills the gap. These results indicate a clear trend: increasing Ag concentration leads to reduced band gap and enhanced

Figure 3.20: Electronic properties of SQS-generated ZnO:Ag with 5 and 6 Ag atoms

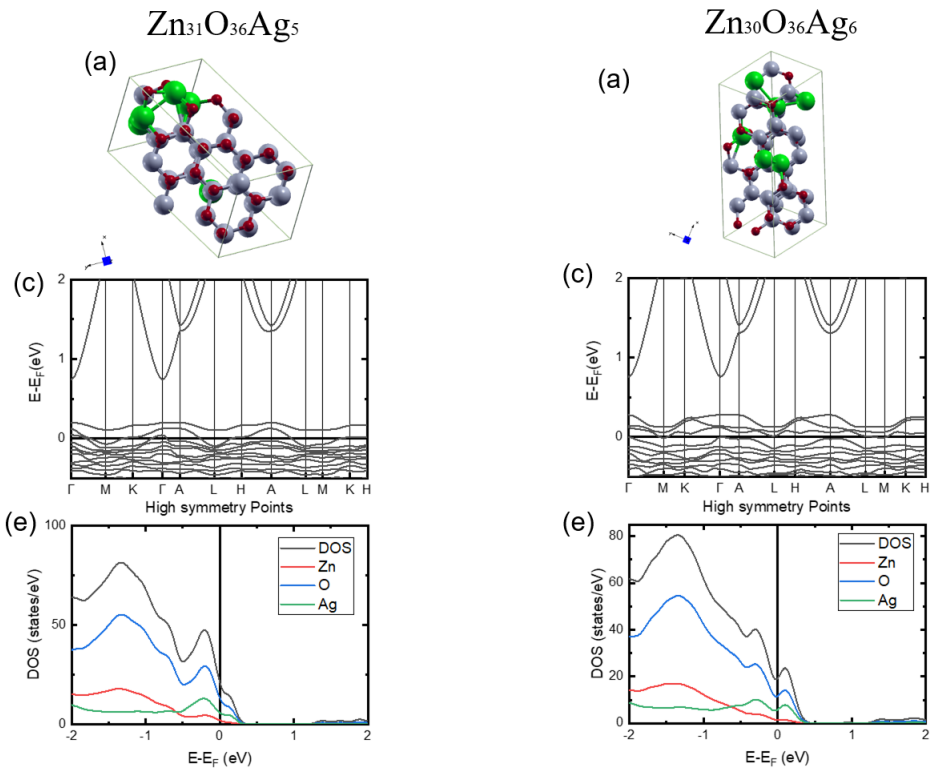

Source: Elaborated by the author (2025).
Note: (a)-(b) Visualizations of 72-atom ZnO:Ag supercells containing five and six Ag atoms, respectively, modeled using the SQS method. (c)-(d) Corresponding electronic band structures. (e)-(f) Density of states (DOS) profiles for each respective concentration.

electrical conductivity, with $Zn_{30}O_{36}Ag_6$ approaching metallic behavior due to the preference of Ag clustering forming metallic particles within the ZnO matrix.

As the Ag concentration increases, greater local distortion in the lattice is observed, especially in $Zn_{28}O_{36}Ag_8$, Fig. 3.21, which is expected with increased doping. The Fermi level (E_F) is located within partially occupied bands. There are signs of gap closing or nearly metallic behavior. This is even more evident: the bands cross the Fermi level, characterizing metallic behavior. It shows that the increase in Ag concentration completely eliminates the band gap. In both cases, there is a significant density of states at the Fermi level, indicating increasing conductivity. The dominant contribution comes from O and Zn, but Ag atoms also contribute around the Fermi level. $Zn_{28}O_{36}Ag_8$ exhibits a sharper DOS peak closer to and at E_F, characterizing a clearer transition to a metallic state than in $Zn_{29}O_{36}Ag_7$. Doping with 7 and 8 Ag atoms introduces increasing distortions in the lattice and strongly impacts the electronic properties. $Zn_{29}O_{36}Ag_7$ is in a transitional phase between a degenerate semiconductor and a metal. $Zn_{28}O_{36}Ag_8$ shows characteristics of a metallic conductor, with bands crossing E_F and a high density of states. This confirms that increasing Ag concentration in ZnO can induce a semiconductor-to-metal transition. Once more, we see that the structures generated by SQS favor the clustering of Ag atoms.

Figure 3.21: Electronic properties of SQS-generated ZnO:Ag with 7 and 8 Ag atoms

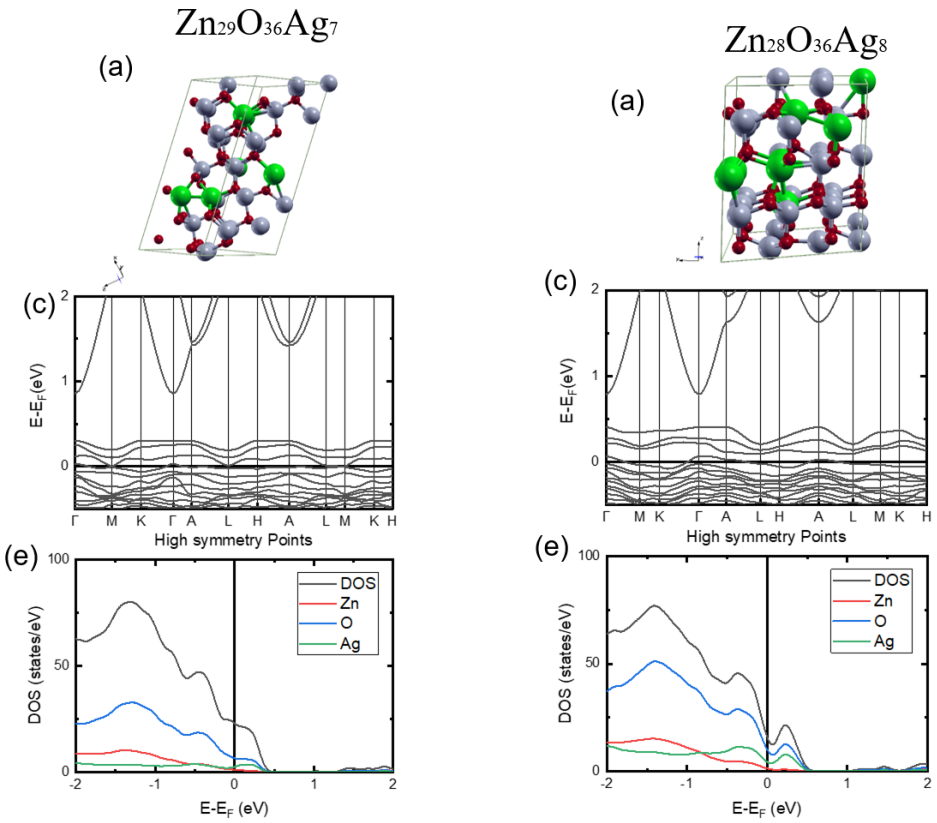

Source: Elaborated by the author (2025).
Note: (a)-(b) Visualizations of 72-atom ZnO:Ag supercells containing seven and eight Ag atoms, respectively, modeled using the SQS method. (c)-(d) Corresponding electronic band structures. (e)-(f) Density of states (DOS) profiles showing high-concentration effects on the band edges.

3.2.4 Comparing all Structural and Electronic Properties of ZnO doped with Ag

To better assess the differences and similarities of all generated structures, we will next discuss their structural and electronic properties. Figure 3.22 shows the variation of the lattice parameters a and c of the WZ ZnO structure as a function of Ag doping in a 72-atom supercell for all three methods described previously (SQS - diamond symbols, random arrangements - circles, and SQS-build - triangles). We observe that the lattice parameter a remains relatively stable for low doping concentrations (up to approximately 5.56%, or 4 Ag atoms) with slight variations among the different structural construction approaches, Fig. 3.22(b). However, starting from 6 Ag atoms (8.33%), a significant increase in the dispersion of the a values is observed, indicating that the substitution of Zn by Ag begins to significantly impact the crystal structure. Some configurations, especially the random ones, show lattice expansion, which can be attributed to the atomic size mismatch between Zn and Ag. For the c parameter, Fig. 3.22(b), a similar trend is found, with relative stability at low concentrations and greater variation as the doping level increases. The variation in c becomes particularly pronounced at concentrations

above 6 Ag atoms, with some structures showing an increase of more than 0.1 Å. This behavior may be related to anisotropic relaxation effects induced by the presence of Ag in the lattice.

Figure 3.22: Lattice constants a and c as a function of Ag concentration in ZnO.

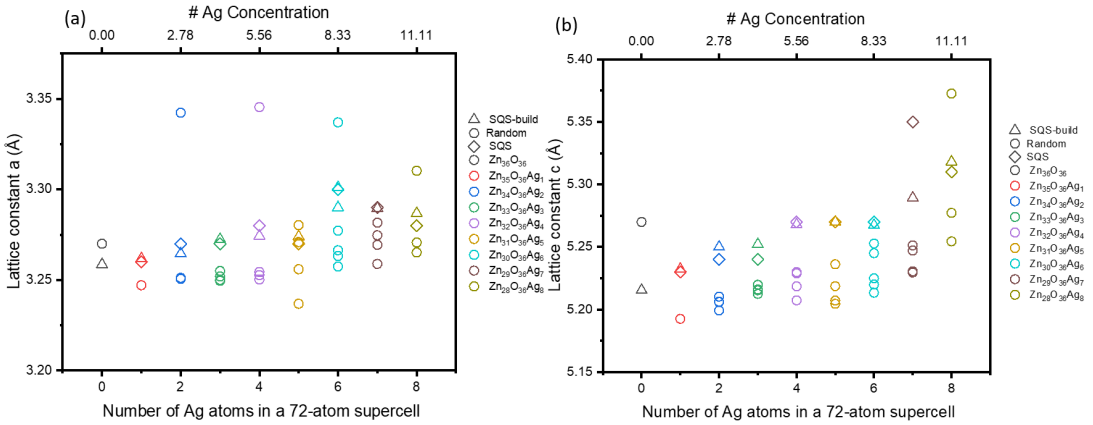

Source: Elaborated by the author (2025).
Note: Variation of lattice parameters (a) a and (b) c for different Ag concentrations in 72-atom supercells. The data compares random configurations, SQS, and SQS-build results. It is observed that the dispersion is significantly higher in random configurations compared to the optimized SQS models.

As expected, the incorporation of Ag atoms affects the lattice parameters of the ZnO WZ structure in a nonlinear manner due to clustering of Ag atoms observed in some structures. The substitution of Zn by Ag tends to expand the lattice, especially at higher concentrations, which is consistent with the larger atomic radius of Ag. Moreover, the comparison between different structural models highlights the importance of model selection in determining structural properties, with the SQS-based configurations exhibiting greater stability and less dispersion in lattice parameters.

Figure 3.23 presents the evolution of the Fermi level relative to the valence band maximum $(E_F - E_V)$ and the net charge associated with the Ag dopants as a function of their concentration in a 72-atom ZnO supercell. Various structural models are considered, including SQS-build, random, and SQS structures. We observe a clear trend in the position of E_F Figure 3.23 (a). For the undoped case ($Zn_{36}O_{36}$), E_F is located above VB, indicative of the intrinsic semiconductor behavior of pure ZnO. As Ag is introduced into the system, E_F progressively shifts downward, approaching or entering the valence band region. This shift becomes more pronounced with increasing Ag content, suggesting a p-type doping behavior due to Ag substituting for Zn, which introduces acceptor-like states in the band structure. Among the configurations, SQS-based models tend to exhibit more consistent behavior with smooth transitions in $E_F - E_V$, whereas random models show larger variability, indicating sensitivity to atomic arrangement.

Figure 3.23 (b) displays the net charge associated with the Ag atoms in each configuration. At low Ag concentrations (1–2 atoms), the net charge is approximately 1.0, suggesting that Ag behaves as a singly charged acceptor (Ag^+). As the concentration increases, the net charge

remains relatively constant in most models, especially in the SQS-based and random models, indicating the stability of Ag^+ incorporation in the ZnO matrix. However, certain configurations, particularly those constructed randomly, show deviations—likely due to local structural distortions or clustering effects that influence the electronic environment around Ag atoms.

Figure 3.23: Fermi level shift and net charge analysis of Ag-doped ZnO

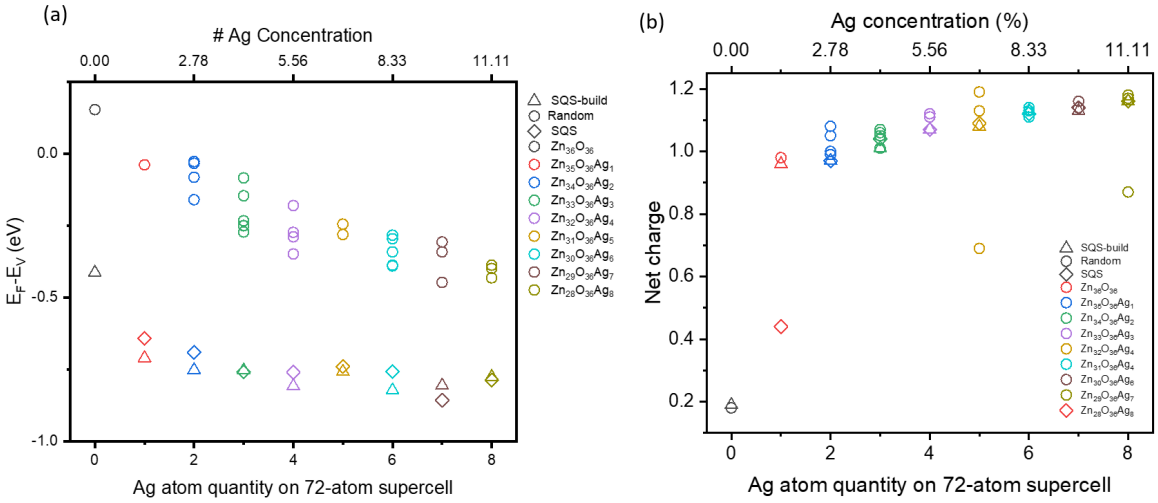

Source: Elaborated by the author (2025).
Note: (a) Fermi level position relative to the valence band maximum $(E_F - E_V)$ for different Ag concentrations, comparing SQS-build, random, and SQS models. (b) Net charge of Ag atoms as a function of the number of dopants in the supercell. These results indicate the electronic evolution of the system from a semiconductor to a degenerate p-type behavior.

We compare the changes in E_g as a function of Ag concentration in all 72-atom ZnO supercell in Figure 3.24. We observe the highest E_g values corresponds to the undoped case ($Zn_{36}O_{36}$), around 0.88 eV. As the number of Ag atoms increases, E_g systematically decreases, indicating a narrowing of the electronic gap due to the introduction of Ag-related impurity states. This trend is particularly steep at low doping levels (1–2 Ag atoms), where the gap drops significantly, demonstrating the strong influence of Ag even at dilute concentrations. At intermediate doping levels (3–6 Ag atoms), the E_g continues to decline, reflecting the impact of local atomic arrangements. At higher Ag concentrations (7–8 atoms), although the band gap values tend to approach a plateau around 0.3–0.4 eV for several configurations, certain atomic arrangements, especially those based on SQS, exhibit metallic behavior, with the band gap closing entirely. This suggests a saturation regime is reached for some structures, while others cross a threshold into full metallicity.

The observed variations among the SQS-build, random, and SQS structures indicate that atomic ordering and local environments play a significant role in modulating the electronic structure. In particular, SQS-build structures often retain slightly higher E_g values compared to the others, emphasizing the importance of atomic-scale structural control in tuning the electronic properties of doped ZnO systems.

Figure 3.24: Energy band gap (E_g) variation as a function of Ag concentration

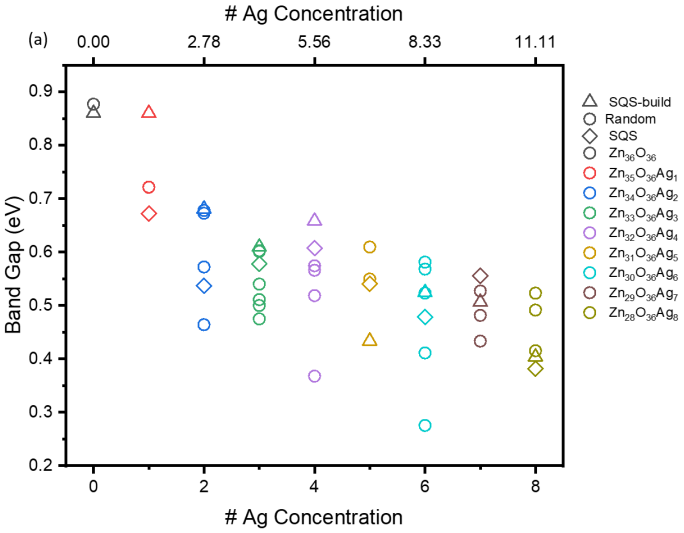

Source: Elaborated by the author (2025).
Note: Comparison of band gap values (E_g) for different Ag concentrations in 72-atom ZnO supercells. The data highlights the differences between configurations from SQS-build (triangles), random substitutions (circles), and the SQS algorithm (diamonds). A clear trend of gap narrowing (redshift) is expected as Ag content increases.

4 SUMMARY

In this dissertation, we utilized Density Functional Theory (DFT) calculations with Quantum ESPRESSO (QE) to comprehensively investigate the structural and electronic properties of pure and silver-doped zinc oxide (ZnO:Ag) in its wurtzite (WZ) phase, characterized by the space group $P6_3/m$. The analysis of pure ZnO established a baseline for its intrinsic properties, while the primary focus was on Ag-doped ZnO, employing three distinct methods to generate structures: random substitutions, Special Quasirandom Structures (SQS), and SQS-build. These methods were applied to 72 supercells to explore the effects of Ag doping across various concentrations, ranging from 0.93% to 11.11%. The study aimed to investigate when p-type semiconductor behavior is achieved, critical for applications in optoelectronics, photocatalysis, and transparent electronics. This chapter summarizes the key findings for pure and Ag-doped ZnO, emphasizing the impact of doping strategies on structural and electronic characteristics.

4.1 PURE ZnO

The investigation began with a four-atom unit cell of pure ZnO in the WZ configuration, optimizing lattice parameters and atomic positions. The optimized parameters ($a = 3.23$ Å, $c/a = 1.60$, Zn–O bond length = 1.97 Å) were compared with experimental values ($a = 3.25$ Å, $c/a = 1.60$, Zn–O = 1.97 Å) and previous theoretical studies [105, 109, 110]. Electronic structure calculations using PBE-GGA functionals were performed to confirm the direct band gap at the Γ point, which is expected to be around 0.71 eV, consistent with ZnO's intrinsic semiconductor behavior. The density of states (DOS) and partial density of states (PDOS) were analyzed, with the valence band expected to be dominated by O p-orbitals, while the conduction band by Zn s- and p-orbitals. Convergence tests were carried out to establish appropriate computational parameters, with a target wavefunction cutoff of 70 Ry, a charge density cutoff of 300 Ry, and a $6 \times 6 \times 3$ k-point grid to ensure accurate results.

To assess scalability, the system was expanded to 32, 72, and 108-atom supercells. Structural parameters remained consistent, with slight variations in lattice constants and a marginal band gap increase (up to 0.86 eV for 108 atoms). The DOS became denser in the valence band due to the increased number of atoms and electrons. Shifts in Fermi energy across supercells were observed, likely due to changes in DOS, edge effects, or insufficient k-point sampling, highlighting the need for careful parameter selection in larger systems. These results provided a robust reference for understanding the intrinsic properties of ZnO before adding dopants.

4.2 ZnO DOPES WITH AGAg

The primary focus of this work was on Ag-doped ZnO, where Zn^{2+} atoms were substituted with Ag^{1+} to induce p-type doping. The study analyzed 72-atom supercells with doping concentrations from 1.39% (1 Ag atom, $Zn_{35}O_{36}Ag$) to 11.11% (8 Ag atoms, $Zn_{28}O36Ag_8)and108 - atomsupercellswithlowerconcentrations(0.93\%for1Agatom, Zn_{53}O_{54}Ag_1$, and 1.85% for 2 Ag atoms, $Zn_{52}O_{54}Ag_2$). Three methods were employed to construct supercells: random doping, SQS, and SQS-build, with multiple configurations evaluated for each concentration to identify the most energetically favorable structure, determined by the lowest total energy.

4.2.1 Structural Properties

Structural analysis of the 72-atom supercell revealed that Ag doping induces lattice expansion, particularly at higher concentrations ($\geq 8.33\%$, or 6 Ag atoms), due to the larger atomic radius of Ag compared to Zn. As shown in Figure 3.22, the lattice parameter a remained relatively stable up to 5.56% doping (4 Ag atoms), with minor variations across configuration types. However, at higher concentrations, a significant increase in dispersion was observed, especially in random configurations, indicating structural sensitivity to Ag incorporation. The c parameter exhibited similar behavior, with pronounced variations above 6 Ag atoms, suggesting anisotropic relaxation effects. SQS and SQS-build configurations showed less dispersion and greater structural stability compared to random models, emphasizing the importance of controlled atomic arrangements (Figures 3.13 to 3.17, 3.18 to 3.21). For the 108-atom supercell, structural visualizations (Figure 3.12) indicated that the WZ structure was preserved with minimal local distortions at low doping levels (1–2 Ag atoms).

4.2.2 Electronic Properties and Charge Analysis

The electronic properties of ZnO:Ag were significantly altered by doping, with detailed band structure and DOS analyses performed for all three evaluated methods across various concentrations (Figures 3.4 to 3.11, 3.13 to 3.17, 3.18 to 3.21, 3.12). Key observations are summarized by method and doping concentration:

Random doping involved placing Ag atoms at Zn sites with energetic optimization, leading to significant variability in electronic properties (Figures 3.4 to 3.11, 3.12). At low doping levels (1–2 Ag atoms), $Zn_{35}O_{36}Ag_1$, $Zn_{34}O_{36}Ag_2$, $Zn_{53}O_{54}Ag$, $Zn_{52}O_{54}Ag_2$, the Fermi level was near the valence band maximum, indicating p-type doping with acceptor states. The band gap remained wide in $Zn_{53}O_{53}Ag_1$(108 atoms), but slightly reduced in $Zn_{34}O_{36}Ag_2$ (72 atoms),

with minimal Ag contributions to the DOS near the Fermi level. At intermediate levels (3–5 Ag atoms), $Zn_{33}O_{36}Ag_3$ to $Zn_{31}O_{36}Ag_5$, localized states and reduced band gaps indicated a transition to metallic behavior, with increasing Ag contributions near the Fermi level. At high doping levels (6–8 Ag atoms), $Zn_{30}O_{36}Ag_6$ to $Zn_{28}O_{36}Ag_8$ the band gap virtually disappeared in several configurations, with dense states crossing the Fermi level, indicating metallic behavior. The DOS showed significant Ag peaks near the Fermi level, dominating electronic states and enhancing conductivity.

The SQS-build method generated initially random structures, followed by geometric relaxation to achieve the lowest-energy configuration, prioritizing energetic stability over statistical randomness (Figures 3.13 to 3.17). For $Zn_{35}O_{36}Ag_1$ to $Zn_{33}O_{36}Ag_3$ (1–3 Ag atoms), the band gap gradually decreased, maintaining semiconductor characteristics with increasing Ag contributions near the Fermi level. For $Zn_{32}O_{36}Ag_4$ and $Zn_{31}O_{36}Ag_5$ (4–5 Ag atoms), the gap further narrowed, transitioning to metallic behavior. At $Zn_{30}O_{36}Ag_6$ to $Zn_{28}O_{36}Ag_8$ (6–8 Ag atoms), the gap was minimal or absent, with states crossing the Fermi level, confirming metallic behavior. The DOS showed progressively higher Ag peaks near the Fermi level, with $Zn_{28}O_{36}Ag_8$ exhibiting the most pronounced metallic characteristics. SQS-build configurations exhibited more consistent electronic properties compared to random doping, due to energetic optimization.

The SQS method optimized structures to replicate statistical correlations of a disordered lattice, maximizing similarity to ideal randomness without prioritizing total energy minimization (Figures 3.18 to 3.21). For $Zn_{35}O_{36}Ag_1$ and $Zn_{34}O_{36}Ag_2$ (1–2 Ag atoms), the band gap remained indicative of semiconductor behavior, with minimal structural distortions and small Ag contributions to the DOS. For $Zn_{33}O_{36}Ag_3$ and $Zn_{32}O_{36}Ag_4$ (3–4 Ag atoms), the gap narrowed, approaching metallic behavior. For $Zn_{31}O_{36}Ag_5$ and $Zn_{30}O_{36}Ag_6$(5–6 Ag atoms), the gap continued to close, with bands crossing the Fermi level in $Zn_{30}O_{36}Ag_6$, indicating metallic behavior. For $Zn_{29}O_{36}Ag_7$ and $Zn_{28}O_{36}Ag_8$(7–8 Ag atoms), the gap was completely eliminated, with high DOS at the Fermi level, confirming metallic behavior. SQS configurations provided a more uniform dopant distribution with preference for Ag clustering, resulting in smoother trends in electronic properties compared to random doping.

The net charge on Ag atoms in the 72-atom supercell remained approximately +1.0 across most concentrations, indicating stable Ag^{1+} incorporation as a singly charged acceptor (Figure 3.23). Deviations in random configurations at higher doping levels suggested local distortions or clustering effects. The band gap decreased systematically from 0.88 eV (undoped) to 0.3–0.4 eV at 11.11% doping (Figure 3.24), with the steepest reduction at low doping levels (1–2 Ag atoms). SQS-build structures retained slightly higher band gaps, indicating that structural ordering impacts gap modulation.

4.2.3 Comparison of Methods

The three methods utilized in this work exhibited distinct characteristics, random doping introduced significant variability due to uncontrolled Ag placement, leading to pronounced differences in band structure and DOS across configurations. It was effective for exploring a wide range of electronic behaviors but less reliable for consistent results, particularly at high doping levels where metallic behavior emerged unpredictably.

SQS-Build by prioritizing energetic stability, provided more consistent electronic properties, with smoother transitions from semiconductor to metallic behavior as Ag concentration increased. It was particularly effective for identifying energetically favorable configurations, though it may result in less uniform Ag distributions.

SQS, by mimicking statistical randomness, offered a realistic representation of disordered lattices, resulting in the most uniform dopant distributions and predictable electronic trends. It was ideal for studying the statistical effects of doping, but did not guarantee the lowest-energy structures.

In comparing our investigation of Ag-doped zinc oxide (ZnO:Ag) with previous studies, all of them affirm the induction of p-type conductivity, characterized by the Fermi level shifting toward or into the valence band [114]. However, they work attribute this behavior to the synergistic effects of zinc vacancies (V_{Zn}) in their $Zn_{34}O_{36}Ag_2$ (V^0_{Zn}) configuration (5.56% doping) [114], which enhances hole concentration and degeneracy, whereas our study relies exclusively on Ag substitution across a doping range of 0.93% to 11.11%. Their system is comparable to our intermediate doping levels, such as $Zn_{32}O_{36}Ag_4$ (5.56%), where both exhibit metallic characteristics. Notably, our work extends to higher concentrations ($\geq$8.33%), revealing a transition to metallic behavior not explored by them. The reference reports a slightly lower bandgap for undoped ZnO (0.73 eV) compared to our 0.81–0.86 eV, likely due to differences in supercell size or k-point sampling, though GGA's bandgap underestimation does not impact p-type identification. By employing larger supercells (72 and 108 atoms) and diverse doping methods (random, SQS, and SQS-build), our study elucidates a concentration-dependent electronic transition, complementing the defect-driven p-type degeneracy emphasized [114]. Our results obtained using Special Quasirandom Structures (SQS) are in good agreement with the findings reported by Francq et al. [115], where it was demonstrated that Ag atoms tend to cluster within the ZnO. The observed agglomeration of Ag in our simulations supports this behavior, particularly at higher doping concentrations. This clustering effect influences the local electronic structure and is consistent with the reduction of the band gap and the emergence of metallic characteristics in some configurations.

5 CONCLUSION

This study demonstrated the efficacy of DFT calculations with QE in characterizing the structural and electronic properties of pure and Ag-doped ZnO. Pure ZnO exhibited consistent structural and electronic properties across supercell sizes, serving as a reliable baseline. Ag doping, implemented via random, SQS-build, and SQS methods, successfully induced p-type conductivity, with significant lattice expansion and band gap narrowing that depended on doping concentration and method. At low doping levels (1–3 Ag atoms), ZnO:Ag retained semiconductor properties, suitable for optoelectronic applications. At intermediate levels (4–5 Ag atoms), a transition to metallic behavior was observed, while high doping (6–8 Ag atoms) led to metallic behavior, enhancing conductivity for applications like transparent electrodes. SQS and SQS-build methods provided more stable and predictable results compared to random doping, highlighting the importance of controlled dopant placement. The tunable band gap and p-type behavior of ZnO:Ag make it a promising candidate for advanced technological applications. Future research should explore co-doping strategies, defect interactions, alternative doping methods, and experimental validation to further optimize ZnO:Ag for practical use.

For future work, it is recommended to investigate the optical properties of Ag-doped ZnO to assess its potential for applications in optoelectronic devices, such as LEDs and photodetectors, by calculating absorption spectra, refractive indices, and photoluminescence characteristics using time-dependent DFT or many-body perturbation theory (e.g., GW+BSE). Additionally, employing hybrid functionals, such as HSE06, could address the underestimation of the band gap observed with PBE-GGA functionals, providing a more accurate description of the electronic structure and band gap values closer to experimental results (approximately 3.4 eV for pure ZnO). This combined approach would enhance the understanding of the material's optical response and electronic properties, enabling the design of tailored ZnO:Ag systems for advanced technological applications.

BIBLIOGRAPHY

1 ÖZGüR, *et al.* **A comprehensive review of ZnO materials and devices**. [S.l.: s.n.], 2005. v. 98.

2 JANOTTI, A.; WALLE, C. G. Van de. Fundamentals of zinc oxide as a semiconductor. **Rep Prog Phys**, v. 72, n. 126501, 2009.

3 WANG, Z. L. Zinc oxide nanostructures: growth, properties and applications. **J. Phys. Condens. Matter**, v. 16, p. R829–R858, 2004.

4 RASMIDI, R.; DUINONG, M.; CHEE, F. P. Radiation damage effects on zinc oxide (zno) based semiconductor devices–a review. **Radiation Physics and Chemistry**, v. 184, p. 109455, July 2021.

5 NANDI, S.; KUMAR, S.; MISRA, A. Zinc oxide heterostructures: advances in devices from self-powered photodetectors to self-charging supercapacitors. **Mater. Adv.**, v. 2, p. 6768–6799, 2021.

6 LITTON, C. W.; REYNOLDS, D. C.; COLLINS, T. C. **Zinc Oxide Materials for Electronic and Optoelectronic Device Applications**. [S.l.]: John Wiley & Sons, 2011.

7 THU, C. *et al.* Role of the metal-oxide work function on photocurrent generation in hybrid solar cells. **Sci. Rep.**, v. 8, p. 3559, 2018.

8 DEY, A. Semiconductor metal oxide gas sensors: A review. **Mater. Sci. Eng. B**, v. 229, p. 206–217, 2018.

9 KHAN, M. M.; ADIL, S. F.; AL-MAYOUF, A. Metal oxides as photocatalysts. **J. Saudi Chem. Soc.**, v. 19, p. 462–464, 2015.

10 FAN, J. *et al.* p-type zno materials: Theory, growth, properties, and devices. **Progress in Materials Science**, v. 58, p. 874–985, 2013.

11 DC. Recent advances in zno materials and devices. **Mater Sci Eng B**, v. 80, p. 383, 2001.

12 ANALYTICS, C. **Web of Science**. 2025. Accessed: 2025-01-14. Disponível em: <https://www.webofscience.com/wos/woscc/summary/58ecf35b-b734-42bb-b3a3-2c75ed143140-01438c9a94/relevance/1>.

13 JAGADISH, C.; PEARTON, S. J. (Ed.). **Zinc oxide bulk, thin films and nanostructures processing, properties and applications**. New York: Elsevier, 2006.

14 KLINGSHIRN, C. Zno: material, physics and applications. **ChemPhysChem**, v. 8, p. 782, 2007.

15 MORKOç, H.; ÖZGüR, **Zinc oxide: fundamentals, materials and device technology**. Berlin: Wiley-VCH, 2009.

16 PEARTON, S. J. *et al.* Recent progress in processing and properties of zno. **Prog Mater Sci**, v. 50, p. 293, 2005.

17 REYNOLDS, D. C.; LOOK, D. C.; JOGAI, B. Solid state communications. **Solid State Commun.**, v. 99, p. 873, 1996.

18 MACMANUS-DRISCOLL, J. L. Zno – nanostructures, defects, and devices. **Nome do Periódico**, Volume, p. Páginas, Ano.

19 MALAIKOZHUNDAN, B.; VINODHINI, J.; VIJAYAKUMAR, S. Zinc nanostructures: Toxicity, safety, and regulation in agroecosystems. In: **Zinc-Based Nanostructures for Environmental and Agricultural Applications**. [S.l.]: Elsevier, 2021. p. 457–470.

20 KREIDER, M. K. *et al.* Al–au thin films for thermally stable and highly sensitive plasmonic sensors. **J. Phys. Chem. C**, v. 126, p. 5628–5639, 2022.

21 GALSIN, J. S. **Solid State Physics**. City: Publisher, 2019.

22 CAROFIGLIO, M. *et al.* Doped zinc oxide nanoparticles: Synthesis, characterization and potential use in nanomedicine. **Applied Sciences**, v. 10, n. 15, p. 5194, 2020. Disponível em: <https://doi.org/10.3390/app10155194>.

23 HOSSEINI, S. *et al.* Effect of ag doping on structural, optical, and photocatalytic properties of zno nanoparticles. **Journal of Alloys and Compounds**, v. 640, p. 408–415, 2015. ISSN 0925-8388. Disponível em: <https://www.sciencedirect.com/science/article/pii/S092583881500849X>.

24 LI, Y.; ZHAO, X.; FAN, W. Structural, electronic, and optical properties of ag-doped zno nanowires: First principles study. **The Journal of Physical Chemistry C**, v. 115, n. 9, p. 3552–3557, 2011. Disponível em: <https://doi.org/10.1021/jp1098816>.

25 RÖSSLER, U. Energy bands of hexagonal ii-vi semiconductors. **Physical Review**, v. 184, p. 733–738, 1969.

26 MORKOç, H.; ÖZGüR Ümit. General properties of zno. In: ____. **Zinc Oxide: Fundamentals, Materials and Device Technology**. [S.l.]: Wiley-VCH, 2009. cap. 1, p. 1–76.

27 LANGER, D. W.; VESELY, C. J. Electronic core levels of zinc chalcogenides. **Physical Review B**, v. 2, p. 4885–4892, 1970.

28 POWELL, R. A.; SPICER, W. E.; MCMENAMIN, J. C. Photoemission studies of the electronic structure of zno. **Physical Review Letters**, v. 27, p. 97–100, 1971.

29 POWELL, R. A.; SPICER, W. E.; MCMENAMIN, J. C. Photoemission studies of the electronic structure of zno. **Physical Review B**, v. 6, p. 3056–3063, 1972.

30 LEY, L. *et al.* Photoemission study of the valence bands of si and ge. **Physical Review B**, v. 9, p. 600–621, 1974.

31 VESELY, C. J.; HENGEHOLD, R. L.; LANGER, D. W. Electronic structure of wurtzite-type semiconductors. **Physical Review B**, v. 5, p. 2296–2303, 1972.

32 BLOOM, S.; ORTENBURGER, I. Band structure of zno. **Physica Status Solidi (b)**, v. 58, p. 561–566, 1973.

33 CHELIKOWSKY, J. R. Electronic structure of wurtzite zns and zno. **Solid State Communications**, v. 22, p. 351–353, 1977.

34 IVANOV, I.; POLLMANN, J. Electronic structure of wurtzite-type semiconductors. **Physical Review B**, v. 24, p. 7275–7286, 1981.

35 LEE, D. H.; JOANNOPOULOS, J. D. Simple scheme for surface-band calculations. i. electronic structure of a slab and of a semi-infinite crystal. **Physical Review B**, v. 24, p. 6899–6907, 1981.

36 SCHRÖER, P.; KRÜGER, P.; POLLMANN, J. First-principles calculation of the electronic structure of the wurtzite semiconductors zno and zns. **Physical Review B**, v. 47, n. 12, p. 6971–6980, 1993.

37 MASSIDDA, S. *et al.* Polarization and dynamical charge of zno within different one-particle schemes. **Physical Review B**, v. 52, n. 24, p. R16977–R16980, 1995.

38 SCHRÖER, P.; KRÜGER, P.; POLLMANN, J. Ab initio calculations of the electronic structure of the wurtzite compounds cds and cdse. **Physical Review B**, v. 49, n. 24, p. 17092–17103, 1994.

39 VOGEL, D.; KRÜGER, P.; POLLMANN, J. Ab initio electronic-structure calculations for ii–vi semiconductors using self-interaction-corrected pseudopotentials. **Physical Review B**, v. 52, n. 20, p. R14316–R14319, 1995.

40 WU, Q. *et al.* First-principles calculations of the electronic structure and optical properties of yttrium-doped zno monolayer with vacancy. **Materials**, MDPI, v. 13, p. 724, 2020.

41 ENCYCLOPEDIA of Materials: Science and Technology. Second. [S.l.]: Elsevier, 2006. 1–9 p.

42 MANSY, S. *et al.* Computational and experimental study of wurtzite phase zno nanoparticles. **Materials Today Communications**, v. 35, p. 105688, 2023.

43 BASEDEN, K. A.; TYE, J. W. Introduction to density functional theory: Calculations by hand on the helium atom. **Journal of Chemical Education**, American Chemical Society, v. 91, n. 12, p. 2007–2222, 2014.

44 WU, Q. *et al.* First-principles calculations of the electronic structure and optical properties of yttrium-doped zno monolayer with vacancy. **Materials (Basel)**, v. 13, n. 3, p. 724, Feb 2020. Disponível em: <https://www.ncbi.nlm.nih.gov/pmc/articles/PMC7040613/>.

45 KITTEL, C. **Introdução à física do estado sólido**. 8. ed. [S.l.]: Editora LTC, 2006.

46 KOHN, W.; SHAM, L. J. Self-consistent equations including exchange and correlation effects. **Phys. Rev.**, v. 140, p. A1133, Nov 1965. Published 15 November 1965.

47 ALMEIDA, R. M. V. S. *et al.* Optoelectronic properties of zinc oxide: A first-principles investigation using the tran–blaha modified becke–johnson potential. **Journal Name**, Volume, January 2019.

48 SMITH, N. V. Photoelectron energy spectra and the band structure of the noble metals. **Physical Review B**, v. 3, p. 1862–1878, 1971.

49 FOX, M. **Optical Properties of Solids**. New York: Oxford University Press, 2001.

50 OKOYE, C. M. I. Theoretical study of the electronic structure, chemical bonding and optical properties of knbo3 in the paraelectric cubic phase. **Journal of Physics: Condensed Matter**, v. 15, p. 5945–5958, 2003.

51 BENASSI, A.; FERRETTI, A.; CAVAZZONI, C. **PWSCF's epsilon.x User's Manual**. [S.l.], 2003. Available online: <http://www.fisica.unimore.it>, <http://www.s3.infm.it>, <http://www.cineca.it>.

52 SCHMIDT-MENDE, L.; MACMANUS-DRISCOLL, J. L. Zno - nanostructures, defects, and devices. **Mater. Today**, v. 10, p. 40–48, 2007.

53 MCCLUSKEY, M. D.; JOKELA, S. J. Defects in zno. **J. Appl. Phys.**, v. 106, p. 071101, 2009.

54 WENCKSTERN, H. von *et al.* Anionic and cationic substitution in zno. **Physical Review B**, American Physical Society, Leipzig, Germany, v. 101, n. 1, p. 045211, 2020. Institut für Experimentelle Physik II, Universität Leipzig, Linnestr. 5, D-04103 Leipzig, Germany; I.Physikalisches Institut JLU-Giessen, Heinrich-Buff-Ring 16, D-35392 Gießen, Germany; Institut für Anorganische Chemie, Leibniz Universität Hannover, Callinstr. 9, 30167 Hannover, Germany; Institut für Physikalische Chemie, Technische Universität Braunschweig, Hans-Sommer-Str. 10, 38106 Braunschweig, Germany; Theoretische Chemie, Leibniz Universität Hannover, Callinstr. 3A, 30167 Hannover, Germany.

55 HUSSAIN, S.

Investigation of Structural and Optical Properties of Nanocrystalline ZnO — Linköping University, The Department of Physics, Chemistry and Biology, 2008.

56 KAXIRAS, E. **Atomic and Electronic Structure of Solids**. [S.l.]: Cambridge University Press, 2003.

57 GIUSTINO, F. **Materials Modelling using Density Functional Theory: Properties and Predictions**. 1st. ed. Oxford: Oxford University Press, 2014. 258 p.

58 BORLIDO, P. *et al.* Large-scale benchmark of exchange–correlation functionals for the determination of electronic band gaps of solids. **Journal of Chemical Theory and Computation**, v. 15, n. 9, p. 5069–5079, 2019. PMID: 31306006.

59 HOFMANN, P. **Solid State Physics: An Introduction**. [S.l.]: Wiley-VCH Berlin, 2015.

60 CASTRO, N. d. S. **Estudo teórico-experimental de nanoestruturas de ZnO dopado com íons Níquel(II) e Cromo(III)**. Tese (PhD Thesis) — Universidade Federal de Uberlândia, Uberlândia, Brazil, 2016.

61 WEHRSPOHN, R. B.; GEPPERT, T. Photonic crystals: Principles and applications. In: **Encyclopedia of Materials: Science and Technology**. Amsterdam: Elsevier, 2006.

62 DEY, A. Semiconductor metal oxide gas sensors: A review. **Materials Science Engineering B**, Elsevier, v. 229, p. 206–217, 2018.

63 GUO, Z. *et al.* Complete dielectric tensor and giant optical anisotropy in quasi-one-dimensional zrte5. **ACS Materials Letters**, American Chemical Society, v. 3, n. 5, p. 525–534, 2021. Disponível em: <https://pubs.acs.org/doi/10.1021/acsmaterialslett.1c00026>.

64 LIU, Y.; HOU, Q. The effect of ag doping and point defects on the electronic structure and photocatalytic properties of zno using first-principles. **Phys. Scr.**, v. 96, n. 5, p. 055808, 2021.

65 MOCKENHAUPT, B. *et al.* Phase evolution, speciation and solubility limit of aluminium doping in zinc oxide catalyst supports synthesized via co-precipitated hydrozincite precursors. **Journal of Materials Chemistry A**, Institute of Inorganic Chemistry, University of Duisburg-Essen, Universitätsstr. 7, 45141 Essen, Germany. E-mail: mbehrens@ac.uni-kiel.de, v. 11, n. 12, p. 5883–5897, 2023. Received 26th January 2023, Accepted 14th March 2023, First published on 14th March 2023.

66 CHAGAS, L. G. **Dopagem substitucional de perovskitas com metais de transição 3d: um estudo ab initio**. Dissertação (Master's thesis) — Universidade Federal de São Carlos, São Carlos, Brazil, 2022.

67 AUTHORS. Point defects in zno: an approach from first principles. **Sci. Technol. Adv. Mater.**, v. 12, p. 034302, 2011.

68 ATKINS, P.; FRIEDMAN, R. **Molecular Quantum Mechanics**. 6th. ed. [S.l.]: Oxford University Press, 2020. ISBN 978-0-19-880677-4.

69 MALIABE, D. G. **Structural and Electronic Properties of Zinc Oxide (ZnO) using Density Functional Theory with Hubbard Correction**. Dissertação (Master's Thesis) — Jimma University, College of Natural Science, Jimma, Ethiopia, Jan 2022.

70 PERDEW, J. P.; BURKE, K.; ERNZERHOF, M. Generalized gradient approximation made simple. **Physical Review Letters**, v. 77, p. 3865, 1996. Erratum: Phys. Rev. Lett. 78, 1396 (1997). Disponível em: <https://doi.org/10.1103/PhysRevLett.77.3865>.

71 VOSKO, S. H.; WILK, L.; NUSAIR, M. Accurate spin-dependent electron liquid correlation energies of local spin density calculations: a critical analysis. **Can. J. Phys.**, v. 58, p. 1200, 1980.

72 BASEDEN, K. A.; TYE, J. W. Introduction to density functional theory: Calculations by hand on the helium atom. **Journal of Chemical Education**, American Chemical Society, v. 93, n. 9, p. 1562–1566, 2016. Disponível em: <https://pubs.acs.org/doi/10.1021/acs.jchemed.6b00302>.

73 KOHN, W.; SHAM, L. J. Self-consistent equations including exchange and correlation effects. **Phys. Rev.**, American Physical Society, v. 140, p. A1133, November 1965. Disponível em: <https://doi.org/10.1103/PhysRev.140.A1133>.

74 GIANNOZZI, P. *et al.* Quantum espresso: a modular and open-source software project for quantum simulations of materials. **Journal of Physics: Condensed Matter**, IOP Publishing, v. 21, n. 39, p. 395502, 2009. [Submitted on 14 Jun 2009 (v1), last revised 26 Jul 2009 (this version, v2)].

75 MILITZER, B. Supercell design for first-principles simulations of solids and application to diamond, silica, and superionic water. **High Energy Density Physics**, v. 21, p. 8–15, 2016. ISSN 1574-1818. Disponível em: <https://www.sciencedirect.com/science/article/pii/S1574181816300659>.

76 EVARESTOV, R. A.; PISKUNOV, S.; ZHUKOVSKII, Y. F. Site symmetry approach in the supercell model of carbon-doped zno bulk. **Chemical Physics Letters**, v. 682, p. 91–95, 2017. ISSN 0009-2614. Disponível em: <https://www.sciencedirect.com/science/article/pii/S0009261417305523>.

77 BOUZIANI, I.; MOUSSA, K. Electronic- and optical-properties of zno nano-sheet doped and codoped with be and/or mg for ultraviolet opto-electronic technologies: density functional calculations. **Physica Scripta**, IOP Publishing, v. 95, n. 1, January 2020.

78 SCHMITZ, K. S. Supercell - an overview. In: **Physical Chemistry**. [S.l.]: Elsevier, 2018.

79 CHRONEOS, A. *et al.* Special quasirandom structures for binary/ternary group iv random alloys. **Chemical Physics Letters**, Department of Materials, Imperial College London, London SW7 2BP, UK; State Key Laboratory of Powder Metallurgy, Central South University, Changsha, Hunan 410083, China; PSE Division, KAUST, Thuwal 23955-6900, Saudi Arabia, v. 95, n. 11, p. 112101, 2009.

80 TASNáDI, F. *et al.* Special quasirandom structure method in application for advanced properties of alloys: A study on $ti_{0.5}al_{0.5}n$ and $tin/ti_{0.5}al_{0.5}n$ multilayer. **Computational Materials Science**, Elsevier, 2012. ADepartment of Physics, Chemistry and Biology (IFM), Linköping University, SE-581 83 Linköping, Sweden; bFunctional Materials, Materials Science and Engineering Department (MSE), Saarland University, P.O. Box 151150, 66041 Saarbrücken, Germany; cMaterials Modeling and Development Laboratory, NUST "MISIS", 119049 Moscow, Russia; dLACOMAS Laboratory, Tomsk State University, 634050 Tomsk, Russia. Disponível em: <https://www.elsevier.com/locate/commatsci>.

81 ZUNGER, A. *et al.* Special quasirandom structures. **Phys. Rev. Lett.**, American Physical Society, v. 65, p. 353, 1990.

82 LANDAU, D.; BINDER, K. **A Guide to Monte Carlo Simulations in Statistical Physics**. third. [S.l.]: Cambridge University Press, 2009.

83 CHEN, J.; XU, Z.; CHEN, Y. Introduction of density functional theory. In: **Electronic Structure and Surfaces of Sulfide Minerals**. [S.l.]: Elsevier, 2020.

84 HEITLER, W.; LONDON, F. Wechselwirkung neutraler atome und homöopolare bindung nach der quantenmechanik. **Zeitschrift für Physik**, v. 44, n. 6-7, p. 455–472, 1927.

85 HARTREE, D. R. The wave mechanics of an atom with a non-coulomb central field. part i. theory and methods. **Proceedings of the Cambridge Philosophical Society**, v. 24, n. 01, p. 89, 1928.

86 FOCK, V. Näherungsmethode zur lösung des quantenmechanischen mehrkörperproblems. **Zeitschrift für Physik**, v. 61, n. 1-2, p. 126–148, 1930.

87 SLATER, J. C. Note on hartree's method. **Physical Review**, v. 35, n. 2, p. 210–211, 1930.

88 SLATER, J. C. Atomic shielding constants. **Physical Review**, v. 36, n. 1, p. 57–64, 1930.

89 ROOTHAAN, C. C. J. New developments in molecular orbital theory. **Reviews of Modern Physics**, v. 23, n. 2, p. 69–89, 1951.

90 MOURIK, T. van; BüHL, M.; GAIGEOT, M. P. Density functional theory across chemistry, physics and biology. **Philosophical Transactions. Series A, Mathematical, Physical, and Engineering Sciences**, v. 372, n. 2011, p. 20120488, 2014.

91 SCHEIBER, B. A. **Wave Function**. 2024. Written and fact-checked by. Physics.

92 EISBERG, R.; RESNICK, R. **Física Quântica**. 2ª. ed. Rio de Janeiro: Editora Guanabara Koogan, 2002.

93 LEWARS, E. G. **Computational Chemistry: Introduction to the Theory and Applications of Molecular and Quantum Mechanics**. 2nd. ed. Dordrecht: Springer, 2011. ISBN 978-9048138614.

94 HEHRE, W. J. **A Guide to Molecular Mechanics and Quantum Chemical Calculations**. 18401 Von Karman Ave., Suite 370, Irvine, CA 92612: Wavefunction, Inc., 2003. Hardcover.

95 GRIFFITHS, D. J. **Introduction to Quantum Mechanics**. 3rd. ed. [S.l.]: Cambridge University Press, 2018. ISBN 978-1-107-00172-8.

96 CHATTARAJ, P. K.; CHAKRABORTY, D. (Ed.). **Electron Density: Concepts, Computation and DFT Applications**. [S.l.]: CRC Press, 2024. 608 p. ISBN 978-1-394-21764-9.

97 SZABO, A.; OSTLUND, N. S. **Electronic Structure: Basic Theory and Practical Methods**. [S.l.]: Cambridge University Press, 2004. ISBN 9780511805769.

98 BADER, R. F. W. **Atoms in Molecules**. New York: Oxford University Press, 1990.

99 SHUSTERMAN, G. P.; SHUSTERMAN, A. J. Teaching chemistry with electron density models. **Journal of Chemical Education**, v. 74, p. 771–776, 1997.

100 FORESMAN, J. B.; FRISCH, A. **Exploring Chemistry with Electronic Structure Methods**. Pittsburgh, PA: Gaussian, Inc., 1996. 302 p.

101 ROGERS, D. W. **Computational Chemistry Using the PC**. [S.l.]: VCH Publishers, 1990. ISBN 978-0-89573-735-1.

102 PATHAK, S. *et al.* Accurate hellmann–feynman forces from density functional calculations with augmented gaussian basis sets. **J. Chem. Phys.**, v. 158, p. 014104, 2023.

103 BASEDEN, K. A.; TYE, J. W. Introduction to density functional theory: Calculations by hand on the helium atom. **Department of Chemistry, Ball State University, Muncie, Indiana 47306, United States**, American Chemical Society and Division of Chemical Education, Inc., 2014.

104 CEPERLEY, D. M.; ALDER, B. J. Ground state of the electron gas by a stochastic method. **Physical Review Letters**, v. 45, p. 566–569, 1980. Cited on page 15.

105 MASOUMI, S.; NADIMI, E.; HOSSEIN-BABAEI, F. Electronic properties of ag-doped zno: Dft hybrid functional study. **Physical Chemistry Chemical Physics**, Royal Society of Chemistry, v. 20, p. 14688–14697, 2018.

106 DONG, C. *et al.* Electronic structure of nanostructured zno from x-ray absorption and emission spectroscopy and the local density approximation. **Physical Review B—Condensed Matter and Materials Physics**, APS, v. 70, n. 19, p. 195325, 2004.

107 HUANG, M. H. *et al.* Room-temperature ultraviolet nanowire nanolasers. **science**, American Association for the Advancement of Science, v. 292, n. 5523, p. 1897–1899, 2001.

108 SCHLüTER, M.; SHAM, L. Density-functional theory of the band gap. In: LöWDIN, P.-O. (Ed.). **Density Functional Theory of Many-Fermion Systems**. Academic Press, 1990, (Advances in Quantum Chemistry, v. 21). p. 97–112. Disponível em: <https://www.sciencedirect.com/science/article/pii/S0065327608605936>.

109 HARUN, K. *et al.* DFT + U calculations for electronic, structural, and optical properties of ZnO wurtzite structure: A review. **Results in Physics**, v. 16, p. 102829, 2020. ISSN 2211-3797. Disponível em: <https://www.sciencedirect.com/science/article/pii/S2211379719327287>.

110 OBA, F. *et al.* Native defects in oxide semiconductors: A density functional approach. **Journal of physics. Condensed matter : an Institute of Physics journal**, v. 22, p. 384211, 09 2010.

111 ALFAIFY, B. U. H. a S. Investigations of optoelectronic properties of novel zno monolayers: A first-principles study. **Journal of Computational Materials Science**, Elsevier, XX, n. X, p. 123–134, 2021.

112 MUNIR, T. *et al.* First principles study of structural and electronic properties of ti doped zno. **Journal Name**.

113 GOPIDI, H. R.; VASHISTA, L.; MALYI, O. I. Physics of band-filling correction in defect calculations of solid-state materials. **Journal Name**, XX, n. YY, p. ZZ–ZZ, 2024. Received 28th February 2024, Accepted 16th April 2024, First published on 4th June 2024. Disponível em: <mailto:oleksandrmalyi@gmail.com>.

114 ZHANG, H. *et al.* First-principles study on the influence of Cu/Ag/Au doping with different valence states and point defects on the p-type conductivity of ZnO. **physica status solidi (b)**, 2025. First published: 22 January 2025. Disponível em: <https://doi.org/10.1002/pssb.202400429>.

115 FRANCQ, R.; SNYDERS, R.; CORMIER, P.-A. Structural and morphological study of zno-ag thin films synthesized by reactive magnetron co-sputtering. **Vacuum**, v. 137, p. 1–7, 2017. ISSN 0042-207X. Disponível em: <https://www.sciencedirect.com/science/article/pii/S0042207X16302238>.